Engineering Coherent Control of Quantum Information in Spin Systems

by

Jonathan Stuart Hodges

Submitted to the Department of Nuclear Science and Engineering
in partial fulfillment of the requirements for the degree of

Doctor of Philosophy in Nuclear Science and Engineering

at the

MASSACHUSETTS INSTITUTE OF TECHNOLOGY
[September 2007]
August 2007

Author .....
Department of Nuclear Science and Engineering
August, 15 2007

Certified by .....
David G. Cory
Professor of Nuclear Science and Engineering
Thesis Supervisor

Read by .....
Sow-Hsin Chen
Professor of Nuclear Science and Engineering
Thesis Reader

Accepted by .....
Jeffery A. Coderre
Chairman, Department Committee on Graduate Students

Engineering Coherent Control of Quantum Information in Spin Systems

by

Jonathan Stuart Hodges

Submitted to the Department of Nuclear Science and Engineering
on August, 15 2007, in partial fulfillment of the
requirements for the degree of
Doctor of Philosophy in Nuclear Science and Engineering

Abstract

Quantum Information Processing (QIP) promises increased efficiency in computation. A key step in QIP is implementing quantum logic gates by engineering the dynamics of a quantum system. This thesis explores the requirements and methods of coherent control in the context of magnetic resonance for: (i) nuclear spins of small molecules in solution and (ii) nuclear and electron spins in single crystals.

The power of QIP is compromised in the presence of decoherence. One method of protecting information from collective decoherence is to limit the quantum states to those respecting the symmetry of the noise. These decoherence-free subspaces (DFS) encode one logical quantum bit (qubit) within multiple physical qubits. In many cases, such as nuclear magnetic resonance (NMR), the control Hamiltonians required for gate engineering leak the information outside the DFS, whereby protection is lost. It is shown how one can still perform universal logic among encoded qubits in the presence of leakage. These ideas are demonstrated on four carbon-13 spins of a small molecule in solution.

Liquid phase NMR has shortcomings for QIP, like the lack of strong measurement and low polarization. These two problems can be addressed by moving to solid-state spin systems and incorporating electron spins. If the hyperfine interaction has an anisotropic character, it is proven that the composite system of one electron and N nuclear spins (1e-Nn) is completely controllable by addressing only to the electron spin. This 'electron spin actuator' allows for faster gates between the nuclear spins than would be achievable in its absence. In addition, a scheme using logical qubit encodings is proposed for removing the added decoherence due to the electron spin. Lastly, this thesis exemplifies arbitrary gate engineering in a 1e-1n ensemble solid-sate spin system using a home-built ESR spectrometer designed specifically for engineering high-fidelity quantum control.

Thesis Supervisor: David G. Cory
Title: Professor of Nuclear Science and Engineering

Acknowledgments

In embarking on the journey of Ph.D. research, I knew that great challenges lie ahead, but I have always had the confidence that with enough hard work and time I would make it through. The following document represents a body of work into which went at least seven notebooks, countless cups of coffee, and too many long days and nights. However, in the beginning I did not realize how much the caring support of my colleagues, professors, family and friends would be such an influential factor in completing this work.

I would first like to acknowledge Professor David Cory, who has been a wise research supervisor and mentor over the past six years. He has taught me not only how to think intuitively about solving problems, but how to connect my work to the broader scientific community. It has been a pleasure to glean insight from David's wealth of knowledge in magnetic resonance and quantum information. His constant creativity in is a limitless source of inspiration.

I have had many fruitful collaborations and discussions of my work with some very bright minds at MIT. My logical qubit collaborator and office mate Paola Cappellaro has taught me how to mathematically formulate my often inarticulate ideas; she has become a great friend and colleague. Secondly, I would like to acknowledge my partner in ESR, Jamie Yang. He is a wizard in the laboratory and I have learned many valuable experimental skills working with him. I would also like to thank my friend and colleague from up north, Colm Ryan, for the many phone calls and discussions about NMR implementations of quantum information processing. I regret that the distance between Waterloo and MIT has kept us from working more closely together.

Professor Cory's research group is a unique and diverse collection of students, postdocs, and research scientists, who cycle through MIT in the usual academic fashion. However, the ethos of his group fosters collaboration and friendship both inside the lab and out. At the risk of making this acknowledgment into a role call, I would like to thank the following people: Nicolas Boulant, Joseph Emerson, Sekhar Ramanathan, Sid Sinha, Yaakov Weinstein, Joon Cho, Debra Chen, Daniel Greenbaum,

Anatoly Dementyev, Michael Henry, Grum Teklemarium, Ben Levi, Cecilia Lopez, Dimitri Pushin, Troy Borneman, Tim Havel, Sergio Valenzuela, Marco Pravia and all the others who I have neglected to list. I am especially grateful to Evan Fortunato, my mentor during my summer internship at MIT.

It feels like such a long time since I have run the gauntlet of qualifying exams and suffered through the first year of classes. During those times and after Whitney Raas was there for lending an ear whenever I need to share gripes about research or department politics. More importantly, our conversations were an excuse to grab another coffee.

Finally, I would like to thank my family for all their support throughout my education. Although it may be a mystery as to what I actually do, your continued questions and interest in my studies do not go unnoticed. Last, but certainly not least, this work would not have been possible without the loving support of my fiancee Gabrielle Alexis Cayton. She has reminded me that life is more than just work, grades, and publications; the sharing of her life with me has brought me much joy and fulfillment. Gabrielle, to you I dedicate this thesis.

Contents

List of Figures

List of Tables

Chapter 1

Introduction

The quantum nature of information processing can lead to computational speed-ups for certain types of algorithms, like factoring [132] and searching [53]. Truly quantum phenomena, like entanglement [40], have applications in creating provably secure communication channels [10] and can give measurement enhancements beyond the Heisenberg uncertainty limit [50]. These advantages are only possible through the coherent control of quantum dynamics while limiting the deleterious effects of decoherence. Nuclear magnetic resonance has served as a test-bed for the development of methods for coherent control and for the exploration of error correction and prevention schemes. This thesis will focus on the aspects of coherent control as it relates to quantum computation in such experimentally realizable systems.

The first part of this thesis (Chapters 2-4) develops methods for coherently controlling quantum information with the goal of implementing high-fidelity quantum gates. This includes improving the model of classical controls previously unaccounted for, as well as implementing new optimal control schemes from the literature. In the presence of decoherence, one method of extending coherence times is the use of quantum encodings. The resulting logical qubits, storing the informaiton over many physical qubits, present a unique challenge in coherent control, as the control Hamiltonians may not respect the structure of the encoding. Nonetheless, a scheme for controlling logical qubits is presented in Chapter 3 and is implemented in a liquid phase NMR testbed (Chapter 4) with natural decoherence.

The techniques developed in liquid phase NMR are then applied to systems that form interesting building blocks for future quantum devices. One example is nuclear and electron spin based qubits in the solid-state. In only a few isolated cases has complete coherent control been demonstrated, and in general, the issues of implementing control have not yet been articulated. In Chapter 5 of this thesis, we develop a method for controlling nuclear spins via the anisotropy of the hyperfine interaction (AHF). We show that such systems are universal and that nuclear-nuclear gates can be implemented in timescales faster than those afforded by solid-state NMR. We demonstrate such engineered quantum gates using the AHF and the methods in Chapter 2 in a test-bed solid-state system of one electron and one nuclear spin. The design of our pulsed ESR spectrometer used for this demonstration is the topic of Chapter 7.

An important consequence of moving to the electron-nuclear spin systems is that the electron spin T_1 relaxation couples via the HF interaction to the nuclear spins, reducing the nuclear spin coherence time. We can draw from the encodings and methods explored in the liquid state and use these to develop a quantum memory in the solid-state. The analysis of possible codes and the structure of electron T_1 induced decoherence in AHF systems is investigated in Chapter 6. Finally, Chapter 8 discusses the scalability of these solid-state systems including single spin projective measurements and concatenation of nuclear subsystems by coupling the electron spins.

Chapter 2

Engineering Quantum Control in Closed Systems

2.1 Background

The standard description of computing with quantum systems and simulating quantum dynamics on quantum systems can be broken down into in three main phases: state preparation, state evolution, and measurement. The state evolution is governed by the Schrödinger/Heisenberg differential equation of motion for a quantum mechanical state/operator. The solution to this differential equation is described by unitary evolution of the quantum state or operator. Thus quantum gates are unitary operators. The state preparation and measurement need not be unitary operations. Either can change the net purity of a quantum state or causing a 'wavefunction collapse'. While there are alternate models of quantum computation, such as measurement-based quantum computation [120], we are concerned with the standard model of generating arbitrary unitary operators enacting quantum gates.

Given the equation of motion for a quantum state, $\rho(t)$ and a set of controllable

$\mathscr{H}_C(t)$ and natural[1] ($\mathscr{H}_0$) Hamitonians for a closed quantum system:

$$\dot{\rho}(t) = -\frac{i}{\hbar}[\mathscr{H}_0 + \mathscr{H}_C(t), \rho(t)] \tag{2.1}$$

the evolution of the state can be found by direct integration. Provided the initial condition $\rho(0)$ is known, the final state is:

$$\rho(T) = U(0,T)\ \rho(0)\ U(0,T)^\dagger \tag{2.2}$$

The propagator, U is defined as:

$$U(0,T) = \mathcal{T} e^{-i\int_0^T \mathscr{H}_0 + \mathscr{H}_C(t)dt} \tag{2.3}$$

where $\mathcal{T}$ is the Dyson time-ordering operator specifying how the integral should take into account the non-commutivity of $\mathscr{H}$ at different times. Henceforth, $\hbar = 1$. In differential form, this reduces to

$$\dot{U}(t) = -i\big(\mathscr{H}_0 + \mathscr{H}_C(t)\big)\ U(t) \tag{2.4}$$

While the formal mathematics involved with the generation of unitary dynamics is beyond the scope of this thesis, the operator $U(t)$ is a dynamical group whose generator is the Hamiltonian [3]. If $\mathscr{H}_C(t)$ is given for all times $0 \leq t \leq T$ the dynamics can be integrated. However, we are interested in the inverse problem of finding some $\mathscr{H}_C(t)$ that generates a desired $U(t)$. The $\mathscr{H}_C(t)$ is not unique and may not exist for all T if $\|\mathscr{H}_C(t)\|$ is bounded.

2.2 Requirements for Control

Before diving into the various methods for generating quantum control, we first identify when it is even justified to expect some desired unitary operator given a natural Hamiltonian $\mathscr{H}_0$ and control Hamiltonian $\mathscr{H}_C$. From the theory of Lie alge-

[1]The static, time-independent Hamiltonian is also referred to as the system or drift Hamiltonian

bras/groups, we can expect $\mathscr{H}_0$ and $\mathscr{H}_C$ to be able to generate a full rank N×N unitary matrix representation of the elements in the Lie group $\mathsf{U}(N)$ if the Lie brackets (or equivalently commutators) of the generators span the group. This was shown in the context of quantum control by Rabitz [118] and others have shown numerical methods for assessing the completeness of control [127]. The question of complete controllability in classical linear dynamical systems has been treated in detail and much of the theory for classical control problems can be used in the quantum regime, most notably the satisfiability of control by graphical means [141, 4].

As an example of controllable and uncontrollable systems, take a simple two spin system[2]: $\mathscr{H}_0 = \frac{\omega_1}{2}\sigma_z^1 + \frac{\omega_2}{2}\sigma_z^2 + \frac{\pi J}{2}\sigma_z^1\sigma_z^2$. Suppose the control Hamiltonian is $\mathscr{H}_C = \sigma_x^1$. In order for the system to be completely controllable, we must be able to generate a complete set of orthogonal basis operators, represented as linear combinations of tensor products in the Pauli basis[3]. The first order commutator of $[\mathscr{H}_0, \mathscr{H}_C]$ generates the operator $O_1 = -i\frac{\omega_1}{2}\sigma_y^1 + \frac{\omega_2}{2}\sigma_z^2 - i\frac{\pi J}{2}\sigma_y^1\sigma_z^2$. By taking higher order commutators, we can generate further operators O_2, O_3, etc until the linear independence of the N^{th} operator from all the other operators O_{N-1} breaks down. In this simple case, we never generate an operator with a term σ_x^2 or σ_y^2, which are necessary to have 15 linearly independent operators. If we keep the same $\mathscr{H}_0$, but change $\mathscr{H}_C$ to $\mathscr{H}_C' = \sigma_x^1 + \sigma_x^2$, we can now generate the σ_x^2 terms necessary and make them linearly independent provided $\omega_1 \neq \omega_2$. In terms of a physical example the former case is like a liquid state NMR sample with spin 1 and spin 2 being different nuclear species (say ^{13}C and ^{1}H) while the latter case is a homonuclear spin system with a finite, large chemical shift difference.

One important distinction is the equivalence of $\mathsf{SU}(N) \times \mathsf{U}(1)$ and $\mathsf{U}(N)$ in the context of quantum mechanics [127]. These two groups differ only by a global phase, unobservable in quantum mechanics. The explicit presence of the identity element, $\mathbf{1}$ as a generator is a necessary condition for generating $\mathsf{U}(N)$. As the identity element

[2] σ_μ^j is the Pauli spin matrix for $\mu = \{x, y, z\}$. Here the product with the identity operator, $\mathbf{1} = \begin{bmatrix} 1 & 0 \\ 0 & 1 \end{bmatrix}$ on all other spins is implied for non-repeated indices.

[3] Here this is all the 16 possible tensor product combinations of σ_x,σ_y,σ_z, and $\mathbf{1}$ between spins 1 and 2.

corresponds to an energy shift in $\mathscr{H}_0$, it is not present in our model of the system. We thus only concern ourselves with the desired unitary matrix up to a global phase.

2.3 Methods

While the algebra generated by the natural and control Hamiltonians provides a mathematical set of conditions for universality, generating arbitrary unitary gates using this knowledge can be non-intuitive. Fortunately, quantum information science has provided various constructions of gates [36] that are universal: single-qubit rotations and any complete set of two-qubit couplings is sufficient to generate any unitary operator. For a magnetic resonance system, RF pulses applied on resonance with any spins' Larmor frequency act as single spin rotations. Periods of evolution under $\mathscr{H}_0$ will behave as a gate with many spin-spin couplings. Refocusing pulses can be applied to evolutions under $\mathscr{H}_0$ to reduce this evolution to two-qubit gates [67].

As an example, let us take the two spin system from above and construct a simple two-qubit gate: a controlled-not:

$$U_{cnot} = \begin{bmatrix} 1 & 0 & 0 & 0 \\ 0 & 1 & 0 & 0 \\ 0 & 0 & 0 & 1 \\ 0 & 0 & 1 & 0 \end{bmatrix} = E_-^1 \sigma_x^2 + E_+^1 \mathbf{1}^2 \tag{2.5}$$

$E_+ = |0\rangle\langle 0| = (\mathbf{1} + \sigma_z)/2$, $E_- = |1\rangle\langle 1| = (\mathbf{1} - \sigma_z)/2$. The projective operator form of the CNOT gate is then rearranged to look like a rotation having the form e^{iA} by applying a variety of identities. For clarity, we work out this simple case.

$$
\begin{aligned}
E_-^1\sigma_x^2 + E_+^1\mathbf{1}^2 &= E_-^1\sigma_x^2 + (\mathbf{1}^1 - E_-^1)\mathbf{1}^2 && (2.6)\\
&= E_-^1 e^{i\frac{\pi}{2}\mathbf{1}^2} e^{-i\frac{\pi}{2}\sigma_x^2} + (\mathbf{1}^1 - E_-^1)\mathbf{1}^2 && (2.7)\\
&= E_-^1 e^{i\frac{\pi}{2}\mathbf{1}^2} e^{-i\frac{\pi}{2}\sigma_x^2} + (\mathbf{1}^1 - E_-^1)\mathbf{1}^2 && (2.8)\\
&= \mathbf{1}^{12} + E_-^1(e^{i\frac{\pi}{2}(\mathbf{1}^2-\sigma_x^2)} - \mathbf{1}^2) && (2.9)\\
&= e^{i\frac{\pi}{2}E_-^1(\mathbf{1}^2-\sigma_x^2)} && (2.10)\\
&= e^{i\frac{\pi}{4}(\mathbf{1}^1-\sigma_z^1)(\mathbf{1}^2-\sigma_x^2)} && (2.11)\\
&= e^{i\frac{\pi}{4}\mathbf{1}^{12}} e^{-i\frac{\pi}{4}\sigma_z^1} e^{-i\frac{\pi}{4}\sigma_x^2} e^{-i\frac{\pi}{4}\sigma_z^1\sigma_x^2} && (2.12)
\end{aligned}
$$

Since global phases are not observed we can drop the first exponential. We further simplify this result by applying spin-selective rotations about x and y:

$$
\begin{aligned}
e^{-i\frac{\pi}{4}\sigma_z^1} e^{-i\frac{\pi}{4}\sigma_x^2} e^{-i\frac{\pi}{4}\sigma_z^1\sigma_x^2} &= && (2.13)\\
&= e^{-i\frac{\pi}{4}\sigma_z^1} e^{-i\frac{\pi}{4}\sigma_x^2} e^{i\frac{\pi}{4}\sigma_y^2} e^{-i\frac{\pi}{4}\sigma_z^1\sigma_z^2} e^{-i\frac{\pi}{4}\sigma_y^2} && (2.14)\\
&= e^{-i\frac{\pi}{4}\sigma_x^1} e^{-i\frac{\pi}{4}\sigma_y^1} e^{i\frac{\pi}{4}\sigma_x^1} e^{-i\frac{\pi}{4}\sigma_x^2} e^{i\frac{\pi}{4}\sigma_y^2} e^{-i\frac{\pi}{4}\sigma_z^1\sigma_z^2} e^{-i\frac{\pi}{4}\sigma_y^2} && (2.15)
\end{aligned}
$$

If the spins 1 & 2 are sufficiently well separated in frequency (i.e. they are different nuclear species), then one can independently address spin 1 and spin 2. Operators of the form $e^{-i\theta\sigma_{x,y}^j/2}$ can be implemented by applying a the control Hamiltonian for a short period of time (T) at the resonance frequency of the j^{th} spin such that $\theta\sigma_{x,y} = \mathscr{H}_C T$. This is commonly referred to as a *hard pulse.* The internal dynamics of the system can be neglected if $|\mathscr{H}_C| \gg |\mathscr{H}_0^R|$ for the rotating frame of the particular spin species. To implement a very good approximation of the $\sigma_z\sigma_z$ coupling, we allow the system to evolve under $\mathscr{H}_0$ for a time $1/2J$, applying a hard π pulse to both spins 1 and 2 at the end and half way through the evolution period [114]. This occurs because when the resonance frequencies of spins 1 & 2 are much greater than the scalar interaction strength, the operational form $\sigma^1 \cdot \sigma^2$ is reduced to only the secular part $\sigma_z^1\sigma_z^2$. The former is the strong coupling regime; the latter is the weak coupling

regime.

If the spins 1 & 2 are not sufficiently separated in frequency, then applying a hard pulse to spin 1 will have a non-trivial effect on spin 2. Spin selective rotations can be accomplished by applying collective pulse and allowing the chemical shift difference to differentiate between the two spins. By interspersing evolution under $\mathscr{H}_0$ with a series of pulses, arbitrary rotations of either spin is possible. Another possible approach is to apply a longer, weaker pulse on resonance with the spin under consideration. As the excitation bandwidth is inversely proportional to the total time of the pulse, a long enough pulse will have little effect on the other spin. During the pulse, the system continues to evolve under $\mathscr{H}_0$ however. This evolution must be tracked and unwanted evolution refocused by a set of π rotations at particular times. In addition, $\mathscr{H}_0$ will exhibit some degree of strong coupling, making the evolution of the spin system more complex.

For multiple spins of the same nuclear species, this tracking becomes increasing cumbersome. Several methods for tracking the net evolution of the spin systems,like Fourier synthesis of couplings [117] or numerical schemes [14], have been discussed, but approximate $\mathscr{H}_0$ as a diagonal Hamiltonian. The robustness of these gates can therefore be compromised by such strong coupling errors.

2.3.1 Strongly Modulating Pulses

Recall that in liquid phase NMR systems, the scalar coupling between two spins has an isotropic form $\sigma \cdot \sigma$, which the above methods approximate as $\sigma_z\sigma_z$ when the precession rates of the individual spins are well-separated [4]. A network of refocusing spin-selective π-pulses can remove the $\sigma_z\sigma_z$ component and can be phase shifted to remove other components of the strong coupling, however evolution of the system under strong coupling during a pulse can cause slight errors of the net unitary. While these can be reduced through further optimization of the delay times, another method is to constantly modulate the control fields to generate the desired unitary action.

[4]The Hamiltonian for liquid state NMR is $\mathscr{H}_0 = \sum_k \frac{1}{2}\omega_k\sigma_z^k + \frac{1}{2}\frac{\pi}{2}\sum_{k,l}\vec{\sigma^k}\cdot\vec{\sigma^l}$. See Chapter 4 for more details.

These will be referred to a strongly modulating pulses (SMP).

Instead of applying low-power, shaped pulses resonant with a particular spin precession rate, quick high-power pulses can be applied at a many arbitrary carrier frequencies. Since the pulses are high-power, each spin will nutate about the effective field of the applied RF and the off-resonant field including a Bloch-Siegert shift. If many of these quick pulses are applied at a variety of frequencies and phases, this averages out the couplings between the spins; the dynamics is then just single spin rotations given by the net action of the short pulses. For small systems this can be solved analytically, but tracking these individual trajectories is best done using numerical techniques.

First, a target unitary operation U_{target}, the natural Hamiltonian, $\mathscr{H}_0$ and the control Hamiltonians $\mathscr{H}_C$ are defined. The control Hamiltonian for this magnetic resonance system is:

$$\mathscr{H}_{C_p}(t) = A_p\Big(\cos(\Omega_p^{\mathrm{rf}}t + \phi_p)\sum_k \sigma_x^k + \sin(\Omega_p^{\mathrm{rf}}t + \phi_p)\sum_k \sigma_y^k\Big) \tag{2.16}$$

Physically, this represents an oscillatory magnetic field perturbation applied orthogonal to the quantization axis of the spins. Note that A_p is proportional to the Rabi frequency of the spins.

Next, an initial guess for the modulation parameters for the p^{th} period of strong irradiation, $\{\Omega_p^{\mathrm{rf}}, A_p, \phi_p, \tau_p\}$ are provided. Here Ω_p^{rf} defines the carrier frequency of the irradiation, A_p is the intensity of the magnetic field, ϕ_p the phase, and τ_p the duration for the particular period. The time-varying RF can be made time-independent by going to a rotating frame and transforming $\mathscr{H}_0$ to $\mathscr{H}_0^{R_p} = \mathscr{H}_0 - \frac{1}{2}\Omega_p^{\mathrm{rf}}\big(\sum_k \sigma_z^k\big)$. The net unitary operator for this p^{th} period,

$$U_p = e^{-i\tau_p(\mathscr{H}_0^{R_p} + A_p(\sum \sigma_x \cos\phi_p + \sum \sigma_y \sin\phi_p))} \tag{2.17}$$

and the net unitary of the P periods of irradiation is the product of the U_p

$$U_{net} = \prod_{p=1}^{P} U_{\rm fc} U_p \tag{2.18}$$

$U_{\rm fc}$ represents the overall frame change between the p^{th} and the $(p+1)^{th}$ periods and is just a collective σ_z rotation of an angle that is the difference of the two frames and times: $\Omega_{p+1}\tau_{p+1} - \Omega_p\tau_p$.

In order to compare the desired unitary with the calculated unitary, the gate fidelity measure [43] is used: $F(U_{net}, U_{target}) = \frac{|tr[U_{net}U_{target}^{\dagger}]|^2}{|tr[U_{net}U_{net}^{\dagger}]|^2}$. Since U_{net} is a function of $4P$ independent variables, F can be maximized by adjusting these $4P$ variables. One approach is to use the Nelder-Meade simplex [116] algorithm. We explicitly calculate U_{net} and evaluate F for values near an initial guess in parameter space, the simplex search finds a local minimum, hopefully resulting in $F = 1$. For a dispersion of parameters in either the control Hamiltonian ($\mathscr{H}_C^j$) (e.g. RF field inhomogeneity) or the system Hamiltonian ($\mathscr{H}_0^j$) (e.g. chemical shift uncertainty, coupling constant uncertainty, B_0 inhomogeneity, etc), the goodness measure can be weighted sum of F for each instance of the dispersion: $\bar{F} = \sum_j w_j F_j$, where w_j is the weighting factor and F_j is the fidelity for the j^{th} instance of the Hamiltonian.

In cases where the Larmor frequencies of the spins are well separated due to having distinct gyromagnetic ratios, multiple control Hamiltonians can be used. The full Hamiltonian can be broken up into subsystems: $\mathscr{H}_0 = \mathscr{H}_A + \mathscr{H}_B + \mathscr{H}_{AB}$. A rotating frame is also defined for each subsystem. If the desired unitary also conforms to the subsystem structure, as is the case for any single-spin rotations, it will have the form of $U_{target} = U_A \otimes U_B$. The SMP algorithm can then be broken up into finding U_A using the natural Hamiltonian $\mathscr{H}_A$ and controls $\mathscr{H}_{C_A}$. Next, the algorithm searches for U_B using $\mathscr{H}_B$ and $\mathscr{H}_{C_B}$ with the additional constraint that the total time of the SMP must be the one for implementing U_A. This subsystem approach reduces the simulation time since two separate smaller Hilbert spaces are easier to compute than one larger one. The strong, independent modulations of subsystems A and B are likely to average out the interaction of $\mathscr{H}_{AB}$. Simulations on the entire Hilbert space

of $\mathscr{H}_0$ for both control sequences show how well this averaging occurs. Should the convergence be inadequate, the controls for each subsystem can be used as an initial guess in searching over the entire Hilbert space. Coherent effects (e.g. Hartmann-Hahn matching) and relaxation (e.g. Overhauser effects) due to simultaneous pulsing should be considered. Lastly, in cases where the controls are available only over one subsystem, say $\mathscr{H}_{C_A}$, the other subsystem need not be treated quantum mechanically. The coupling effects due to $\mathscr{H}_{AB}$ can be divided into an "incoherent sum" of the $dim(\mathscr{H}_B)$ possible configurations of the spins in B, giving a set of Hamiltonians $\{\mathscr{H}_A\}$. This again reduces the size of the Hilbert space over which the algorithm must search [149]. For example, a seven spin-1/2 system, is represented as a 128×128 matrix, but a four spin-1/2 subsystem can be treated as 8 separate 16×16 matrices.

2.3.2 Gradient Ascent Pulse Engineering

The Gradient Ascent Pulse Engineering (GRAPE) algorithm [71] is a numerical method, like SMP, for finding control sequences for generating arbitrary unitary transformations. It differs in its searching of parameter space by taking the gradient of various goodness functions (i.e. gate fidelity) resulting in linear updates to the modulation sequence rather than using the simplex method.

While the SMP method defines periods of modulation with fixed duration, transmitter frequency, amplitude and phase, the GRAPE method varies the amplitude of two different orthogonal control parameters (like the in-phase and quadrature components of the RF field) for a fixed time step, Δt ,and a fixed number of points, N. At each point in time, t_j, the control Hamiltonian has K finite amplitudes, $a_j : \mathscr{H}_C = \sum_{k=1}^{K} a_{jk}\hat{C}_k$. Provided $|\mathscr{H}_T(t_j)|\Delta t \ll 1$, the net unitary propagator of the entire system is well approximated by the product of the j instantaneous unitaries:

$$U(T = N\Delta t) \approx \prod_j e^{-i\mathscr{H}_{T_j}\Delta t} \tag{2.19}$$

At this point, the same Nelder-Meade simplex algorithm for all $N \times K$ parameters can be used to optimize the fidelity function F. Alternatively, the GRAPE method

uses the product structure of U and the linearity of quantum theory to calculate the first derivative of F with respect to a_{jk} and updates the $N \times K$ parameters to move in the direction of steepest descend in parameter space. If the initial guess to the K independent controls are $\vec{a}_k^{(0)}$, then the next iteration of controls can be updated as:

$$\vec{a}_k^{(n+1)} = \vec{a}_k^{(n)} + \epsilon \, \vec{a}_k^{(n)} \cdot \nabla_k F \tag{2.20}$$

where ϵ is the step-size and $\nabla_k F|_j = \frac{\partial F}{\partial a_{jk}}$. The derivatives of F have a conveniently compact form, allowing for fast-computation and limiting the number of matrix exponentials to be computed.

$$\begin{aligned}
\frac{\partial F}{\partial a_{jk}} &= \frac{\partial}{\partial a_{jk}}\Big(\frac{|tr[U_{net}U_{target}^{\dagger}]|^2}{|tr[U_{net}U_{net}^{\dagger}]|^2}\Big) && (2.21)\\
&= \frac{1}{V}\frac{\partial}{\partial a_{jk}}\Big(tr[U_{net}U_{target}^{\dagger}]\, tr[U_{net}^{\dagger}U_{target}]\Big) && (2.22)\\
&= \frac{1}{V}\frac{\partial}{\partial a_{jk}}\Big(tr[U_N U_{N-1}\ldots U_j U_{j-1}\ldots U_1 U_{target}^{\dagger}] \times \\
&\quad tr[U_1^{\dagger}\ldots U_{j-1}^{\dagger}U_j^{\dagger}\ldots U_{N-1}^{\dagger}U_N^{\dagger}U_{target}]\Big) && (2.23)\\
&= \frac{1}{V}\Big(tr[\mathcal{U}_{j_+}(-i\hat{C}_k\Delta t)U_j\,\mathcal{U}_{j_-}]tr[U_{net}^{\dagger}U_{target}] + \\
&\quad tr[U_{net}U_{target}^{\dagger}]tr[\mathcal{U}_{j_-}^{\dagger}(i\hat{C}_k\Delta t)U_j^{\dagger}\mathcal{U}_{j_+}^{\dagger}U_{target}]\Big) && (2.24)
\end{aligned}$$

Here we have used the fact that $\partial U_j/\partial a_{jk} = (-i\hat{C}_k\Delta t)U_j$ and made the substitution $\mathcal{U}_{j_-} = U_{j-1}U_{j-2}\ldots U_1$ and $\mathcal{U}_{j_+} = U_N U_{N-1}\ldots U_{j+1}$. The derivative for each a_{jk} is thus related to the products of unitaries appropriately separated with the insertion of the control Hamiltonian for the j^{th} interval. In implementing this algorithm, we only need to calculate the matrix exponential for each time step once and store it in memory, taking successive products of matrices to arrive at the gradient. This greatly reduces the number of evaluations of F compared to that of the simplex algorithm. The algorithm terminates when F is within an acceptable threshold.

While both methods converge to find quantum gates numerically, there are key differences in the types of gates found using either method. The high-dimension parameter space over which we search has much structure and many local minima [83].

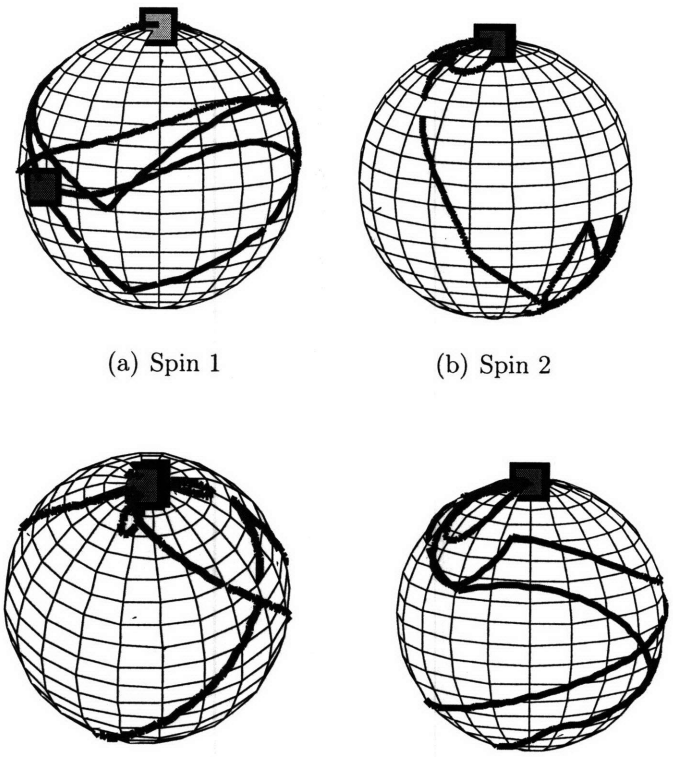

(a) Spin 1 (b) Spin 2

(c) Spin 3 (d) Spin 4

Figure 2-1: Bloch Sphere plots for an SMP. These four spheres represent the σ_x, σ_y, and σ_z components of each of the four carbon spins of crotonic acid. The green (light) box represents the initial state ($\rho_\Delta = \sum_k \sigma_z^k$) and the red (darker) box the final state ($-\sigma_y^1+\sigma_z^2+\sigma_z^3+\sigma_z^4$), the result of the rotation: $U_{C1\_90X} = e^{-i\pi\sigma_x^1/4}$. Note the discontinuities in the trajectory indicate switching from one period of RF to another period of RF. These transient effects are discussed below. The trajectories are nearly sections of a geodesic along the surface of the sphere; slight modulations in the line are due to small scalar couplings to other spins. The duration of this pulse is $557\mu s$.

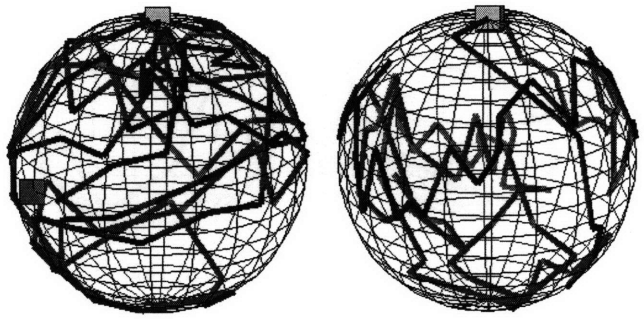

(a) Spin 1 (b) Spin 2

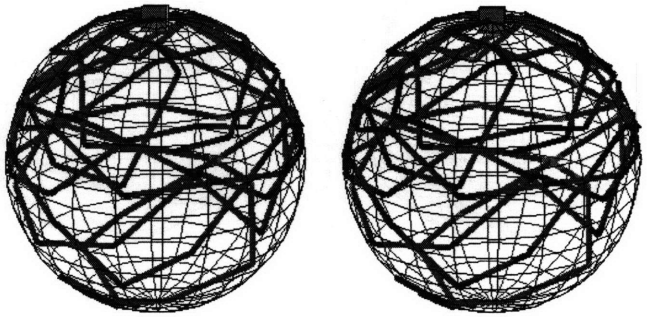

(c) Spin 3 (d) Spin 4

Figure 2-2: Bloch Sphere plots for GRAPE Pulse. The same conventions as Figure 2-1 are used here. The pulse consists of 100 points of RF, constant for $10\mu s$. The trajectory of the single spins is much more complicated than that of SMPs. This may lead to degradations in fidelity during implementation.

The initial guess of the algorithm confines the search to some local region in parameter space and the landscape of this region is modified by the weighting the goodness functions with penalties added for limiting the overall duration and maximum amplitude. Empirically[5], the SMP method finds single-spin rotations, $\mathsf{SU}(2) \otimes \cdots \otimes \mathsf{SU}(2)$ easily, but frequently fails to converge to for multiple-qubit gates ($\mathsf{SU}(4)$). This is not seen with the GRAPE algorithm, which finds multiple qubit gates provided the total time of the initial guess is sufficiently long. It remains an open question as to why we see this behavior. One possibility may be the complex penalty functions of the SMP method are tuned for single-spin rotations, while the GRAPE method does not impose added penalties beyond the fidelity. Another possiblity is that the number of independent control parameters for a GRAPE pulse (NK) are typically larger than those of an SMP ($NK \gg 4P$).

2.4 Imperfect Systems

Finding a set of classical control parameters using only the closed system quantum mechanical evolution gives a solution for generating some desired unitary transformation within a specified precision. Care must be taken to find implementable sets of control parameters, both in terms of the magnitude of the control and in the bandwidth of the specified control parameters. Furthermore, even within the limits of a classical control system, e.g. a magnetic resonance spectrometer, the specified control fields given to the controller may be distorted by the non-linear elements, like diodes and amplifiers, such that the fields present within the quantum system of interest differ from the desired fields.

To understand the effects of bandwidth, we must give an accurate model for the classical control system. In an NMR probe, one way of coupling magnetic fields to the sample of interest is the inductor of a tuned RLC circuit. As our model, we will chose the linear response to a driven, tuned and matched circuit but solve the unmatched circuit first as a simpler example. The response of a spin system driven with a tuned

[5]These results come from investigations on a four-qubit liquid-state NMR sample.

circuit has been treated in the context of multiple-pulse solid-state NMR [98], more generally using linear response theory [7], and even using finite pulse approximation [143]. We base our analysis on this work and then extend it to the control methods introduced in the previous section.

The parallel circuit in Figure 2-3 shows that in response to a time-dependent voltage $v_s(t)$ a current $i_L(t)$ will flow through the inductor L and consequently give rise to a magnetic field[6] $\vec{B}_1(t)$ The effects of the reactive elements can be described by a convolution kernel $K(t-t')$ whereby the current through the inductor is:

$$i_s(t) = \int_{-\infty}^{\infty} K(t')v_s(t-t')dt' \tag{2.25}$$

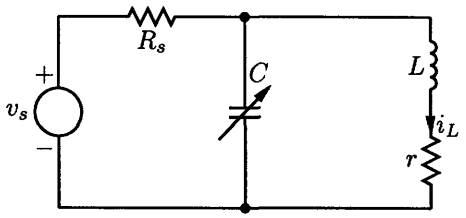

Figure 2-3: Parallel RLC Circuit model of NMR Probe.

Using the Laplace transform the integral equation is rewritten as a set of algebraic equations. A function of time, t can be expressed in terms of a complex variable s by the transform $f(s) \Leftrightarrow \int_0^{\infty} f(t)e^{-st}dt$. The net current $i_s(s)$ flowing across the voltage source is given by $v_s(s)/Z_{\text{total}}(s)$ where the total impedance of the circuit Z_{total} is,

$$Z_{\text{total}}(s) = \frac{sL + r + R_s LC(s^2 + \frac{r}{L}s + \omega_0^2)}{LC(s^2 + \frac{r}{L}s + \omega_0^2)}. \tag{2.26}$$

and $\omega_0^2 = 1/LC$. Using Kirchoff's laws, we solve for the current across the inductor

[6]In this simplification of the electromagnetic model, the current $i_L(t)$ is an approximation of the current density $\vec{J}(\vec{r},t)$ resulting in a field $(\vec{B}_1(t))$ inside the sample. In this model, we neglect the susceptibility of the sample and the geometric factors between current and field.

$i_L(s)$:

$$i_L(s) = \frac{i_s(s)}{LC(s^2 + \frac{r}{L}s + \omega_0^2)} \tag{2.27}$$

$$= \frac{v_s(s)}{R_s LC[s^2 + (\frac{r}{L} + \frac{1}{RC})s + \omega_0^2(1 + \frac{r}{R})]} \tag{2.28}$$

Defining the quality factors and shifted resonance as:

$$Q_{\|} = \omega_0 RC \tag{2.29}$$

$$Q_s = \frac{\omega_0 L}{r} \tag{2.30}$$

$$\frac{1}{Q_e} = \frac{1}{Q_{\|}} + \frac{1}{Q_s} \tag{2.31}$$

$$\Omega_0^2 = \omega_0^2(1 + \frac{r}{R}) \tag{2.32}$$

The complex transfer function, $\tilde{K}(s)$ is specified by the product of two poles by completing the square of the quadratic function of s in the denominator:

$$\tilde{K}(s) = \frac{\omega_0^2}{R(s + \alpha + i\omega_r)(s + \alpha - i\omega_r)} \tag{2.33}$$

where

$$\alpha = \frac{\omega_0}{2Q_e} \tag{2.34}$$

$$\omega_r^2 = \omega_0^2(1 + \frac{r}{R} - \frac{1}{4Q_e^2}) \tag{2.35}$$

Here Q_e is the effective quality factor of the tuned circuit, Ω_0 is the shifted resonance due to a damping factor, and ω_r is the addition shift due to resonance.

Following the standard impulse response theory [59], the impulse of a constant AC voltage with phase ϕ_0 and frequency ω turned on at some time $t = 0$ constitutes the following Laplace transform pair:

$$V(t) = V_0 e^{i\omega t + \phi_0}\theta(t) \Leftrightarrow V(s) = \frac{V_0 e^{i\phi_0}}{s - i\omega} \tag{2.36}$$

where $\theta(t)$ is the Heaviside function. The time varying current, $i_L(t)$, can be specified by the inverse Laplace transform, $\mathcal{L}^{-1}$ of the voltage and transfer function:

$$\begin{aligned} i_L(t) &= \mathcal{L}^{-1}\{V(s)K(s)\} && (2.37) \\ &= \frac{V_0 e^{i\phi_0}\omega_0^2}{R}\Big\{d_1 e^{i(\omega t+\phi_1)} + d_2 e^{-\alpha t}e^{i(\omega_r t+\phi_2)} - d_3 e^{-\alpha t}e^{-i(\omega_r t-\phi_3)}\Big\} && (2.38) \end{aligned}$$

The complex parameters d_j and ϕ_j are given by:

	1	2	3
d	$1/\sqrt{4\alpha^2\omega^2+(\alpha^2+\omega_r^2-\omega^2)^2}$	$1/(2\omega_r\sqrt{\alpha^2+(\omega-\omega_r)^2})$	$1/(2\omega_r\sqrt{\alpha^2+(\omega+\omega_r)^2})$
$\tan[\phi]$	$\frac{-2\alpha\omega}{\alpha^2+\omega_r^2-\omega^2}$	$\frac{\alpha}{\omega-\omega_r}$	$\frac{\alpha}{\omega+\omega_r}$

Table 2.1: Transient response parameters of tuned RLC circuit.

The terms with coefficients d_2 and d_3 give the transient response of the circuit to the sudden impulse, with a characteristic time of $\frac{1}{\alpha}$, oscillating at the loaded resonance frequency, ω_r. The steady current thus oscillates at the driven frequency, ω is out-of-phase with the driving voltage by ϕ_1. The in-phase and quadrature components of the current across the inductor can be separated from the complex response by taking the real and imaginary parts of the terms after factoring out the steady-state current.

$$i_L(t) = \frac{V_0 e^{i\phi_0}\omega_0^2}{R} d_1 e^{i(\omega t+\phi_1)}\Big\{1 + \frac{d_2}{d_1}e^{-\alpha t}e^{i((\omega_r-\omega)t+\phi_2-\phi_1)} - \frac{d_3}{d_1}e^{-\alpha t}e^{-i((\omega_r+\omega)t-\phi_3+\phi_1)}\Big\} \tag{2.39}$$

$$\begin{aligned} i_{L,0}(t) &= \frac{V_0 e^{i\phi_0}\omega_0^2}{R} d_1 e^{i(\omega t+\phi_1)} && (2.40) \\ i_{L,\parallel}(t) &= i_{L,0}\Big(1 + \frac{d_2}{d_1}e^{-\alpha t}\cos\big((\omega_r-\omega)t+\phi_2-\phi_1\big) \\ &\quad -\frac{d_3}{d_1}e^{-\alpha t}\cos\big((\omega_r+\omega)t-\phi_3+\phi_1\big)\Big) && (2.41) \\ i_{L,\perp}(t) &= i_{L,0}\Big(1 + \frac{d_2}{d_1}e^{-\alpha t}\sin\big((\omega_r-\omega)t+\phi_2-\phi_1\big) \\ &\quad +\frac{d_3}{d_1}e^{-\alpha t}\sin\big((\omega_r+\omega)t-\phi_3+\phi_1\big)\Big) && (2.42) \end{aligned}$$

Although described by a complicated set of equations, the transient response is simply understoood as an in-phase and quadrature current. The characteristic decay time of this current is proportional to $1/Q_e^2$, such that larger Q's will result in longer transients. With regard to applying a pulse of particular phase ϕ_0, the in-phase transient will cause a rotation of any single spin with increased amplitude for short times, while the quadrature transient with cause a rotation about an orthogonal axis $\phi_0 + \pi/2$. Thus the actual pulse rotates the spins about an axis offset from the intended axis of rotation [121, 98]

This simple RLC circuit has a single tunable element that can adjust the resonance frequency, but the impedance between the voltage source and the entire circuit will also change as the capacitance changes. By adding another capacitor, we have two independent elements to ensure the tuning of the circuit resonance to the Larmor frequency and matching the impedance of the circuit to the transmission line (50Ω).

Figure 2-4 shows a model tune-match circuit with independently tunable elements C_1 and C_2. We follow the same analysis as above, noting that the characteristic polynomial of the transfer function will increase by one power of s due to the addition of a reactive element. The total impedance of this circuit Z_{TM} is again used along with Kirchoff's laws to arrive at the transfer function, $\tilde{K}(s)$, relating the input voltage to the inductor current, $i_L(s) = v_s(s)\tilde{K}(s)$. $Z_{TM}(s)$ and $K(s)$ are:

$$\begin{aligned} Z_{\mathrm{TM}} &= \frac{1}{sC_2} + R_s + \frac{sL + r}{LC_1(s^2 + \frac{r}{L}s + \omega_0^2)} \\ &= \frac{R_s C_1 C_2 s^3 + L(C_1 + C_2)s^2 + r(C_1 + C_2)s + \omega_0^2}{sLC_1C_2(s^2 + \frac{r}{L}s + \omega_0^2)} \end{aligned} \tag{2.43}$$

$$\tilde{K}(s) = \frac{s/C_1R_s}{s^3 + \frac{L}{RC_s}s^2 + \frac{r}{R_sC_s}s + \frac{\omega_0^2}{R_sC_1C_2}} \tag{2.44}$$

where C_s is the effective series capacitance of C_1 and C_2.

Since the impulse voltage is a function of $1/s$ and $\tilde{K}(s)$ a cubic in s, the current response will be a quartic in s and can be solved exactly. The general form of the current $i_L(s)$ is $i_L(s) = \frac{\mathsf{R}(s)}{\mathsf{P}(s)}$, where R and P are polynomial functions of s and can be

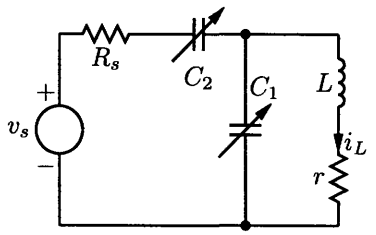

Figure 2-4: Tune-Match RLC^2 Circuit model of NMR Probe.

decomposed into partial fractions:

$$I(s) = \sum_j \frac{r_j}{s - p_j} \Leftrightarrow I(t) = \sum_j r_j e^{p_j t} \tag{2.45}$$

If we use thes initial impulse from Eq. (2.36), the current is:

$$i_L(t) = \frac{V_0 e^{i\phi_0}}{R_s C_1} \left\{ m_1 e^{i(\omega t + \varphi_1)} + \sum_{j=2} m_j e^{p_j t + i\varphi_j} \right\} \tag{2.46}$$

where p_j are the poles of the transfer function and $m_j e^{i\varphi_j}$ are the residues of those poles.

For the purpose of simulating the real field response $B_1(t)$ for a known control $v_s(t)$, it will suffice to compute a response for a given choice of circuit parameters $\{C_1, C_2, R_s, r, L\}$ valid for any piecewise constant $V(t)$, as the response will add linearly in time. We have computed the m_j, ϕ_j and p_j as a function of the circuit parameters using Mathematica and use the result in our numerical model below. We omit the solution here as it gives little insight to the problem.

As our model depends on the values of the circuit components, by completely specifying these values we can then apply our response model to the control fields for implementing a unitary operation. Not all the values of the circuit components can be easily measured, but can be inferred from other measurements. The impedance of the inductor within a Bruker proton/carbon/nitrogen inverse probe head is approximately $L = 80nH$. The resistance r can be inferred from the quality factor Q of the probe[7]

[7]We neglect Q loading due to the sample.

and the resonance frequency ω_0, measured using a network analyzer. A matched probe should have the real part of the impedance set to 50Ω and the imaginary part vanishing, yield the following set of equations:

$$C_1 = \frac{\omega R_s L \pm \sqrt{r^3 R_s - r^2 R_s^2 + r R_s \omega^2 L^2}}{\omega R_s (r^2 + \omega^2 L^2)} \tag{2.47}$$

$$C_2 = \frac{r}{\omega \sqrt{rR(r^2 - rR + \omega^2 L^2)}} \tag{2.48}$$

C_1 and C_2 can thus be inferred from L, r, R, ω_0.

2.4.1 Application to Strongly Modulating Pulses

For a strongly modulating pulse, the classical control parameters are described by a sum of N finite duration (τ) voltages with a particular amplitude (A), carrier frequency (ω) and phase(ϕ) $V_c(t) = \sum_{j=1}^{N} v_j(t)$ with

$$v_j(t) = A_j(t)\cos(\omega_j t + \phi_j)\Big(\theta(t - \tau_j - \sum_{k=1}^{j-1}\tau_k) - \theta(t - \sum_{k=1}^{j-1}\tau_k)\Big) \tag{2.49}$$

The control fields $B_j(t)$ can be derived for each of the v_j and added together with a time translation. The amplitude and phase difference between each of the periods give rise to an in-phase and quadrature transient. We simulate this transient by explicitly calculating the current response, $i'(t)$, in 10ns intervals for a strongly modulating pulse. As the measured response of the probe for a flat pulse shows transients on the order of 300ns (Figure 2-5) this provides enough points to see the affects of the transient. Figure 2-6 shows a seven period strongly modulating pulse with and without the simulation of transients. We note that for this particular pulse, the measured transient and the predicted transient have different shapes. It is not known whether this is an artifact of sampling at a different rate than the one at which the transient response was calculated.

The in-phase and quadrature transients behave like a net rotation of the in-phase

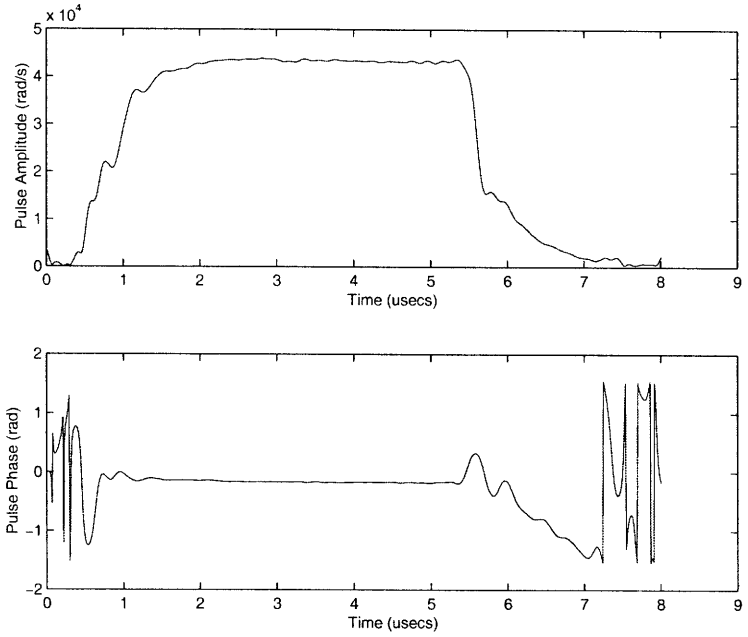

Figure 2-5: 5μs pulse digitized at 100MHz.

control Hamiltonian, $\mathscr{H}_{C-ip} = \sum_i \sigma_x^i$, and quadrature Hamiltonian $\mathscr{H}_{C-q} = \sum_i \sigma_y^i$. The transients can be modeled as small angle error unitaries in the vain of [143] and added to Eq. (2.18)

$$U_{net} = \prod_{k=1}^{N} U_{\epsilon(k)} U_k U_{\epsilon(k)}^{\dagger} = U_E \prod_{k=1}^{N} U_k \tag{2.50}$$

Although the $U_{\epsilon(k)}$ are separable and appear as single-spin rotations, the non-commutivity with the other U_k make them act non-trivially over the entire Hilbert space when taken over the entire modulation sequence. Thus, U_E need not appear as single-spin rotations. We should note that by the usual controllability criteria mentioned in the previous section, the presence of transients does **not** sacrifice the universality of system, but they do lead to an overall coherent error when implementing a gate.

We quantify this loss of fidelity by simulating the quantum dynamics for the current response $i'(t)$. For a characteristic set of pulses on crotonic acid (see Chapter 4) we calculate the loss of fidelity as a function of Q. The average loss of fidelity for this set is less than 0.05% for a modest Q ($Q_{measured}$=126), as seen in Figure 2-7.

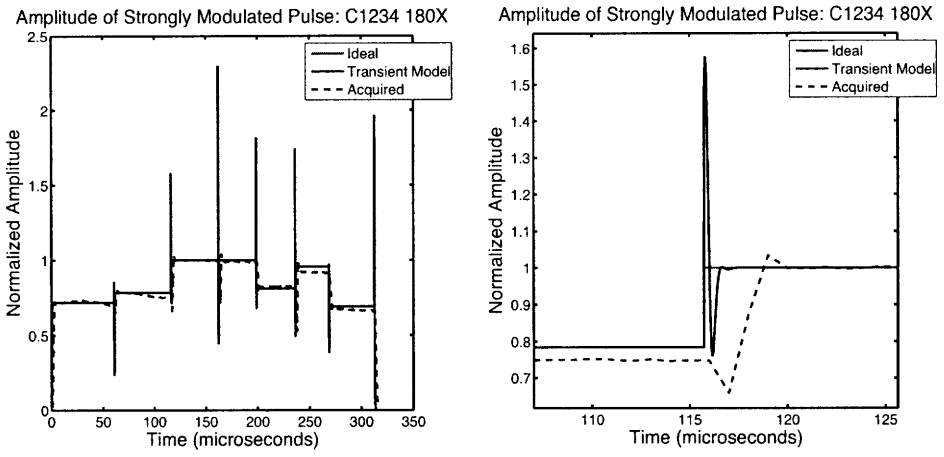

(a) (b)

Figure 2-6: Strongly Modulating Pulse with transients. This seven period pulse implements a collective $\frac{\pi}{2}$ rotation on all four spins of crotonic acid.

For Q's ranging from 50 to 500, we calculate the average loss of fidelity and worst case loss of fidelity over the set of 31 pulses. These results appear in Figure 2-8. In the limit of $Q \rightarrow 0$, the tuned circuit becomes broadband and the rapid changes of amplitude and phase do not affect the spin system.

2.5 Conclusions

The application of optimization and control theory to the problem of generating unitary evolution continues to improve the quality and permits us to increase the complexity of quantum gates. Furthermore, including bandwidth limitations in the system model will boost the fidelity of implemented pulses. The methods used for generating control, though having roots in liquid-state NMR, have been applied to many other systems including trapped ions, superconducting qubits, and solid-state nuclear and electron spin qubits. However, as the size of the Hilbert space grows exponentially with each additional qubit, using classical computing simulations to find ideal control parameters will not prove scalable or even feasible in the near future.

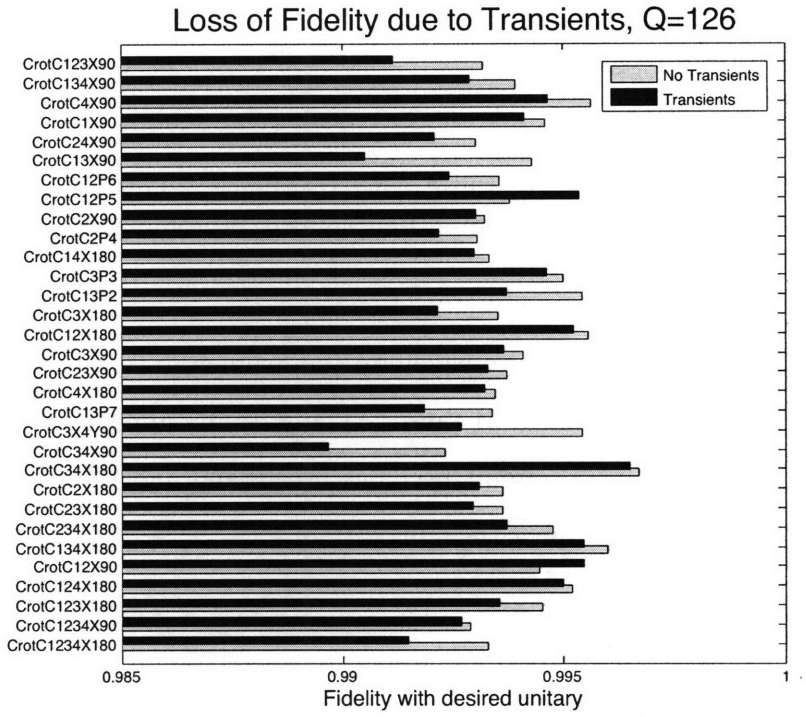

Figure 2-7: Fidelity loss with and without transients for Crotonic acid pulses. The addition of transients into the system model does not affect all pulses equally. This is due to the different number of periods of the pulses as well as the relative amplitude and phase switching between periods.

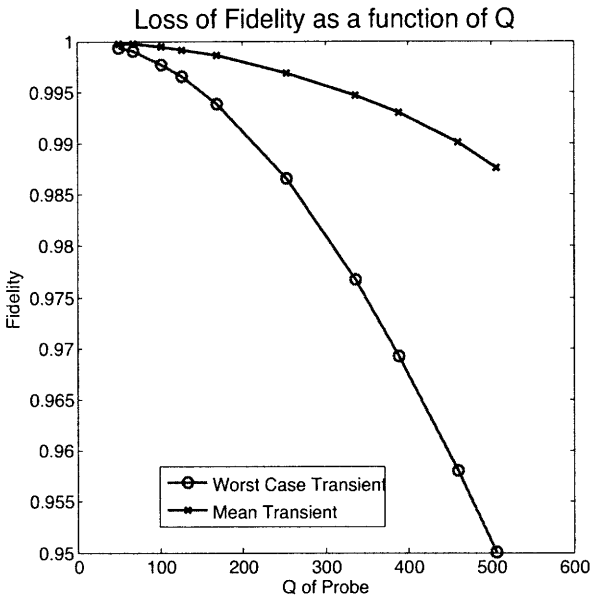

Figure 2-8: Loss of Fidelity versus Q. The worst case pulse and the average fidelity loss of a catalogue of 31 strongly modulating pulses. For moderate Q values (<150), the loss per pulse is less than 1%.

Lastly, the description here focused only on closed quantum systems, whereas the interaction of the controllable quantum system with an uncontrollable environment can lead to a loss of quantum coherence. Further improvements in the robustness of quantum gates can be made by taking into account the noise processes of the open quantum system. Indeed, the single-qubit rotation + ZZ-gate model presented above inherently refocuses slowly varying magnetic fields – usually responsible for T_2 proceses, but is not an optimal way of computing gates. Generating complex control sequences in the presence of a relaxation superoperator has been explored theoretically in the literature though an experimental demonstration of these open-system optimal control techniques has yet to be realized.

In summary, the present techniques for generating arbitrary control of quantum systems, while sufficient for today's experimental implementations, will need to mature greatly as they scale in size and as we account for decoherence.

Chapter 3

Engineering Quantum Control in Open Systems

When modeling a quantum system, one typically starts by describing the microscopic Hamiltonian of the system. Seldom are such microscopic systems well-isolated from the many other independent degrees of freedom of the surrounding microscopic systems and thus for a more complete description we include an interacting environment. We define the environment as all the other quantum systems or degrees of freedom which we do not have immediate control over. Our closed system, which had guaranteeing unitary dynamics, is now open to the influence of an environment; the dynamics will in general be non-unitary.

3.1 Encoding Quantum Information

Quantum mechanics describes the the microscopic evolution while statistical mechanics provides a macroscopic description of the system seen by averaging over the many degrees of freedom. As experimentalists we measure macroscopic quantities like voltage, charge, force, etc. that may seem very different than the quanta of angular momentum we model. The term decoherence [152, 51, 16] is used to describe the transition of the quantum mechanical nature of matter to the classical nature, as the quantum coherence or superposition of a state is lost. The finer points of decoherence

will not be discussed; it is a broad area of active research outside the scope of this thesis.

The problem of decoherence compromising quantum computations was identified early in the field of quantum information science. Quantum versions of error correcting codes (QECC) from classical communication theory [133, 20, 136] were employed to correct for particular error models and became unified under the stabilizer formalism [52]. The general scheme takes one qubit of quantum information and protects it from a finite number of errors by spreading the information among additional N ancilla qubits. If this encoding step occurs at time, $t = 0$, then at some later time t' (chosen for a particular error rate and the code depth) the information can be decoded from the N+1 qubits and the states of the N ancilla bits contain information about what sorts of errors occurred. Measurements of the ancilla bits do not destroy the original quantum state and can be used to rectify the original state. With N new ancilla bits the process can be repeated for the duration of the computation.

For noise models with particular symmetries, Zanardi [151] and Guo [38] found that particular subspaces of the Hilbert space between 1 qubit and N ancilla bits remain invariant under the action of the noise. These decoherence free subspaces are special cases of the more general noiseless subsystems. Such passive error avoidance encodings do not require the repeated measurement and refreshing QECC, making them infinite distance codes [75]. Experimental implementations of decoherence-free subspaces (DFS), noiseless subsystems (NS), and QECCs have proven their efficacy at correcting errors, though natural noise seldom coincides precisely with the chosen noise model.

3.2 Case Study: Correlated collective noise along quantization axis

3.2.1 System-Environment Model

We define a model Hamiltonian as a closed quantum system that can be broken into three different pieces:

$$\mathscr{H}_{S+E} = \mathscr{H}_S + \mathscr{H}_E + \mathscr{H}_S \otimes \mathscr{H}_E \tag{3.1}$$

where S describes the system and E the environment. If we move into an interaction frame of the system environment defined as $U_E(t) = e^{-i\mathscr{H}_E t}$, this renders the system environment Hamiltonian time dependent:

$$\tilde{\mathscr{H}}_{S+E} = U_E \mathscr{H}_{S+E} U_E^\dagger = \mathscr{H}_S + \mathscr{H}_S(t) \otimes \mathscr{H}_E(t) \tag{3.2}$$

If we reduce our observations to only those of the system Hilbert space ($\mathcal{H}_S$), the system Hamiltonian now has a time dependence due to the unknown environmental dynamics and the coupling term: $\mathscr{H}_S = \mathscr{H}_{det} + \mathscr{H}_{stoch}(t)$.

3.2.2 Stochastically fluctuating magnetic fields

In this section we use a simple, well-known DFS to motivate our discussion. The DFS encodes one logical qubit in two physical spin-$\frac{1}{2}$ particles and protects against collective dephasing caused by fully correlated uni-axial noise. In NMR, for example, fluctuations of the quantizing magnetic field B_z at a local molecule appear fully correlated, yet lead to dephasing when averaged over the spin ensemble [44].

These fluctuations are described by a Hamiltonian of the form $H_{stoch}(t) = \gamma B_z(t)\, Z$, where $Z = \frac{1}{2}\sum_i \sigma_z^i$ is the total angular momentum of the spins along the z-axis and γ is their gyromagnetic ratio. The DFS is based on the encoding $|0\rangle_L = |01\rangle$, $|1\rangle_L = |10\rangle$. A basis for the space of operators on the encoded qubit, in turn, is given by the

four logical Pauli operators:

$$\begin{aligned} \sigma_z^L &\Leftrightarrow \tfrac{1}{2}(\sigma_z^1 - \sigma_z^2) & \sigma_x^L &\Leftrightarrow \tfrac{1}{2}(\sigma_x^1\sigma_x^2 + \sigma_y^1\sigma_y^2) \\ \mathbf{1}^L &\Leftrightarrow \tfrac{1}{2}(\mathbf{1}^{1,2} - \sigma_z^1\sigma_z^2) & \sigma_y^L &\Leftrightarrow \tfrac{1}{2}(\sigma_x^1\sigma_y^2 - \sigma_y^1\sigma_x^2) \end{aligned} \tag{3.3}$$

This two spin-$\frac{1}{2}$ particle Hilbert space ($\mathbb{C}^4 = \mathbb{C}^2 \otimes \mathbb{C}^2$) can be described as a direct-sum of the total angular momentum subspaces, $Z_0 \oplus Z_{+1} \oplus Z_{-1}$, where l is the total angular momentum projected along the quantization axis. The logical basis states $|0\rangle_L$ and $|1\rangle_L$ reside exclusively in Z_0, where $Z_0 \equiv \mathbb{C}^2$. When we discuss leakage, we imply that information stored in Z_0 is lost to parts of Hilbert space outside of Z_0 through unitary dynamics. In this case, the information within the state of the system cannot be described completely by the four operators above (Eq. (3.3)). Since the total angular momentum with $l = 0$ is a constant of the motion under the system-enviroment Hamiltonian, a state not completely represented by a linear combinations of (Eq. (3.3)) is thus affected by decoherence. We will expore this DFS as implemented in liquid state NMR for both one and two logical qubits.

The internal Hamiltonian (in the rotating frame) for two spins in liquid-state NMR already is exclusively in Z_0 and thus can be expressed by the operators in Eq. (3.3); it does not cause mixing of the subspaces Z_l,

$$\mathscr{H}_{int} = \tfrac{\Delta\omega_{12}}{2}(\sigma_z^1 - \sigma_z^2) + \tfrac{\pi}{2} J_{12}\, \vec{\sigma}^1 \cdot \vec{\sigma}^2 \tag{3.4}$$

$$\cong \Delta\omega_{12}\sigma_z^L + \pi J_{12}(\mathbf{1}_L + \sigma_x^L) \tag{3.5}$$

where $\Delta\omega_{12}$ is the difference in chemical shift of the two spins and J_{12} the scalar coupling constant. The addition of $\mathbf{1}$ to $\mathscr{H}_{int}$ only adds an global shift in energy. Thus evolution under the internal Hamiltonian alone generates a continuous rotation about an axis in the logical xz-plane making an angle of $\arctan(\pi J_{12}/\Delta\omega_{12})$ with the logical z-axis.

If we want to add an additional encoded qubit to the system, we add two additional physical qubits and take the tensor product combinations of the states $|0_L\rangle$ and $|1_L\rangle$

to generate the basis vectors of two logical qubits stored within four physical qubits:

$$\begin{aligned} |00\rangle_L &\Leftrightarrow |0101\rangle, \qquad & |10\rangle_L &\Leftrightarrow |1001\rangle, \\ |01\rangle_L &\Leftrightarrow |0110\rangle, \qquad & |11\rangle_L &\Leftrightarrow |1010\rangle \end{aligned} \tag{3.6}$$

The liquid state NMR Hamiltonian for four scalar coupled spins, unlike the two spin case, cannot be written using solely the logical operators:

$$\mathscr{H}_{int-4} = \mathscr{H}_{1L} + \mathscr{H}_{2L} + \frac{\pi}{2}\left(J_{13}\,\vec{\sigma}^1 \cdot \vec{\sigma}^3 + J_{14}\,\vec{\sigma}^1 \cdot \vec{\sigma}^4 + J_{23}\,\vec{\sigma}^2 \cdot \vec{\sigma}^3 + J_{24}\,\vec{\sigma}^2 \cdot \vec{\sigma}^4\right) \tag{3.7}$$

Assuming the J_{jk} are unique, this Hamiltonian will drive certain basis states outside the DFS (e.g. $\vec{\sigma}^2 \cdot \vec{\sigma}^3|0101\rangle = 2|0011\rangle - |0101\rangle$). If the noise is collective only over each pair of spins that encodes a logical qubit [144], the states $|0011\rangle$ and $|1100\rangle$ are not protected against the noise and they will decohere. Therefore, the internal Hamiltonian will be responsible for leakage and the ultimate decay of the system.

Notice that we would in general expect the noise to be collective over all the physical qubits, and not pairwise collective. In the case of NMR, this corresponds to a fluctuating external magnetic field, which is fully correlated. However, the differences in energies between qubits could be strong enough to effectively add a non-collective component to the noise. In particular, we can consider in NMR the case in which each pair is formed by spins of a different chemical species. In this case, the difference in gyromagnetic ratio makes the strength of the noise acting on each pair unequal, so that the noise is no longer collective. On the other hand, when the Zeeman energy separation is considerable, the coupling between spins can be very well approximated by the diagonal part of $\vec{\sigma}^j \cdot \vec{\sigma}^k$, i.e. $\sigma_z^j \sigma_z^k$, which does not cause leakage.

When the noise generator is fully collective (as for homonuclear systems in NMR), the internal Hamiltonian still causes leakage, via the coupling to the states $|0011\rangle$ and $|1100\rangle$. Since these states belong to the zero eigenvalue subspace of the noise generator, they do not decohere. Information could still be lost at the measurement stage, since these states are not faithfully decoded to physical states. A unitary operation is enough to correct for this type of leakage [79], and since decoherence

is not an issue here, there are no concerns regarding the time scale over which the correction should be applied; however, amending for this unwanted evolution would in general mean the introduction of an external control. This can be a source of leakage leading to decoherence.

For logical encodings other than the DFS considered, the natural Hamiltonian may drive the state out of the protected subspace even for single logical qubits; for example, the NS considered in [45] will evolve out of the protected subspace whenever the chemical shifts or scalar couplings among its three constituent spins are not all equal. This will be discussed further in the context of electron-nuclear systems in Chapter 7.

3.2.3 Generating Control

If we assume that leakage from the natural Hamiltonian can be suppressed, then information within encoded qubits will be protected from decoherence, but may experience unitary evolution within the subspace due to a drift Hamiltonian. While this scheme provides an excellent quantum memory, it does not provide universal control of a logical qubit within the subspace. Nonetheless, universal computation within these DFSes has been shown to be possible from a theoretical point of view [81, 6, 86, 87] and in specific experimental conditions [44, 9, 106, 102]. In particular, universal fault-tolerant computation within a DFS is possible if the exchange interaction between qubits can be switched off and on at will [70, 37, 89]. Our interest is assessing the fidelity of control for a finite decoherence, for a finite bandwidth of our control parameters, and for Hamiltonians not respecting the symmetry of the logical subspace, in particular the ones available in NMR ($\mathscr{H}_{int}$ and $\mathscr{H}_C$).

We know that the control Hamiltonian for magnetic resonance (Eq. 3.8) and the natural Hamiltonian provide universal control over a Hilbert space $\mathcal{H} \in \mathbb{C}^4$ and thus can also provide universal control within a subspace $\mathcal{H}_s \subset \mathcal{H}$. However, unless both the natural and control Hamiltonians can be expressed *solely* as logical operators of the encoding, the control Hamiltonian will cause leakage outside of the subspace.

As an example, we take the collective DFS over two spins from above. The control

Hamiltonian can be parameterized as:

$$\mathscr{H}_C(t) \;=\; \omega_{\mathsf{rf}}(t)\, e^{-i(I_z^1+I_z^2)\phi(t)}\big(I_x^1+I_x^2\big)e^{i(I_z^1+I_z^2)\phi(t)} \tag{3.8}$$

This control Hamiltonian is physically the same as Eq. (2.16), but given in a rotating frame. $\omega_{\mathsf{rf}}(t)$ is a continuous function of the magnetic field amplitude, whereas A_p was a discrete time representation of the same amplitude. Note that this Hamiltonian is not expressible in terms of the logical operators given in (3.3). In the case of ideal control fields, an instantaneous π-pulse ($t_p \rightarrow 0$) corresponds to a logical operation [44], since $P_x(\pi) = e^{-i\pi/2(\sigma_x^1+\sigma_x^2)} = -e^{-i\pi/2(\sigma_x^1\sigma_x^2)}$, which is equivalent to a π pulse around σ_x^L. Figure 3-1 motivates the extent to which complete control over the logical subsystem can be obtained in the finite t_p regime. In this figure, we plot the purity of the projection of $\rho(t) = e^{-i\omega_{\mathsf{rf}}t(\sigma_x^1+\sigma_x^2)}\sigma_z^L e^{i\omega_{\mathsf{rf}}t(\sigma_x^1+\sigma_x^2)}$ on the logical subspace (notice that here and in the following we are only interested in the traceless part of the density matrix, since it is the only part that gives rise to the NMR signal). In the limit of very high RF power ($\frac{\Delta\omega}{\omega_{\mathsf{rf}}} \rightarrow 0$), the system undergoes a π-pulse in a time $t_p = \frac{\pi}{\omega_{\mathsf{rf}}}$ and returns completely to the subspace after this time. It remains outside the subspace only for the duration of the pulse. For ω_{rf} which are physically relevant ($\omega_{\mathsf{rf}} < 2\pi 100$ kHz and $0 < \Delta\omega < 2\pi 20$ kHz), a single RF pulse does not result in a logical π-rotation due to off-resonance effects. Experimentally we are limited to finite t_p and even our simple two logical qubit model system is sufficient to introduce several key challenges in implementing coherent control over logical qubits: (i) decoherence due to leakage outside the subspace during RF modulation periods, (ii) decoherence due to leakage outside the subspace after RF modulation, and (iii) loss of fidelity due to cumulative leakage with respect to the spectral density of the noise.

Figure 3-2 shows an illustrative example of the integrated effects of a π-pulse applied to the two spins in such a DFS on the purity ($Tr\{\rho^2\}$) and correlation with the ideal final state ($Tr\{\rho_{\mathsf{want}}\rho\}$) as a function of the ratio of the relaxation rate $1/T_2$ to the RF power ω_{rf}. The initial states were chosen from the four logical Pauli operators Eq. (3.3), and we make the approximation that the internal Hamiltonian

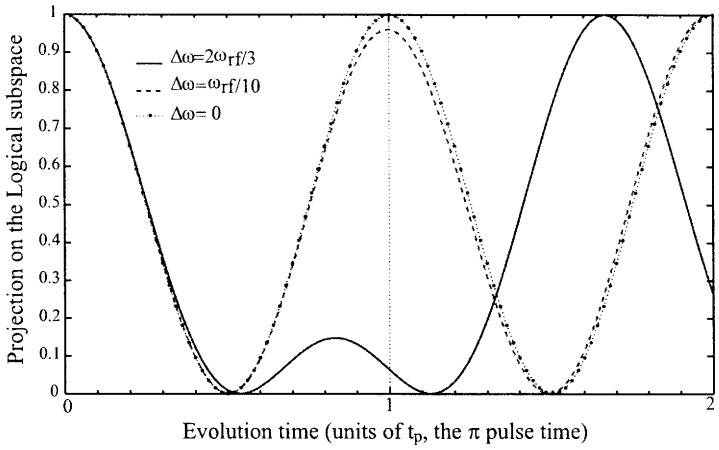

Figure 3-1: Leakage during an RF pulse. Shown above is the projection onto the logical subspace of a state initially inside the DFS, during application of an RF pulse for various ratios of $\frac{\Delta\omega}{\omega_{rf}}$. Defining the projection operator onto the logical subspace as P_L , we plot $p(t) = Tr[(P_L\rho(t))^2]/Tr(\rho(t)^2)$, for $t = 0 \rightarrow 2t_p$, where $\rho(t) = e^{-i\omega_{rf}t(\sigma_x^1+\sigma_x^2)}\sigma_z^L e^{i\omega_{rf}t(\sigma_x^1+\sigma_x^2)}$ and $\omega_{rf}t_p = \pi$. The logical state completely returns to the subspace after application of a π-pulse to both spins only when the spins have identical resonance frequencies ($\Delta\omega = 0$). If the ratio $\frac{\Delta\omega}{\omega_{rf}}$ is non-zero, as required for universality, the return to the logical subspace is imperfect (in particular, it is in general possible to go back to a state very close to the initial state in a time $t > t_p$, but it is much more difficult to implement a π rotation). A logical π-pulse using a single period of RF modulation is not possible, a more complex RF modulation, like composite pulses [85], strongly-modulating pulses [43, 115] or optimal control theory [71], is required. In the above model, $\frac{\omega_{rf}}{J} = 500$; the initial state of the system is σ_z^L.

is zero during the application of these π-pulses, with the noise superoperator along the z-axis, and relaxation constant T_2. As would be expected, the desired result (negating the state in the case of $\rho_0 = \sigma_y^L, \sigma_z^L$, or preserving it for $\rho_0 = \mathbf{1}^L, \sigma_x^L$) is rapidly degraded by the totally correlated decoherence during the π-pulse, unless the Rabi frequency is considerably faster than the relaxation rate. The increase in both the coherence and the correlation when the relaxation becomes fast compared to the rotation rate is due to a sort of "quantum Zeno" effect [109], so that the RF field itself is unable to rotate the state out of the DFS. This regime is known as motional narrowing in NMR relaxation theory [31]. In a complete analysis of the 2-spin case the effects shown in Fig. 3-1 must be combined to those in Fig. 3-2.

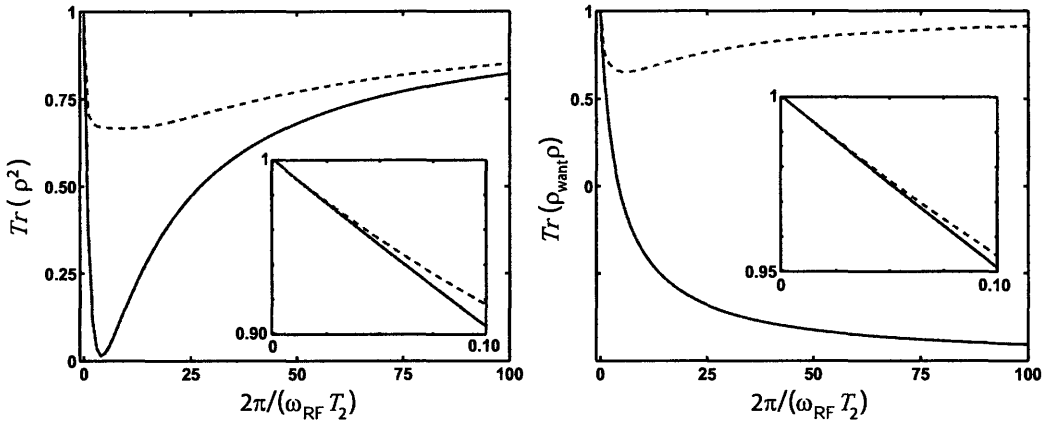

Figure 3-2: Fidelity loss due to subspace leakage. The plots illustrate the loss of fidelity due to totally correlated decoherence during the application of a π-pulse about the x-axis to the two spins of the DFS. The dashed curves (red) are for the initial states $\rho_0 = \mathbf{1}^L$ or $\rho_0 = \sigma_x^L$, while the lower curves (blue) are for $\rho_0 = \sigma_y^L$ or $\rho_0 = \sigma_z^L$. The left plot shows the trace of ρ^2 following the π-pulse as a function of the inverse product of the RF power ω_{rf} and the relaxation time T_2. The right plot shows the correlation with the ideal final state, i.e. the trace of $\rho_{\mathrm{want}}\rho$, following the π-pulse as a function of this same parameter.

3.2.4 Control in the Presence of Leakage

It has been established that (i) we must leave the subspace in order to generate control over our encoded qubit and (ii) decoherence effects during the pulse will compromise the information. If we assume that the noise properties of the system are well-enough behaved that (ii) can be neglected, decoherence will only occur due to information that has leaked from the subspace and remains there for some time. However, evolution of a state outside the subspace is precisely how we can generate the correct evolutions under $\mathscr{H}_0$ in order to perform effective unitary rotations inside the subspace. By leaving the subspace, allowing for a period of evolution, then returning to the subspace, the information begins and ends protected but can be compromised in between.

In the absence of symmetry to a noise process, time-honored methods for reducing dephasing were developed long before the onset of quantum information theory. Hahn's spin echo [57] shows that by modulating the system with a π-pulse dephasing due to static field (infinite correlation time) inhomogeneities are cancelled. Carr and

Purcell [23, 99] extended this concept by adding a train of π-pulses and showed that decay of coherence could be reduced for finite correlation time noise processes. A recent resurgence in these ideas have appeared in the quantum information literature. So called dynamical decoupling or "bang-bang" control [147] has been applied beyond magnetic resonance, for example to the control of decoherence in spin-boson models [142].

We analyze the fidelity of performing a encoded quantum operation under a collective noise model of a stationary process with a finite correlation time within the formalism of Stochastic Liouville Theory (SLT) [48, 58, 25] and cumulant expansions [80]. We show that high fidelity encoded quantum operations can be achieved by leaving the subspace and modulating at a rate much faster than the correlation time of the noise.

3.3 Stochastic Liouville Theory and Cumulant Averages

Stochastic Liouville theory is based on a semiclassical model of decoherence, in which the Hamiltonian at any instant in time consists of a deterministic and a stochastic part. In the simplest case of NMR T_2 relaxation, this typically takes the form

$$\mathscr{H}_{tot}(t) \;=\; \mathscr{H}_{det}(t) + \mathscr{H}_{st}(t) \;=\; \mathscr{H}_0 + \mathscr{H}_C(t) + \sum\nolimits_k \omega_k(t) Z_k \;, \tag{3.9}$$

where $\mathscr{H}_0$ is the static internal Hamiltonian, $\mathscr{H}_C(t)$ is the RF Hamiltonian, the $\omega_k(t)$ describe the phase shifts due to stochastic, time-dependent fluctuating fields and Z_k are the generators of each of these noise sources, i.e. operators which describe how these classical fields are coupled to the quantum system. In the two-spin DFS example considered previously, there is only one noise generator $Z = (\sigma_z^1 + \sigma_z^2)/2$ with $\omega(t) = \gamma B(t)$, which describes collective fluctuations parallel to the applied static magnetic field.

We now introduce a superoperator $\mathcal{L}(t)$ defined on Liouville (operator) space via

$$\mathcal{L}(t) \;=\; \mathscr{H}_{tot}^{*}(t)\otimes\mathbf{1}-\mathbf{1}\otimes\mathscr{H}_{tot}(t) \;=\; \mathcal{L}_{det}(t)+\sum\nolimits_{k}\omega_{k}(t)\mathcal{Z}_{k} \tag{3.10}$$

where $\mathcal{Z}_k = Z_k^*\otimes\mathbf{1}-\mathbf{1}\otimes Z_k$. This superoperator is the generator of motion for density operator ρ, meaning

$$|\rho(t)\rangle \;=\; \mathcal{U}\,|\rho(0)\rangle \;=\; \mathcal{T}\exp\!\Big(-i\int_0^t dt'\,\mathcal{L}(t')\Big)\,|\rho(0)\rangle \tag{3.11}$$

where $\mathcal{T}$ is the time-ordering operator and $|\rho\rangle$ represents the quantum state in Liouville space. Since what is actually observed in an experiment is the statistical average over the microscopic trajectories of the system $\big\langle|\rho(t)\rangle\big\rangle$, we have to take the ensemble average superpropagator to obtain $\big\langle|\rho(t)\rangle\big\rangle = \langle\mathcal{U}\rangle|\rho(0)\rangle = \mathcal{S}|\rho(0)\rangle$. The problem of calculating the average of the exponential of a stochastic operator has been solved by Kubo [80] using the cumulant expansion. In terms of the so-called "cumulant averages" $\langle\cdots\rangle_c$ (see Appendix A), the superpropagator is given by:

$$\mathcal{S}=\langle\mathcal{U}\rangle \;=\; \exp\!\Big(-i\int_0^t dt'\,\langle\mathcal{L}(t')\rangle_c-\tfrac{1}{2}\mathcal{T}\int_0^t dt_1\int_0^t dt_2\,\langle\mathcal{L}(t_1)\mathcal{L}(t_2)\rangle_c+\cdots\Big) \tag{3.12}$$

Providing the spectral norm $\|\int_0^t dt'\mathcal{L}(t')\| \ll 1$ for all $t>0$ we can safely neglect high order terms in the exponential's argument.

Similar expressions are obtained in the formalism of average Hamiltonian theory (AHT) [54] for the coherent (instead of stochastic) averaging of the system evolution under control Hamiltonians cyclic and periodic in time. Here we can obtain simplifications analogous to those encountered in AHT if we analyze the evolution in the interaction frame (called "toggling frame" in NMR) defined by the RF propagator $U_{\mathsf{rf}}(t)$ [55]. In this frame the noise operators acquire a further time-dependency (coherently imposed by the cyclic excitation) in addition to the stochastic time dependency of their coefficients $\omega_k(t)$. The total Hamiltonian in the toggling frame is

$$\tilde{\mathscr{H}}_{tot}(t) \;=\; \tilde{\mathscr{H}}_{det}(t)+\sum\nolimits_{k}\omega_{k}(t)\tilde{\mathcal{Z}}_{k}(t), \tag{3.13}$$

where the toggling frame equivalent operator $\tilde{O}$ of any given operator O is defined by $\tilde{O}(t) = U_{\mathsf{rf}}^{\dagger}(t)\, O\, U_{\mathsf{rf}}(t)$, with

$$U_{\mathsf{rf}}(t) \equiv \mathcal{T} \exp\Big(-i \int_0^t dt'\, H_{\mathsf{rf}}(t') \Big), \tag{3.14}$$

and $U_{\mathsf{rf}}(t_c) = \mathbf{1}$ for cyclic controls, so that the toggling frame and laboratory frame coincide at the end of each cycle.

This time-dependent change of basis in Liouville space induces a change of basis in the space of superoperators acting on Liouville space, as a result of which the noise super-generators $\mathcal{Z}_k$ also become time-dependent, i.e.

$$\tilde{\mathcal{Z}}_k(t) = \tilde{Z}_k(t) \otimes \mathbf{1} - \mathbf{1} \otimes \tilde{Z}_k(t)\ . \tag{3.15}$$

This facilitates the calculation of the average super-generator, $\bar{\mathcal{L}}$ and further allows the first-order effects of the RF fields upon the decoherence to be determined from the second-order terms in the cumulant expansion. In contrast, assuming as usual that the random variables $\omega_k(t)$ have a mean value of zero at all times, it would be necessary to analyze the third-order terms in order to obtain these results.

Returning now to the problem of greatest interest here, in which there is only one noise generator which describes totally correlated decoherence as above and the corresponding random variable $\omega(t)$ is stationary and mean zero, the results given in Appendix A imply that the first two cumulants in the toggling frame are:

$$\begin{aligned}
\tilde{\mathcal{K}}_1(t) &= \frac{1}{t} \int_0^t dt'\, \langle \mathcal{L}_{det}(t') + \omega(t') \tilde{\mathcal{Z}}(t') \rangle = \frac{1}{t} \int_0^t dt'\, \tilde{\mathcal{L}}_{det}(t') \\
\tilde{\mathcal{K}}_2(t) &= \frac{1}{t^2} \int_0^t dt_1 \int_0^{t_1} dt_2 \Big(\big[\tilde{\mathcal{L}}_{det}(t_1), \tilde{\mathcal{L}}_{det}(t_2) \big] + 2\, G(t_2 - t_1)\, \tilde{\mathcal{Z}}(t_1)\, \tilde{\mathcal{Z}}(t_2) \Big)
\end{aligned} \tag{3.16}$$

In the last line we have introduced the autocorrelation function $G(\Delta t) = \langle \omega(t + \Delta t) \omega(t) \rangle$ for the stationary random noise variable $\omega(t)$.

3.4 Refocusing noise with a Carr-Purcell sequence

We now use these results to analyze an implementation of a σ_x^L rotation on a two-spin DFS qubit. We will show that this implementation is applicable when the correlation time of the noise τ_c is long compared to the time required to apply a π-pulse to the spins. It consists of a $(\pi/2)$-rotation of both spins in the DFS qubit about the y-axis, followed by a Carr-Purcell-style sequence consisting of an even number $2n$ of π-pulses separated by equal time intervals $\tau = t/2n$, and finally the inverse $(\pi/2)$-rotation, i.e.

$$\left[\frac{\pi}{2}\right]_y \Big(-\tau - [\pi]_x - \tau - [\pi]_x \Big)^n \left[\frac{\pi}{2}\right]_{\bar{y}} \tag{3.17}$$

This transforms the weak $\sigma_z\sigma_z$ coupling between the two spins of the DFS qubit into $\sigma_x\sigma_x$, which projects to the σ_x^L operator within the DFS (Eq. 3.3). Setting $\tau = \phi/(2n\pi J)$ yields a rotation by an angle ϕ around the logical x-axis. Even though the state of the two spins is outside the DFS throughout the time $2n\tau$, the sequence of π-pulses is able to refocus the effects of the noise provided $\tau \ll \tau_c$.

Assuming instantaneous π-pulses, this follows from AHT since during any cycle $(0, 2\tau)$ the internal Hamiltonian in the toggling frame $\tilde{H}_{int}$ alternates between $+\Delta\omega(\sigma_x^1 - \sigma_x^2) + (\pi/2)J\sigma_x^1\sigma_x^2$ (in the interval $(0,\tau)$) and $-\Delta\omega(\sigma_x^1 - \sigma_x^2) + (\pi/2)J\sigma_x^1\sigma_x^2$ (in the interval $(\tau, 2\tau)$), so that the zeroth-order average Hamiltonian is just $\bar{\mathscr{H}}^{(0)} = (\pi/4)\sigma_x^1\sigma_x^2 = (\pi/4)\sigma_x^L$. This is in fact also the average Hamiltonian to all orders, since the toggling frame Hamiltonian commutes at all time, and the first cumulant is just the corresponding superoperator $\tilde{\mathcal{K}}_1 = \mathcal{K}_1 = (2\tau)^{-1}(\bar{\mathscr{H}}^* \otimes \mathbf{1} - \mathbf{1} \otimes \bar{\mathscr{H}})$.

Again because the toggling frame Hamiltonians commute, the deterministic part of the Liouvillian $\tilde{\mathcal{L}}_{det}(t)$ does not contribute to $\tilde{\mathcal{K}}_2 = \mathcal{K}_2$ at the end of each cycle, nor at the end of the entire sequence. The second cumulant is determined by the stochastic part alone:

$$\mathcal{K}_2 = \frac{2}{(2n\tau)^2} \int_0^{2n\tau} dt_1 \int_0^{t_1} dt_2\, G(t_2 - t_1)\tilde{\mathcal{Z}}(t_1)\tilde{\mathcal{Z}}(t_2)\ . \tag{3.18}$$

Because each π-pulse simply changes the sign of $\tilde{\mathcal{Z}}(t)$ from the preceding interval, it

follows that $\tilde{\mathcal{Z}}(t) = +\mathcal{Z}_x$ if t is in an even interval $\big(2k\tau,\,(2k+1)\tau\big)$ and $\tilde{\mathcal{Z}} = -\mathcal{Z}_x$ if t is in an odd interval $\big((2k-1)\tau,\,2k\tau\big)$, where k is an integer $0 \le k \le n$ and $\mathcal{Z}_x$ is the noise super-generator rotated along the x-axis. In addition, since the random variable $\omega(t)$ is stationary, the double integral over any two intervals i and i' will be equal to the double integral over any other pair j and j' providing that $|i - i'| = |j - j'|$. These observations allow the overall double integral in Eq. (3.18) to be expressed as

$$\mathcal{K}_2 \;=\; \frac{2\,\mathcal{Z}_x^2}{(2n\tau)^2}\left(2nA + \sum_{m=1}^{2n-1}(2n-m)\,B_m\right) \;\equiv\; \mathcal{Z}_x^2\,\zeta\;, \tag{3.19}$$

where

$$A \;\equiv\; \int_0^{\tau} dt_1 \int_0^{t_1} dt_2\, G(t_1 - t_2) \tag{3.20}$$

and

$$B_m \;\equiv\; (-1)^m \int_{m\tau}^{(m+1)\tau} dt_1 \int_0^{\tau} dt_2\, G(t_1 - t_2) \tag{3.21}$$

for $m = 1, \ldots, 2n-1$.

In the case of Gaussian noise with autocorrelation function $G(t) = \Omega^2 e^{-t/\tau_c}$, one finds that

$$A \;=\; (\Omega\tau_c)^2\left(e^{-\tau/\tau_c} + \tau/\tau_c - 1\right) \tag{3.22}$$

and

$$B_m \;=\; \bar{B}(-1)^m\, e^{-m\tau/\tau_c}, \quad \bar{B} = (\Omega\tau_c)^2 e^{-\tau/\tau_c}(e^{\tau/\tau_c} - 1)^2. \tag{3.23}$$

On evaluating the geometric series in Eq. (3.19), one obtains the closed form

$$\zeta \;=\; \frac{2\,\Omega^2\tau_c^2}{(2n\tau)^2}\left[2n\Big(\tau/\tau_c + e^{-\tau/\tau_c} - 1\Big) + \left(\frac{1 - e^{-\tau/\tau_c}}{1 + e^{-\tau/\tau_c}}\right)^2\Big(1 - 2n\big(1 + e^{-\tau/\tau_c}\big) - e^{-2n\tau/\tau_c}\Big)\right], \tag{3.24}$$

which is easily shown to go to zero as $\tau/\tau_c \to 0$ [1]. We can quantify the protection afforded by the CP-sequence by taking the entanglement fidelity [104, 44] of the superoperator with the ideal propagator for the sequence as a measure of its efficacy,

[1] In the limit $\tau/\tau_c \to \infty$ the behavior of ζ depends on the noise strength: If a constant noise strength is assumed,$\zeta \to 0$ as $\frac{\Omega^2}{\tau/\tau_c}$. If instead we assume $\Omega\tau_c$ =cst, $\zeta \to \infty$, since it is now $\zeta \propto \frac{\tau/\tau_c}{2n\tau^2}$, and the fidelity will go to zero.

$F = Tr\{U_{\rm id}^{-1}S\}/Tr\{U_{id}^{-1}U_{id}\}$. Since the unitary part of the evolution commutes with the noise and gives the ideal propagator, the fidelity is just the trace of the superoperator, which for a single two-spin DFS qubit is

$$F(\zeta) = Tr\{e^{-Z_x^2\zeta(2n\tau)^2/2}\} = \tfrac{1}{8}\left(3 + 4\,e^{-2\zeta n^2\tau^2} + e^{-8\zeta n^2\tau^2}\right). \qquad (3.25)$$

The fidelity for cycles of CP-sequences of length 4 and 16 are plotted in Figure 3-3. As expected, it shows an improvement for an higher number of intervals and shorter time spacings with respect to the correlation time.

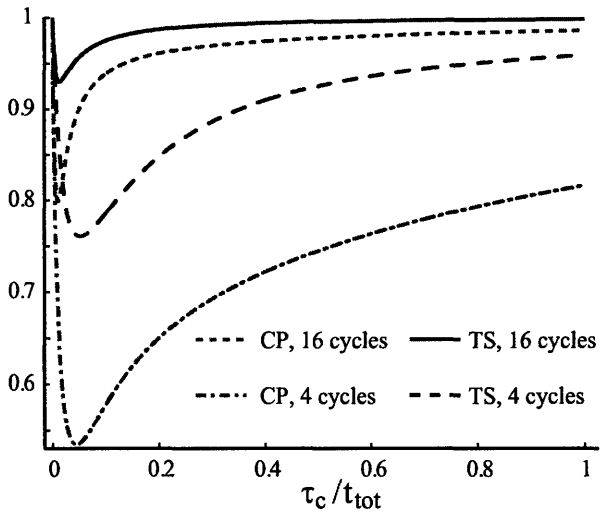

Figure 3-3: Gate fidelity as a function of the correlation time for 4 and 16 cycles of the Carr-Purcell (CP) and Time-Suspension sequences (TS). The noise strength Ω was fixed at 1 Hz., while the duration of the entire sequence was fixed at $t_{tot} = 4$ sec (where $t_{tot} = 2n\tau$ for the CP sequence and $t_{tot} = 4n\tau$ for the TS sequence). The increase in fidelity at very short correlation times is due to the phase fluctuations becoming so fast that they produce essentially no effect at the given noise strength Ω.

It is interesting to also consider a simple sequence that completely refocuses the internal Hamiltonian, namely

$$\left(-\tau - [\pi]_x^1 - \tau - [\pi]_x^2 - \tau - [\pi]_x^1 - \tau - [\pi]_x^2\right)^n, \qquad (3.26)$$

where the superscripts on the pulse angles now refer to the spin affected by the pulses

and n is an integer. This will be referred to in the following as the Time-Suspension (TS) sequence. The average Hamiltonian is now zero, while the noise operator in the toggling frame is $\tilde{Z}_1 = \pm(\sigma_z^1 + \sigma_z^2)/2$ in the intervals 1 and 3 respectively and $\tilde{Z}_2 = \pm(\sigma_z^1 - \sigma_z^2)/2$ in the other two intervals. If we sandwich the TS-sequence between a pair of $(\pi/2)$-pulses as we did for the CP, and again assume a stationary Gaussian distribution of totally correlated noise, we find it is more effective at protecting the system from decoherence even when the number of π-pulses on each spin and the cycle time is the same, since the effective modulation rate is then faster (there is a pulse every $\tau/2$). Indeed the relaxation superoperator for the TS-sequence is $\mathcal{K}_2 = \zeta_1(\mathcal{Z}_1^2 + \mathcal{Z}_2^2) + \zeta_2 \mathcal{Z}_1\mathcal{Z}_2$ (see [21] for details), where $\mathcal{Z}_k = Z_k \otimes \mathbf{1} - \mathbf{1} \otimes Z_k$ $(k = 1, 2)$ and:

$$\begin{aligned} \zeta_1 = \; & \frac{\omega^2\tau_c^2}{16n^2\tau^2}\left[\left(\frac{1-e^{\tau/\tau_c}}{1+e^{2\tau/\tau_c}}\right)^2 \left(e^{-4n\tau/\tau_c}\left(ne^{4\tau/\tau_c} - n + 1\right) - 1\right) e^{-3\tau/\tau_c}\right. \\ & \left. + 2n\frac{\tau}{\tau_c} + n\left(e^{-2\tau/\tau_c} - 1\right)\left(2 - e^{-\tau/\tau_c}\right)\right] \end{aligned} \tag{3.27}$$

$$\zeta_2 = \frac{\omega^2\tau_c^2}{16n^2\tau^2}\frac{\left(1 - e^{\tau/\tau_c}\right)^2 e^{-4\tau/\tau_c}}{1 + e^{2\tau/\tau_c}}\left[e^{-4n\tau/\tau_c}\left(ne^{4\tau/\tau_c} - n + 1\right) + ne^{4\tau/\tau_c} - (n+1)\right] \tag{3.28}$$

The fidelity is therefore:

$$\begin{aligned} F(\zeta_1, \zeta_2) \; &= \; Tr\{\exp\left(-\zeta_1(\mathcal{Z}_1^2 + \mathcal{Z}_2^2)(4n\tau)^2/2 - \zeta_2\mathcal{Z}_1\mathcal{Z}_2(4n\tau)^2/2\right)\} \\ &= \; \tfrac{1}{2}\, e^{-\zeta_1(4n\tau)^2}\left(\cosh(-\zeta_1(4n\tau)^2) + \cosh(-\zeta_2(4n\tau)^2/2)\right) . \end{aligned} \tag{3.29}$$

3.5 Simulation of a selective DFS qubit gate

It is particularly interesting to study how these schemes perform for realistic control parameters, with finite rf power. The analytical expressions found above for the attenuation due to totally correlated noise with a stationary Gaussian distribution apply only to the special case of ideal pulses (instantaneous in time), but similar behavior is expected under more realistic assumptions on the control fields. In particular, to act selectively only on some of the spins we would have to use the technique

of SMP [43, 115], thereby inducing a much more complex dynamics on the system for which closed form solutions are not available, but which can be studied via numerical simulations.

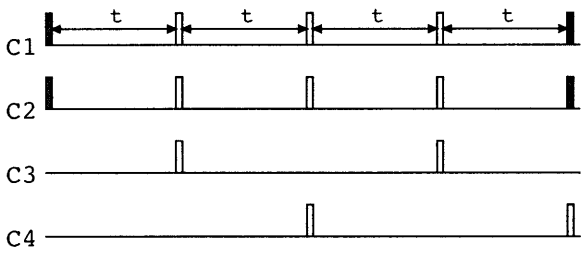

Figure 3-4: Pulse sequence for a rotation about σ_x^{1L} of a two-spin DFS qubit. The evolution of a second DFS qubit under the internal Hamiltonian of the system is refocused. The darker pulses represent $\frac{\pi}{2})_y$ rotations while the lighter pulses are π rotations.

We have studied the accuracy with which a rotation about the logical x-axis can be performed by numerical simulations. These simulations included the internal Hamiltonian, the external control Hamiltonian and totally correlated noise $\omega(t)$ with a stationary, Gaussian distribution. The evolution was discretized into equal time steps, for each of which we calculated the propagator $U(t_k) = \exp(-i(H_{int}+H_{rf}(t_k)+\omega(t_k)Z)\delta t)$. The noise strength $\omega(t_k)$ is extracted from a multivariate gaussian probability distribution, with a covariance matrix $C_{j,k} = \Omega^2 e^{-|j-k|\delta t/\tau_c}$, where j and k are integers indicating the time intervals. We then take the average of the superoperators $S_i = \bar{U}_i \otimes U_i$ obtained over a sequence of evolutions differing only by the random number seed.

We have performed one set of simulations using a fictitious two-spin molecule (chemical shift difference: $\Delta\omega = 600$Hz, scalar coupling $J = 50Hz$), and another using the internal Hamiltonian of ^{13}C-labeled crotonic acid (see Section 4.2 for details). Both sets of simulations were performed with instantaneous ideal pulses, and again with the strongly-modulating pulses used in actual NMR experiments.

In the case of the two-spin molecule, since selective pulses are not required, we compare the results of SMP pulses with the dynamics under short, collective pulses (called "hard pulses" in Section 2.3, π-pulse time $t_p = 2\mu s$). SMP appear to perform

better even if they require longer times. In the crotonic acid simulations, the sequence was designed not only to implement a selective $\pi/2$-rotation about the logical x-axis on the two spins in one DFS qubit, but to also refocus the evolution of the other two spins under the molecule's internal spin Hamiltonian (see Fig. 3-4).

The fidelities of these simulations are plotted as a function of correlation time in Fig. 3-5. Compared to simulations with ideal pulses, we observe a drop in the fidelity due to the finite duration of each pulse. This drop is only in part accounted for by the increase in time in the cycle length. Nevertheless, the effectiveness of the CP-sequence in preventing decoherence during the unavoidable excursions from the DFS is evident.

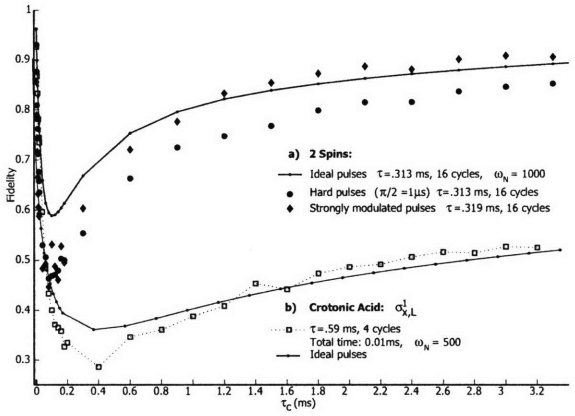

Figure 3-5: Fidelity for ideal and real pulses. a) Two-spin CP sequence implementing a $\pi/2$ rotation about the logical σ_x (A fictitious spin system with $\Delta\omega = 600$Hz and J=50Hz was used in the simulation) b) $\pi/2$ rotation about the logical σ_x^{1L} for Crotonic acid (see 4.2 for molecule data).

3.6 Conclusions

We have considered the difficulties of operating on quantum information stored in encoded qubits without losing the protection from decoherence offered by the encoding. Although we have focused on the Hamiltonians and control fields operative in NMR for concreteness, similar challenges will be encountered in other functional realizations of quantum information processing, including superconducting qubits, ion traps

and quantum optics. The most significant result is a demonstration that in many realizations, including NMR, the implementation of a universal set of quantum gates may be considerably simplified by briefly leaving the DFS while using dynamical decoupling to inhibit decoherence during these excursions. This approach depends on the ability to operate on the system on time scales short compared to the correlation time of the noise. In evaluating various possible realizations of quantum information processing, it is important to characterize not only the decoherence rate, but also the spectral density of the underlying noise, to verify that the gate speed is sufficient to allow the noise to be refocused. We provided here numerical results relative to realistic conditions in an NMR experimental implementation, which build on and confirm the previously reported theoretical results. In addition to its role as a facile testbed for quantum information processing, NMR spectroscopy provides widely applicable tools such as Average Hamiltonian/Liouvillian theory by which one can calculate the efficacy of control sequences for refocusing the noise, and devise new ones for specific noise generators.

Chapter 4

Experimental Demonstration of Encoded Logical Operations

In this chapater, we demonstrate a quantum logical gate between a pair of logical qubits using liquid state NMR techniques. First, we must prepare the nuclear spin ensemble for quantum processing using pseudo-pure states. Next, we entangle the two logical qubits using encoded quantum logic. As developed in the previous chapter, we use the scheme for generating logical rotations of encoded qubits when the control Hamiltonian drives the encoded information outside of a protected subspace. Provided the noise correlation time is slow compared to the rate of modulation, we can implement higher fidelity operations despite the significant leakage. The analysis of the results assesses how well one can implement logical quantum operations in the presence of leakage.

4.1 Implementation

4.1.1 State Preparation

In the standard NMR model for liquids comprised of small molecules with magnetic nuclei, the microscopic spin Hamiltonian for a single molecule in high-field well approximates the coherent dynamics of the system. The microscopic systems behave as

non-interacting to first order: all intermolecular dipole-dipole interactions are averaged out and appear as mechanisms for relaxation. Thus, liquid state NMR provides an excellent means for exploring engineering of unitary dynamics. If we specify the thermal equilibrium state of this ensemble quantum system, for a large number ($\approx 10^{20}$) molecules we find that the initial state of the system is highly mixed at temperatures where the system remains a liquid (around 300K). This means that if we could select a single molecule from the sample, statistically each nuclear magnetic moment would be as likely to be up (aligned with the field) as it would to be down (anti-aligned with the field), with only a slight preference (1 part in 10^6) for alignment. This so called high-temperature, high-field approximation is applied to the canonical Boltzmann distribution for an ensemble of quantum systems where the initial state of a system of N spins 1/2 is:

$$\rho_{\text{eq}} = \frac{e^{-\beta\mathscr{H}_0}}{\mathcal{Z}} \tag{4.1}$$

$$\approx \frac{\mathbf{1}}{2^N} - \beta\hbar B_0 \sum_{j=1}^{N} \gamma_j I_z^j + \mathscr{O}\big((\beta\hbar B_0)^2\big) \tag{4.2}$$

where $\beta = 1/kT$ and $\mathcal{Z}$ is the partition function of the system. For typical fields and temperatures for liquid phase NMR, the Taylor expansion of the Hamiltonian can be truncated to first order in $(\beta\hbar B_0\gamma)$. All correlations due to the scalar couplings are much weaker and can also be dropped; also, $\mathcal{Z} \approx \mathbf{1}$. This equilibrium state poses a problem for using NMR molecules as small-scale quantum information processors because the standard model of quantum computation requires pure quantum states as fiducial inputs at the beginning of a quantum algorithm.

Full Pseudo-pure states

For this implementation, we use a spatially-averaged pseudo-pure state[1]. The implementation expressed as quantum logic gates is shown in Figure 4-1. First, we must breakdown the quantum logic gates into a series of single-spin rotations and delays

[1]See Appendix B for details about initialization of thermal spin states.

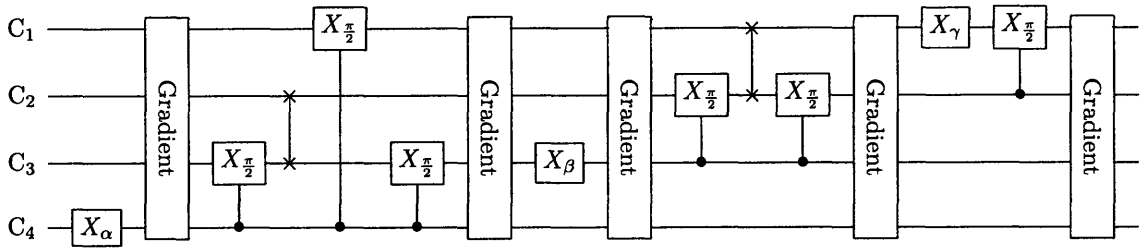

Figure 4-1: Full Pseudo-Pure State Preparation Circuit.We represent single qubit rotations by square boxes, controlled rotations by closed circles on the controlling qubit linked to the applied rotation on the controlled qubit; swaps gate by two crosses on the swapped qubits, connected by a vertical line. Notice the number of controlled operations, each requiring a time of the order of the inverse coupling strength, and SWAP gates, each requiring three times the inverse coupling strength. The single-qubit rotations above have the values $\alpha \approx \frac{9}{20}\pi$, $\beta \approx \frac{2}{5}\pi$, and $\gamma \approx \frac{2}{7}\pi$ which account for the scaling of the signal-to-noise compared to the equilibrium state.

with the appropriate refocusing pulses to avoid unwanted evolution from chemical shift and scalar coupling terms in the Hamiltonian [114]. Pulsed magnetic field gradients introduce a spatially-dependent Hamiltonian and provide a method for implementing non-unitary quantum dynamics when we carry out measurements over the entire ensemble. We use strongly-modulating pulses (Chapter 2) to generate all single-spin rotations and model the system as an incoherent mixture of ensembles experiencing slightly different RF field strengths to improve the average gate fidelity of an inherently incoherent quantum process [13].

Subsystem Pseudo-pure states

When we would like to study the control of logical qubits, we know implicitly that the protected quantum information lies in a logical subsystem of dimension d_s embedded within a larger Hilbert space of physical qubits of dimension d_f, where $d_s < d_f$. In the case of initial states that are made pure over the entire Hilbert space, we must average over an exponentially increasing number of permutations of the eigenvalues in order to effectively purify the system. If we work with logical qubits it is not necessary to purify the parts of Hilbert space outside the logical degrees of freedom. Hence, we can simplify the state preparation sequence when investigating logical qubits.

To present the general structure that encoding imposes to the Hilbert space, we adopt the subsystem approach [75, 70], that provides a unified description for Quantum Error Correction (QEC) [76, 20, 136], Decoherence Free Subspaces (DFS) [151, 38, 88] and Noiseless Subsystems (NS) [146, 33, 87, 86]. A Hilbert space $\mathcal{H}$ of dimension $d = 2^N$ is used to encode $l \leq N$ qubits of information, protected against a set of noise operators $\{\hat{J}_\alpha\}$. With a change of basis to a direct sum[2] $\mathcal{H} \cong \bigoplus_i \mathcal{L}_i \otimes \mathcal{S}_i$, the noise acts only on the subsystems $\mathcal{S}_i$ (the syndrome) while the subsystems $\mathcal{L}_i$ are noiseless (for simplicity, we will often refer to a decomposition: $\mathcal{H} = \mathcal{L} \otimes \mathcal{S} \oplus \mathcal{R}$, with $\mathcal{R}$ an unprotected subspace).

If we evolve the system with logical operations, acting only on the encoded subspace $\mathcal{L}$, the information within the subspace $\mathcal{L}$ will not leak out or mix with the orthogonal spaces and will act separably on the syndrome space during logical unitary transformations. This preserves the purity of the encoded subspace under the action of $\hat{J}$. Therefore, the remaining subsystems $\mathcal{S}_i$ and subspace $\mathcal{R}$ can remain in a mixed state.

The state preparation procedure that bears the most resemblance to the method we propose is logical labeling [49], which uses a unitary transformation to change the equilibrium distribution of spin states into one where a subsystem of the Hilbert space is pseudo-pure conditional on a physical spin having some preferred orientation. The parts of Hilbert space that remain mixed are of no use to the computation. It can be shown that a $m-$qubit pseudo-pure state can be stored among the Hilbert space of $N-$qubits provided the inequality $(2^m - 1) \leq \frac{N!}{((N/2)!)^2}$ is satisfied. A key insight is that in the study of encoded qubits, one need not take this $m-$qubit effective pure state and perform an encoding of $l-$logical qubits under the hierarchy $l < m < N$: Instead, a l-qubit encoded state can be prepared directly from the equilibrium state of N qubits.

If information is encoded in a subsystem of dimension 2^l, with a corresponding syndrome subsystem, $\mathcal{S}$ of dimension d_s that we can leave in a mixed state, the number of zero eigenvalues in this subsystem pseudo-pure state is $(2^l - 1)d_s$. We can

[2]Further action is required in the case of QEC codes [146].

create a state that is pure over the logical degrees of freedom as long as there are at least as many zero eigenvalues in the thermal state as in the l-qubits pure state: $(2^l - 1) \leq \frac{N!}{((N/2)!)^2 d_s}$. However, the eigenvalue spectrum of the equilibrium density matrix of N spins-1/2 ($\lambda(\rho_{eq}) = \{N, N-2, ..., -N\}$) will most generally not generate the necessary eigenvalue spectrum required for decoding [3] the l-qubits of information into l physical qubits without error. Thus, an averaging process akin to the ones used for generating pseudo-pure states over the entire Hilbert space must also be used.

For the full pseudo-pure state creation, the eigenvalue spectrum of the entire Hilbert space is arranged such that all of the 2^N eigenvalues are identical save one particular entry. With an encoded state, we have at least one other parameter to vary within the eigenvalue spectrum in order to minimize the loss of signal due to the averaging. Under a particular encoding the Hilbert space is transformed to $\mathcal{H} \cong \bigoplus_i \mathcal{L}_i \otimes \mathcal{S}_i$. In the encoded representation the initial state will have the form:

$$\rho_{spps} = \bigoplus_i a_i \left(|\psi\rangle_L^i \langle\psi|_L^i \otimes \frac{\mathbf{1}_S^i}{d_{s_i}} \right) \tag{4.3}$$

$|\psi\rangle_L^i$ is a fiducial state within the encoded subspace. The dimension of the i^{th} syndrome is d_{s_i}; a_i are subspace weighting coefficients, such that $\sum_i a_i = 1$, ensuring a unit trace of ρ_{spps}. To simplify the analysis, we have set the syndrome to the identity state.

If we encode l logical qubits among N physical qubits, with a syndrome subsystem $\mathcal{S}$ of dimensions 2^s, we move the information into a single subspace and the non-

[3] An important requirement for the subsystem pseudo-pure states is the ability to decode: the use of a mixed state should not introduce a mixing of the information contained in the logical qubits and in the unprotected subsystems, even when the information is transferred back to physical qubits by decoding. For unital maps, setting the unprotected subsystem to the identity state will satisfy this requirement without any further action required on the decoded state (notice that other mixed states are possible for particular encodings). For a DFS or a NS, not being able to apply the simple decoding operation to transfer the full information back to the physical qubits is inconvenient, as logical observables are in general difficult to measure experimentally since they are usually given by many-body states in the basis of the physical system. In the case of QEC the decoding involves also a correction step. If the unprotected part of the Hilbert space has evolved, it is no longer possible to perform a unique correction operation, valid for any input state.

information carrying subspace can have any state:

$$\rho_{spps} = a\left(|\psi\rangle\langle\psi|_L \otimes \frac{\mathbf{1}_S}{2^s}\right) \oplus b\,\rho_{\mathcal{R}} \tag{4.4}$$

with b chosen in accordance with $\rho_{\mathcal{R}}$ such that $Tr[\rho_{spps}] = 1$. Again, we sacrifice a general analysis for simplicity and insight, setting $\rho_{\mathcal{R}}$ to the identity state, thus relating b to the dimensionality of the subsystem and a:

$$\rho_{spps} = a\left(|\psi\rangle\langle\psi|_L \otimes \frac{\mathbf{1}_S}{2^s}\right) \oplus \frac{1-a}{2^N - 2^{s+l}}\mathbf{1}_R, \tag{4.5}$$

We quantify the signal arising from observable magnetization of the state ρ as:

$$S(\rho) = \sqrt{Tr\{\sum \sigma_z^i \rho\}^2 + Tr\{\sum \sigma_x^i \rho\}^2 + Tr\{\sum \sigma_y^i \rho\}^2} \tag{4.6}$$

and seek to maximize $S(\rho(a))$ for the l qubit encoding about N qubits. A full analysis [22] shows that for $a = d_S 2^{1-N}$ the signal is maximal (See Appendix B).

For multiple encodings of more than one logical qubit, each being protected against some noise, or to concatenate different encodings, a tensor structure of encoded qubits arises naturally. We also analyze this second type of construction, that can bring a further enhancement of the signal. We assume here that we encode one logical qubit in n physical qubits – each being a subsystem pseudo-pure state – and we build a logical $l-$qubit state with the tensor product of these encoded qubits. The Hilbert space can be written as a tensor product of direct sums as: $\mathcal{H} = \bigotimes_{i=1}^{l}(\mathcal{L}_i \otimes \mathcal{S}_i \oplus \mathcal{R}_i)$.

The corresponding partially mixed states differ with respect to the previous ones, in that the subspaces not used to store protected information ($\mathcal{R}_{\text{total}}$) are not maximally mixed:

$$\rho_{spps} = (a_1|\psi\rangle\langle\psi|_{L_1} \otimes \tfrac{\mathbf{1}_{S1}}{2^{s1}} \oplus \tfrac{1-a_1}{2^n - 2^{s1+1}}\mathbf{1}_{R1}) \otimes (a_2|\psi\rangle\langle\psi|_{L_2} \otimes \tfrac{\mathbf{1}_{S2}}{2^{s2}} \oplus \tfrac{1-a_2}{2^n - 2^{s2+1}}\mathbf{1}_{R2}) \otimes \ldots \tag{4.7}$$

Appendix B shows the analysis for maximizing the signal for the special case of $a_i = a$.

For our system of two-logical qubits protected against collective z noise, we have two subspaces, with $d_{S1} = d_{S2} = 0$. We chose to prepare the initial state of the encoded subspace to be $|00\rangle_L$. If we use the first method of SPPS creation, the state is:

$$\rho_{spps_1} = a|0101\rangle\langle 0101| \oplus \frac{1-a}{12}\,\mathbf{1}_R \tag{4.8}$$

with $a = 1/8$ for a maximum signal $S = 1/2$, the state represented as Pauli operators has three- and four-body correlations:

$$\begin{aligned}\rho_{spps_1} \;=\; & \tfrac{1}{16}\mathbf{1} + \\ & \tfrac{1}{128}\Big(\sigma_z^1 - \sigma_z^2 + \sigma_z^3 - \sigma_z^4 + \\ & \sigma_z^2\sigma_z^4 - \sigma_z^2\sigma_z^3 - \sigma_z^1\sigma_z^4 + \sigma_z^1\sigma_z^3 + \\ & \sigma_z^2\sigma_z^3\sigma_z^4 - \sigma_z^1\sigma_z^3\sigma_z^4 + \sigma_z^1\sigma_z^2\sigma_z^4 - \sigma_z^1\sigma_z^2\sigma_z^3\Big) + \\ & \tfrac{1}{96}\Big(\sigma_z^3\sigma_z^4 + \sigma_z^1\sigma_z^2 - \sigma_z^1\sigma_z^2\sigma_z^3\sigma_z^4\Big)\end{aligned} \tag{4.9}$$

However, if we choose the second method, a single logical qubit SPPS for this encoding is:

$$|01\rangle\langle 01| = \frac{\mathbf{1}_L + \sigma_{z,L}}{2} = \frac{\mathbf{1} + \sigma_z^1 - \sigma_z^2 - \sigma_z^1\sigma_z^2}{4} \tag{4.10}$$

The Hilbert space can be written as a direct sum of the logical subspace $\mathcal{L}$ (spanned by the basis $|01\rangle$ and $|10\rangle$) and its complementary subspace $\mathcal{R}$ (spanned by the basis $|00\rangle$ and $|11\rangle$). If we add the identity on the $\mathcal{R}$ subspace to the logical pure state, we obtain a mixed state that is equivalent in terms of its behavior on the logical degrees of freedom:

$$\rho_{L_1} = \frac{1}{4}(\mathbf{1} + \frac{\sigma_z^1 - \sigma_z^2}{2}) = \frac{1}{4}(\mathbf{1} + \sigma_{z,L}) = |0\rangle\langle 0|_L \oplus \frac{\mathbf{1}_R}{4} \tag{4.11}$$

The traceless part of this state is simply $\propto \sigma_z^1 - \sigma_z^2$: From thermal equilibrium, a unitary operation is sufficient to obtain this state, so no signal is lost. The subsystem pseudo-pure state that one obtains with this method requires less averaging to implement the non-unitary transformation. We expect such transformation to result

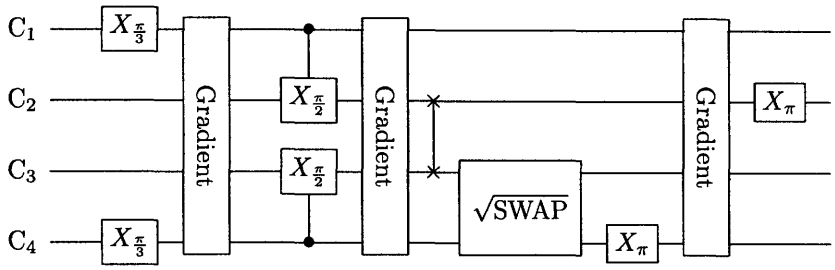

Figure 4-2: Subsystem Pseudo-Pure State Preparation Circuit.

in higher SNR since less purification of the state is required. Also, the lack of a $\sigma_z^1\sigma_z^2$ indicates that subsystem pseudo-pure states will in general require fewer multi-spin correlations, leading to shorter preparation sequences.

By taking the product space of two of these states:

$$\begin{aligned}
\rho_{spps} &= \tfrac{1}{16}(\mathbf{1}_L^1 + \mathbf{1}_R^1 + \sigma_{z,L}^1) \otimes (\mathbf{1}_L^2 + \mathbf{1}_R^2 + \sigma_{z,L}^2) \\
&= \tfrac{1}{16}(\mathbf{1}^{1,2} + \tfrac{\sigma_z^1 - \sigma_z^2}{2}) \otimes (\mathbf{1}^{3,4} + \tfrac{\sigma_z^3 - \sigma_z^4}{2}) \\
&= \left(\tfrac{1}{2}|01\rangle\langle 10| \oplus \tfrac{1}{4}(|00\rangle\langle 00| + |11\rangle\langle 11|)\right)_{12} \otimes \\
&\qquad \left(\tfrac{1}{2}|01\rangle\langle 10| \oplus \tfrac{1}{4}(|00\rangle\langle 00| + |11\rangle\langle 11|)\right)_{34}
\end{aligned} \tag{4.12}$$

A non-unitary operation is required to obtain this state, but the resulting scaling factor (α) for our implementation is 2/3. The scaling factor for creating the full pseudo-pure state is 4/15. The preparation procedure is also less complex, since it only requires preparing up to 2−body terms ($\sigma_z^i\sigma_z^j$) instead of the 4−body term ($\sigma_z^1\sigma_z^2\sigma_z^3\sigma_z^4$) necessary for the full pseudo-pure state [4].

4.1.2 Quantum Circuit

As a demonstration of our control, we generate entanglement between two logical qubits by implementing logical versions of typical quantum gates. Given two qubits in the fiducial ground state $|00\rangle$, one can create entanglement between the two qubits by rotating the first qubit into a superposition of $|0\rangle$ and $|1\rangle$ and then performing a

[4] An N-body term involves interactions among all N spins; usually only some of the couplings among spins are strong enough to permit fast two-qubit operations

two-qubit gate on the resultant state. One such construction is a Hadamard gate, followed by a controlled-not:

$$|00\rangle \xrightarrow{\mathrm{H}_1\otimes 1} \frac{1}{\sqrt{2}}(|00\rangle + |10\rangle) \xrightarrow{\mathrm{C}_1\mathrm{NOT}_2} \frac{1}{\sqrt{2}}(|00\rangle + |11\rangle) = |\Phi_+\rangle \tag{4.13}$$

The creation of a logical Bell state amounts to implementing logical versions of Hadamard and CNOT gates. Thus we express these gates using the complete basis spanned by the logical operators in Eq. (3.3).The Hadamard gate on a logical qubit is specified, up to a global phase, as

$$iU_{\mathrm{H}} = i\frac{\sigma_x^L + \sigma_z^L}{\sqrt{2}} = e^{-i\frac{\pi}{8}\sigma_y^L} e^{-i\frac{\pi}{2}\sigma_x^L} e^{i\frac{\pi}{8}\sigma_y^L} \tag{4.14}$$

The unitary operator for implementing a CNOT gate can be decomposed into a product of unitary operators of the form of single logical spin rotations and couplings of the 'ZZ' form similar to that of Eq. (2.6):

$$\begin{aligned} U_{C_0NOT} &= E_+^{1L}\sigma_x^{2L} + E_-^{1L}\mathbf{1}^{2L} \\ &= e^{i\frac{\pi}{4}\mathbf{1}^{1L}\mathbf{1}^{2L}} e^{-i\frac{\pi}{4}\sigma_y^{2L}} e^{-i\frac{\pi}{4}(\sigma_z^{1L}+\sigma_z^{2L})} e^{-i\frac{\pi}{4}\sigma_z^{1L}\sigma_z^{2L}} e^{i\frac{\pi}{4}\sigma_y^{2L}} \end{aligned} \tag{4.15}$$

If we replace all of the σ_μ^L by the two-spin versions according to Eq. (3.3), this would amount to implementing many different two-qubit gates. Not all of the terms in the expansion from logical qubits to physical qubits are relevant to the information within the logical subspace. Many simplifications are possible. For instance, when a logical operator consists of a sum of commuting bilinear terms, it may suffice to drop all but one of the terms in the sum and add a constant scaling factor provided this simplified unitary has the same effect as the full unitary on a state within the logical encoding. One example is the isomorphism between a rotation of $\frac{\pi}{2}$ about σ_x^{1L} and a π rotation about $\sigma_x^1\sigma_x^2$ or $\sigma_y^1\sigma_y^2$:

$$
\begin{aligned}
e^{-i\theta\frac{\sigma_x^1\sigma_x^2+\sigma_y^1\sigma_y^2}{2}} &= e^{-i\theta\frac{\sigma_x^1\sigma_x^2}{2}}e^{-i\theta\frac{\sigma_y^1\sigma_y^2}{2}} \\
&= \left(\cos(\frac{\theta}{2})\mathbf{1} - i\sin(\frac{\theta}{2})\sigma_x^1\sigma_x^2\right)\left(\cos(\frac{\theta}{2})\mathbf{1} - i\sin(\frac{\theta}{2})\sigma_y^1\sigma_y^2\right) \\
&= \cos^2(\frac{\theta}{2})\mathbf{1} + \sin^2(\frac{\theta}{2})\sigma_z^1\sigma_z^2 - i\sin(\theta)\frac{\sigma_x^1\sigma_x^2+\sigma_y^1\sigma_y^2}{2} \\
&=^L \cos(\theta)\mathbf{1} - i\sin(\theta)(\sigma_+^1\sigma_-^2 + \sigma_-^1\sigma_+^2) \qquad (4.16)
\end{aligned}
$$

$$
\begin{aligned}
e^{-i\theta\sigma_x^1\sigma_x^2} &= \cos(\theta) - i\sin(\theta)\sigma_x^1\sigma_x^2 \\
&= \cos(\theta)\mathbf{1} - i\sin(\theta)(\sigma_+^1\sigma_+^2 + \sigma_+^1\sigma_-^2 + \sigma_-^1\sigma_+^2 + \sigma_-^1\sigma_-^2) \\
&=^L \cos(\theta)\mathbf{1} - i\sin(\theta)(\sigma_+^1\sigma_-^2 + \sigma_-^1\sigma_+^2) \qquad (4.17)
\end{aligned}
$$

$$
\begin{aligned}
e^{-i\theta\sigma_y^1\sigma_y^2} &= \cos(\theta) - i\sin(\theta)\sigma_y^1\sigma_y^2 \\
&= \cos(\theta)\mathbf{1} - i\sin(\theta)(-\sigma_+^1\sigma_+^2 + \sigma_+^1\sigma_-^2 + \sigma_-^1\sigma_+^2 - \sigma_-^1\sigma_-^2) \\
&=^L \cos(\theta)\mathbf{1} - i\sin(\theta)(\sigma_+^1\sigma_-^2 + \sigma_-^1\sigma_+^2) \qquad (4.18)
\end{aligned}
$$

Here the last lines in (Eqs. 4.16, 4.17, 4.18) are all equivalent. The $=^L$ operation keeps only the terms that act within the logical subspace. Explicitly, the logical basis states are eigenstates of the $\sigma_z^1\sigma_z^2$ operator with eigenvalue -1 and are also eigenstates of the operator $\sigma_\pm^1\sigma_\mp^2$ with eigenvalues of 0. Using the following substitutions the net unitary of a Hadamard gate and a CNOT gate can be decomposed into four separate logical operations (up to a global, unobservable phase), each consisting of a $\frac{\pi}{2}$ rotation about a single bilinear term:

$$
U_{C_0NOT}U_H \Leftrightarrow e^{i\varphi}U_4U_3U_2U_1 \qquad (4.19)
$$

$$\begin{aligned} U_1 &= e^{-i\frac{\pi}{4}\sigma_y^1\sigma_y^2} & U_2 &= e^{-i\frac{\pi}{4}\sigma_y^3\sigma_y^4} \\ U_3 &= e^{-i\frac{\pi}{4}\sigma_z^2\sigma_z^3} & U_4 &= e^{-i\frac{\pi}{4}\sigma_x^3\sigma_y^4} \end{aligned} \tag{4.20}$$

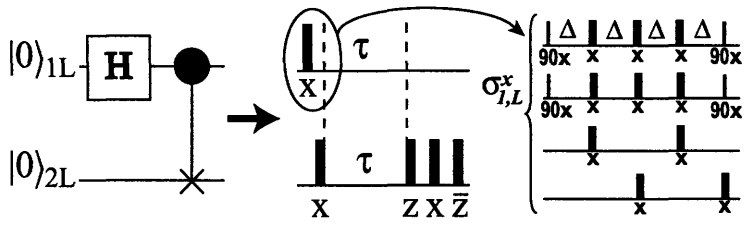

Figure 4-3: Logical Circuits to Physical Pulses. From left to right: entangling circuit on logical qubits and corresponding logical pulses and the pulse sequence implementing the σ_x^{1L} logical rotation on the physical qubits.

4.1.3 NMR Circuit

To generate a σ_x^{1L} coupling, we first generate the zeroth order average Hamiltonian $\mathcal{Z}_{12} = \frac{\pi}{2} J_{12}\sigma_z^1\sigma_z^2$ [56, 54] by employing the CP-like sequence (see Figure 4-3) alos described in Figure 3-4:

$$\Delta_{12} - \pi)_x^{1,2,3} - \Delta_{12} - \pi)_x^{1,2,4} - \Delta_{12} - \pi)_x^{1,2,3} - \Delta_{12} - \pi)_x^4 \tag{4.21}$$

(Note the notation $\theta)_\mu^k \equiv \exp[-i\frac{\theta}{2}\sum_k \sigma_\mu^k]$.) The effective unitary propagator to zeroth order is $U^{(0)} = e^{-4i\Delta_{12}\mathcal{Z}_{12}}$.

By applying "collective" $\frac{\pi}{2}$ rotations about $\hat{x}$ before the above sequence and a $\frac{\pi}{2}$ rotation about $-\hat{x}$ after, the average Hamiltonian is transformed into $\sigma_y^1\sigma_y^2$ which has the same action as a σ_x^{1L}. Similarly, if the rotation axes are separated by $\frac{\pi}{2}$ (i.e. an $\hat{y}$ phased pulse on one of the spins in the logical pair and a $\hat{x}$ phased pulse on the other), an operator isomorphic to a σ_y^{1L} is achieved. The logical "two-body" interaction – $\sigma_z^{1L}\sigma_z^{2L}$ – acting on the encoded subspaces is isomorphic to $\sigma_z^1\sigma_z^3$. We obtain this by using (4.21) and replacing spin 2 with spin 3. Each of the four rotations in (4.20) can

be generated in this manner yielding an overall sequence:

$$\frac{\pi}{2}\Big)_{\bar{x}}^{1,2} - \mathsf{Z}_{12} - \frac{\pi}{2}\Big)_{x}^{1,2,3,4} - \mathsf{Z}_{34} - \frac{\pi}{2}\Big)_{\bar{x}}^{3,4} - \mathsf{Z}_{23} - \frac{\pi}{2}\Big)_{x}^{3}\frac{\pi}{2}\Big)_{y}^{4} - \mathsf{Z}_{34} - \frac{\pi}{2}\Big)_{\bar{x}}^{3}\frac{\pi}{2}\Big)_{\bar{y}}^{4} \quad (4.22)$$

where Z_{jk} denotes the subsequence generating $\mathcal{Z}_{jk}$ and setting $\Delta_{jk} = (8J_{jk})^{-1}$.

4.2 Experiment

Our quantum system is comprised of the four ^{13}C spins ($I = \frac{1}{2}$) of isotopically labeled crotonic acid (also known as trans-3-butenoic acid) [74]. This molecule contains nine magnetically active nuclei in total; the total spin system Hamiltonian takes the form:

$$\mathscr{H}_{internal} = \frac{1}{2}\sum_{i\in \mathrm{C}}(\omega_i - \omega_0^C)\sigma_z^i + \frac{1}{2}\sum_{k\in \mathrm{H}}(\omega_k - \omega_0^H)\sigma_z^i + \sum_{i,j\in \mathrm{C}; i<j}\frac{\pi}{2}J_{ij}\vec{\sigma}^i\cdot\vec{\sigma}^j + \sum_{k,l\in \mathrm{H}; k<l}\frac{\pi}{2}J_{kl}\vec{\sigma}^k\cdot\vec{\sigma}^l + \sum_{j,k; j<k}\frac{\pi}{2}J_{jk}\sigma_z^j\sigma_z^k \quad (4.23)$$

where ω_0^{C} (ω_0^{H}) is the rotating frame frequency near the ^{13}C (^{1}H) Larmor frequency, the ω_i are the chemical shifts of the 4 carbon nuclear spins, the ω_k are the chemical shifts of the 5 hydrogen nuclear spins, and the 6 J_{ij} (10 J_{kl}) are the scalar coupling constants between two carbon (two hydrogen) spins (as usual, $\hbar = 1$). We are mainly concerned with coherently controlling the carbon subsystem of spins and seek to suppress the proton subsystem. As the heteronuclear scalar couplings (terms $J_{j,k}$) are the only means of mixing the two subsystems, a broadband decoupling sequence modulating the proton spin system effectively removes this coupling during the experiment. In practice, decoupling the proton spin system is equivalent to saturating the populations of the proton spins. One potential artifact of this approach is the introduction of transient nuclear Overhauser effects (NOE) [108, 24, 135].

We apply the pulses, delays, and gradients outlined above to create two different initial states and two logical Bell states on the crotonic acid carbon subsystem. In order to quantify the result of our quantum operations, we reconstruct the initial and final states using quantum state tomography [28]. Here, we measure the Free

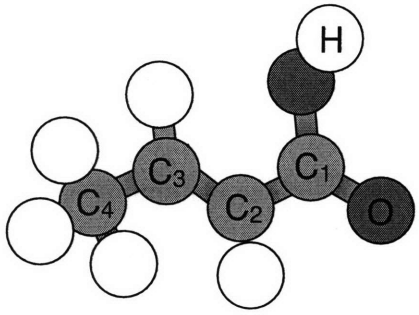

Figure 4-4: Crotonic Acid Molecule.

	C_1	C_2	C_3	C_4
C_1	6878.89	72.36	1.37	7.17
C_2		1882.63	69.58	1.65
C_3			4410.95	41.50
C_4				-8604.96

Table 4.1: Chemical Shift and Scalar Couplings of Crotonic Acid. The diagonal terms represent the chemical shifts of the four carbons relative to a transmitter frequency of 100. 622 439 610 MHz. The off-diagonal terms give the scalar couplings between the two spins. (Values courtesy of [74].)

Induction Decay of the spin system under $\mathscr{H}_{internal}$. The voltage signal is proportional to the expectation value $\left\langle \sum_j \sigma_-^j(t) \right\rangle$ from which we can determine the coefficients (c_n) of 32 of the 256 basis operators $(\hat{O}_n)$ comprising the $\mathbb{C}^{16} \times \mathbb{C}^{16}$ Hilbert space: $\rho = \sum_n c_n \hat{O}_n$. Applying a set of 18 readout pulses we can change unobservable $\hat{O}_n$ into one of the 32 directly observable operators and reconstruct the state using the orthogonality of these operators: $tr[\hat{O}_n \hat{O}_m^\dagger] = \delta_{mn}$.

$\frac{\pi}{2})_x^4$	$\frac{\pi}{2})_x^3$	$\frac{\pi}{2})_x^{23}$	$\frac{\pi}{2})_x^{1234}$	$\frac{\pi}{2})_y^{1234}$	$\frac{\pi}{2})_y^{12}$	$\frac{\pi}{2})_x^{13}$	$\frac{\pi}{2})_x^{24}$	$\frac{\pi}{2})_y^{123}$
$\frac{\pi}{2})_x^{124}$	$\frac{\pi}{2})_y^{134}$	$\frac{\pi}{2})_y^2 \frac{\pi}{2})_{\bar{x}}^4$	$\frac{\pi}{2})_y^{23} \frac{\pi}{2})_{\bar{x}}^1$	$\frac{\pi}{2})_y^{12} \frac{\pi}{2})_{\bar{x}}^3$	$\frac{\pi}{2})_x^{12} \frac{\pi}{2})_y^4$	$\frac{\pi}{2})_x^{13} \frac{\pi}{2})_y^4$	$\frac{\pi}{2})_y^{13} \frac{\pi}{2})_{\bar{x}}^4$	$\frac{\pi}{2})_x^{23} \frac{\pi}{2})_y^4$

Table 4.2: Readout Pulses. The notation $\theta)_\mu^j$ indicates a single spin rotation of angle θ about the Cartesian axis μ for each of the spins in $\{j\}$.

The reconstructed density matrices are shown in Figures 4-5 and 4-6, where the vertical axis shows the normalized amplitude and the horizontal axes label the basis states in the computational basis (i.e. $|0000\rangle$,$|0001\rangle$,...). The effects of decoherence

while performing the entangling operation can be qualitatively seen in the final state as an attenuation of the off-diagonal terms of the Bell state: $\frac{|01\rangle_L+|10\rangle_L}{\sqrt{2}}$. Such attenuation does not alter this state's protection against collective dephasing. Also, we note that this particular Bell State ($\frac{|01\rangle+|10\rangle}{\sqrt{2}}$) is immune to collective dephasing under the noise generator j_z^{12} but the Bell states $\frac{|00\rangle\pm|11\rangle}{\sqrt{2}}$ are not.

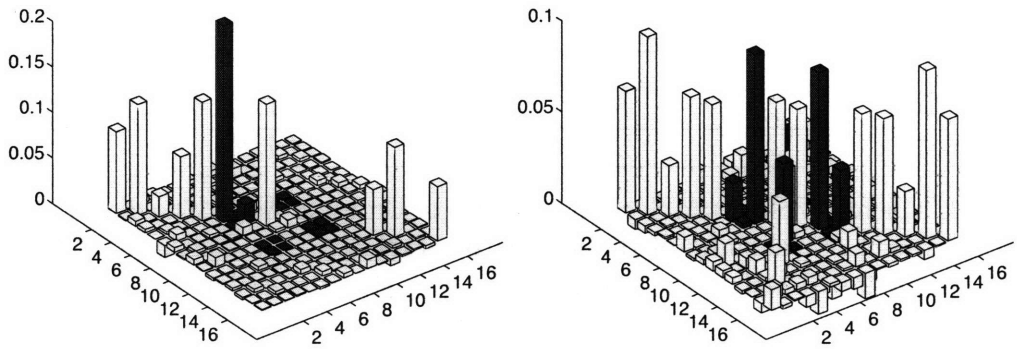

(a) Subsystem Pseudo-Pure State

(b) Logical Bell State

Figure 4-5: Subsystem pseudo-pure and logical bell state density matrices. Density matrices for the initial pseudo-pure state over only the logical subspace (a) and the corresponding Bell-State (b). The darker part indicates the states in the logical subspace. In the case of the subsystem pseudo-pure states, the division of the logical subspace allows for the other areas of Hilbert space to be mixed.

4.3 Analysis

With the numerical values for the density operators we can now quantitatively assess the implementation of the logical operations over the entire Hilbert space and the logical subspace. We can also quantify the decoherence due to leakage.

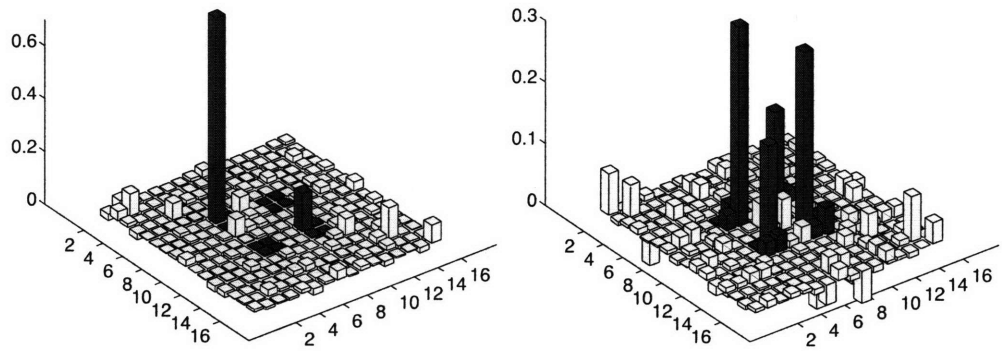

(a) Pseudo-Pure (b) Logical Bell State

Figure 4-6: Pseudo-pure and logical bell state density matrices. Density matrices for the initial pseudo-pure state over the entire Hilbert space (a) and the corresponding logical Bell State (b). The basis states comprising the dual DFS have been darkened.

4.3.1 Measures of Control

The quantum process associated with the encoded entangling operation can be specified by the general map:

$$\mathcal{E}(\rho) = \sum_{\mu} A_{\mu} \rho A_{\mu}^{\dagger} \tag{4.24}$$

where A_μ are Kraus operators describing the experimental implementation of the encoded operation, and ρ is defined over the entire Hilbert space. If the process consists of strictly coherent dynamics a single Kraus operator defines the operation: $A_0 = U$. The correlation of two quantum states is defined as [43]:

$$C = \frac{Tr\{\rho_{th}\rho_{exp}\}}{\sqrt{Tr\{\rho_{th}^2\}Tr\{\rho_{exp}^2\}}} \tag{4.25}$$

which defines the relative closeness of states in Hilbert space with proper normalization. Here $\rho_{th} = U\rho_{in}U^{\dagger}$, $\rho_{exp} = \mathcal{E}(\rho_{in})$, and ρ_{in} define the ideal, experimental and input states respectively. The closeness of the ideal state to the experimental state measures how well we have implemented the logical entangling operation for a particular input state.

When the quantum process $\mathcal{E}$ includes incoherent and decoherent dynamics, the purity ($Tr\{\rho^2\}$) of the experimental state ρ_{exp} is less than that of the initial state ρ_{in}. In this case, one can define an attenuated correlation $C' = \gamma C$ where the attenuation coefficient is defined as

$$\gamma = \sqrt{\frac{Tr\{\rho_{exp}^2\}}{Tr\{\rho_{in}^2\}}} \tag{4.26}$$

When we compare theoretical and experimental encoded states, their overlap has contributions that mirror the logical subsystem structure of the Hilbert space. Consider for simplicity a Hilbert space that can be written in terms of a logical and non-logical subspaces, $\mathcal{H} \cong \mathcal{L} \oplus \mathcal{R}$. The Kraus operators [78] A_μ can be separated into three groups: $\{A_{\mu,\mathsf{LL}}, A_{\mu,\mathsf{RR}}, A_{\mu,\mathsf{LR}}\}$, which respectively describe the maps on the $\mathcal{L}$ subspace, $\mathcal{R}$ subspace, and the mixing of these two subspaces. The correlation will reflect these three contributions to the dynamics, $C = \alpha_{\mathsf{LL}} C_{\mathsf{LL}} + (\alpha_{\mathsf{LR}} C_{\mathsf{LR}} + \alpha_{\mathsf{RL}} C_{\mathsf{RL}}) + \alpha_{\mathsf{RR}} C_{\mathsf{RR}}$, where:

$$C_{\mathsf{KH}} = \frac{Tr\{P_{\mathsf{K}} \rho_{th} \sum_\mu A_{\mu,\mathsf{KH}} (P_{\mathsf{H}} \rho_{in} P_{\mathsf{H}}) A_{\mu,\mathsf{KH}}^\dagger\}}{\sqrt{Tr\{(P_{\mathsf{H}} \rho_{exp})^2\} Tr\{(P_{\mathsf{K}} \rho_{th})^2\}}}, \qquad \alpha_{\mathsf{KH}} = \sqrt{\frac{Tr\{(P_{\mathsf{H}} \rho_{exp})^2\} Tr\{(P_{\mathsf{K}} \rho_{th})^2\}}{Tr\{\rho_{exp}^2\} Tr\{\rho_{th}^2\}}} \tag{4.27}$$

Here we define P_{L} (P_{R}) as the projector onto the encoded (non-logical) subspace. Notice that if the ideal state is inside the logical subspace, its projection on the non-logical subspace $P_{\mathsf{R}} \rho_{th}$ is zero and the last term goes to zero, $C_{\mathsf{RR}} = 0$.

For encoded qubits, we limit state tomography to the logical subspace only, so that a reduced number of readouts is enough to characterize the information available from the this subspace. The ability to preserve and manipulate the information inside the logical subspace can be better quantified by the correlation on this subspace, C_{LL}, comparing the experimental logical state with the theoretical state inside the subspace only. If the input state of this process, ρ_{in}, is a full pseudo-pure state (FPPS) and inside the logical subspace, the correlation C_{LL} with the logical ideal state is the only contribution to the total correlation C.

If a subsystem pseudo-pure state (SPPS) is used instead, $C_{\mathsf{LR}} \neq 0$, since the

output state in the protected subspace may contain contributions arising from the action of the map $\mathcal{E}$ on the identity in the non-logical subspace. Given an input state $\rho_{in} = a|\psi\rangle\langle\psi|_L + (1-a)\frac{\mathbf{1}_R}{d_R}$, from the experimental output state we can only measure the quantity (by observing only the l-logical qubits or their phyisical equivalents):

$$C^*_{\mathsf{LL}} = aC_{\mathsf{LL}} + (1-a)C_{\mathsf{LR}} = aC_{\mathsf{LL}} + (1-a)\frac{Tr\{U_{th}|\psi\rangle\langle\psi|_L U^\dagger_{th}\mathcal{E}(\frac{\mathbf{1}_R}{d_R})\}}{\sqrt{Tr\{(P_L\rho_{exp}P_L)^2\}}\sqrt{Tr\{(P_L\rho_{th}P_L)^2\}}} \tag{4.28}$$

Note that in this case $C \neq C^*_{\mathsf{LL}}$, since the contribution C_{RL} is not taken into account. The measured correlation is thus defined by two terms: the first takes into account the control over the encoded subspace only and the eventual leakage from it, while the second takes into account mixing from the $\mathcal{R}$ subspace to the $\mathcal{L}$ subspace. State tomography of the input state $\mathbf{1}_R$ after the algorithm allows one to calculate the correlation on the logical subspace C_{LL}.

To characterize the control of quantum gate operations most generally, many metrics have been suggested [43, 128, 104]. A good operational metric is for example the average gate fidelity (or fidelity of entanglement), that can be measured as the average of correlations of a complete orthonormal set of input states $\{\rho^j\}$: $\bar{F} = \sum_j C^j = \sum_j Tr\{U_{th}\rho^j U_{th}\mathcal{E}(\rho^j)\}$. Similarly, the encoded operational fidelity can be defined as the average correlation over an orthonormal set of operators spanning $\mathcal{L}$ (ρ^j_L): $\bar{F}_L = \sum'_j C^j_{LL} = \sum'_j Tr\{U_{th}\rho^j_L U_{th}\mathcal{E}(\rho^j_L)\}$.

The fidelity on the logical subspace focuses on the achieved control in the implementation of the desired transformation on the protected subspace; this new metric is immune to unitary or decoherent errors within $\mathcal{R}$ alone:

$$\begin{aligned}\bar{F}_L &= \textstyle\sum'_j C^j_{LL} = \sum'_j Tr\{U_{th}\rho^j_L U_{th}(\sum_\mu A_\mu P_L \rho^j_L P_L A_\mu)\} \\ &= \textstyle\sum_\mu |U_{th}A_{\mu,L}|^2/N^2\end{aligned} \tag{4.29}$$

The extent to which $U_{L,exp}$ is close to $U_{th,L}$ can be determined from $\bar{F}_L$, while the avoidance of subspace mixing will be specified by the gap between $\bar{F}$ to $\bar{F}_L$.

Quantum state	C_{Sim}	C_{Exp}	C_{LL}
Full pseudo-pure (FPPS)	0.98	0.91	0.99
Full pseudo-pure Bell state (FPPBS)	0.96	0.74	0.95
Subsystem pseudo-pure (SPPS)	0.99	0.97	0.99
Subsystem pseudo-pure Bell state (SPPBS)	0.97	0.87	0.91

Table 4.3: Experimental and simulated data for the encoded Bell state. Experimental errors of $\approx 4\%$ can be attributed to systematic errors in the fitting algorithm used to reconstruct the density matrix from NMR spectral data. C_{Sim} represents the correlation between simulation of the NMR spin system and the ideal state, taken over the entire Hilbert space. C_{Exp} compares this same simulation of the experiment to the experimental tomography reconstruction of the state, in the entire Hilbert space. C_{LL} measures the correlation between the simulated and experimental states projected onto the logical subspace.

Quantum state	γ_{Sim}	γ_{Exp}	γ_{LL}
Full pseudo-pure Bell State (FPPBS)	0.97	0.78	0.65
Subsystem pseudo-pure Bell State (SPPBS)	0.95	0.87	0.72

Table 4.4: Attenuation coefficients for encoded Bell states. These values represent a loss of purity in implementing a sequence of gates for entangling logical qubits. γ_{Sim} shows the attenuation of the ideal encoded Bell state of an NMR simulation including coherent and incoherent processes only, normalized to the initial state purity. γ_{Exp} shows the loss of purity between the experimental initial state and final states, reconstructed using state tomography. γ_{LL} shows the loss of purity for the projection of these experimentally reconstructed states onto the logical subspace. Values less than unity indicate a loss of coherence in the spin system.

4.3.2 Analysis of the Experiment

Since the experimental implementation of the pulse sequence used to generate logical entanglement is independent of the initial state, we can use both initial states and the aforementioned measures to gauge our control of the logical subspace. When these measures differ with different initial states we reveal several key features of the experimental implementation not accounted for in the simulation.

With respect to a simulation of the NMR system over four spins, the sequence generates the desired logical entanglement with high fidelity regardless of initial state. For example, in comparing the full pseudo-pure state (FPPS) and the subsystem pseudo-pure state (SPPS), we see that the correlation between the ideal state and

the simulated state (C_{Sim}) are nearly unity and differ from each other by only 1%. The resulting simulated correlations of the full and subsystem pseudo-pure Bell states, abbreviated FPPBS and SPPBS respectively, also differ by only 1% and are quite close to unity. Lastly, the attenuation coefficients differ by 2%. As the simulations do not take into account any decoherent or relaxation processes (T_1, T_2, Overhauser effects, etc.), any reduction in purity is due solely to the simulation of RF inhomogeneity, an incoherent process [13].

In comparing the experimentally measured density operator with the simulations we can quantify our ability to experimentally create the desired initial state, implement our entangling operation, and see the effects of decoherence on the system. First, we see that the correlation of the the SPPS is 6% higher than that of the FPPS when measured over the entire Hilbert space (C_{exp}) but equal and nearly unity when the states are projected onto the logical subspace (C_{LL}). This apparent discrepancy represents errors due to unwanted, nonzero contributions to the density operator *outside* the logical subspace since $C_{exp} = \sum_{\mathsf{jk}} \alpha_{\mathsf{jk}} C_{\mathsf{jk}}$ where C_{jk} represent correlations for blocks of the density operator and α is a weighting factor summing to unity ($\sum_{\mathsf{jk}} \alpha_{\mathsf{jk}} = 1$) [22]. To illustrate this aspect, we can calculate C_{RR}, α_{LL}, and α_{RR} for both initial states.

For the SPPS, $C_{\mathsf{RR}} = 0.97$, $\alpha_{\mathsf{LL}} = 0.38$, and $\alpha_{\mathsf{RR}} = 0.61$. Whereas for the FPPS, $C_{\mathsf{RR}} = 0.45$, $\alpha_{\mathsf{LL}} = 0.89$, and $\alpha_{\mathsf{RR}} = 0.05$. (For the ideal SPPS α_{LL} should be $\frac{4}{9}$ and α_{RR} should be $\frac{5}{9}$; for the ideal FPPS α_{LL} should be 1.) The C_{exp} value for the SPPS is much higher than that of the FPPS due to having near unit values for both C_{RR} and C_{LL} and $\alpha_{\mathsf{LR}} \approx 0$. Physically, this emphasizes the advantages of using a simpler initial state. For the FPPS we must create a total density operator with equal weightings of the many-spin correlations like $\sigma_z^1\sigma_z^2\sigma_z^3\sigma_z^4$ and all the combinations of $\sigma_z^1\sigma_z^2\sigma_z^3$ between four spins starting from the thermal state: $\sum_{j=1}^{4} \sigma_z^j$. In the SPPS only terms involving classical correlations between two spins (like $\sigma_z^1\sigma_z^3$) are necessary. The primary source of error in creating pseudo-pure states over the entire Hilbert space are these many-spin correlations of the initial state, thus accounting for the lower C_{RR} contribution to the FPPS.

Next, we address our ability to experimentally implement encoded quantum operations by analyzing the different correlations of the FPPBS and the SPPBS. Since we use *exactly the same* pulse sequence to transform the FPPS to the FPPBS as we do for transforming the SPPS to the SPPBS, we would naively suspect the trends for the initial states to follow for the logical Bell states. However, the correlation between the experiment and the simulation for the SPPBS is roughly 18% better than that of the FPPBS. The fact that the FPPS and the SPPS are different states within the entire Hilbert space accounts for this: contributions from C_{RR} improve C_{exp} for sub-system pseudo-pure states. By calculating the projected correlations and weighting factors, we see that C_{exp} for the SPPBS is bolstered by C_{RR}, as $C_{\mathsf{RR}} = 0.91$, $\alpha_{\mathsf{RR}} = 0.64$, and $\alpha_{\mathsf{LL}} = 0.31$. For the FPPBS, $C_{\mathsf{RR}} = 0.41$, $\alpha_{\mathsf{RR}} = 0.06$, and $\alpha_{\mathsf{LL}} = 0.74$; as with the full pseudo-pure initial state, small errors outside the logical subspace considerably decrease the correlation over the entire Hilbert space. Furthermore, the pulse sequence seems to favor the SPPS state, as the purity (γ_{Exp}) of the SPPBS is larger than the FPPBS. Again, this behavior indicates the presence of many-spin correlations in full pseudo-pure states, as these correlations can develop extended and fragile quantum coherences, decohering faster than a single spin or a single logical qubit.

Finally, If we consider the evolution in the logical subspace only, we find that C_{LL} is quite high for both the FPPBS and the SPPBS: 0.95 compared to 0.91 respectively. Though slightly different from the simulations, the two states are comparable as the correlation within the logical subspace between the experimentally measured FPPBS and the experimentally measured SPPBS is 0.97. This indicates that our control sequence will transform information within the logical subspace in a nearly identical manner, unbiased towards the information outside the logical subspace. In summary, we see that for a given implementation of the logical entangling operation, we can learn about the experimental imperfections by preparing two states that are both pure within a given subspace but each different outside of this subspace. In particular, when considering the loss of purity and the correlation with the logical subspace, a subsystem pseudo-pure state outperforms a full pseudo-pure state when comparing the measured initial and final states to simulations.

4.4 Conclusions

The structure of the control and natural Hamiltonian plays an important role in the control of logical qubits, as the operators needed to implement gates may not be present and generating them may drive the information out of the subsystem. For large systems with significant symmetry (like quantum dots under the exchange interaction [37]) or exceedingly small systems [44], the structure of the natural Hamiltonian can provide the logical operations in itself. However, for systems of intermediate size (most relevant to the present implementations of quantum information processors) implementing quantum gates among logical qubits requires both a precise knowledge of the natural Hamiltonian and a complete set of control parameters to ensure no leakage from the protected subsystem or subspace. For example, if our four-qubit system were composed of two proton spins and two carbon spins, each individual species could be modulated separately, thus doubling the number of control parameters in the external Hamiltonian and limiting the leakage of the information from the subspace.

Recall that logical encodings are used to protect quantum information against decoherence. Here we have omitted the encoding and decoding step of getting the information from physical qubits to logical qubits and back and instead used an initial state already reflecting the encoding. Our measures of fidelity may seem artificial, as we could have actually measured the decoded qubits to get the same information about leakage, loss of purity, etc. We should stress that the *main* goal is to assess the control of logical qubits. Our measures over the logical degrees of freedom thus allow us to quantify the leakage and loss due to decoherence, as well as the correlations of the state. We can thus address the two main issues of logical control (i) implementing leakage-free gates and (ii) implementing the intended operator on the subspace without worrying about errors in the decoding process.

Lastly, our selection of logical qubits comprised of only two physical qubits limits our logical operations for single qubit and two-qubit interactions to only "two-body" operators. If instead we were to attempt a repetition of the experiment where the

logical qubits were encoded under different subsystems [45, 6], the single qubit and two-qubit rotations would involve either "three-body" operators [140] or a sum of non-commuting operators – quite unlikely to be found in a natural Hamiltonian. In such a scenario, the ability to implement logical operations would necessarily need to come from a modulation sequence, appropriately chosen to avoid leakage from the subsystem.

Chapter 5

Control of Anisotropically coupled Electron and Nuclear Spins in Closed Quantum Systems

5.1 Introduction

As introduced in Chapter 1, nuclear spin degrees of freedom are excellent candidates for quantum bits due to their long decoherence times. Although liquid phase NMR systems are well recognized as versatile test-beds for quantum information processing [30, 49], there is not a comprehensive proposal for how to engineer these coherent systems into a robust quantum information processor that could scale as a quantum computer [148, 126, 15]. The recognized deficiencies of liquid phase NMR include: (i) the spin system is in a highly mixed state, (ii) the measurement is a weak ensemble based measurement, (iii) the product of coupling strengths (J) to coherence times (T_2) is not much larger than 1, and (iv) the addressability of single qubits does not scale with Hilbert space size.

Nuclear spins in single crystals or solid-state lattices have more promise for QIP. For example the product $J \cdot T_2$ is larger due to dipole-dipole coupling of nuclear spins and the longer relaxation times achieved by cooling to ^{4}He temperatures. The

polarization is also increased by going to lower temperatures, but still will not be in a pure state without using another mechanism for increasing the polarization, like optical pumping or dynamic nuclear polarization [134]. There have not been convincing and demonstrable ways of achieving projective measurements of nuclear spins or addressing the number of spins required for a quantum computation.

With the incorporation of electron spins into the lattice of nuclear spins, it is possible to make strong projective measurements [123, 77] for both initializing a single electron spin qubit or reading out the nuclear spin state. These measurements can also boost the polarization of the nuclear spins. Furthermore, the orbital and charge degrees of freedom of an electron spin can be used to incorporate "flying qubits", linking together two information processors. The hyperfine interactions of the electron and nuclear spins are also much stronger, but the coherence times of the electron may also be much shorter, limiting the $J \cdot T_2$ product. It should be stressed that this system may not scale to be a quantum computer, but does provide comprehensive solutions to state initialization and projective measurements.

Many solid-state spin based proposals [68, 90, 11, 82, 29, 137] are particularly suitable for quantum computaton. First, the advances in semiconductor manufacturing technology can be used for a "top-down" approach to building coherent devices with scalable controls as the Hilbert space grows in size. For example, photolithography techniques can be used to make a single qubit device. Such devices can be coupled together 'on-chip' with each device having its own controls and tunable qubit-qubit couplings. Likewise, select natural materials provide coherent, large Hilbert spaces in a "bottom-up" approach, like nuclear spins in a lattice, but with a limited number of controls. In both cases, the spin degrees of freedom provide Hilbert spaces with long coherence times. Errant spins outside the isolated system (either electron or nuclear in nature) act as a primary source of decoherence of the quantum information.

To date, there have been many demonstrations of coherent control in spin based solid-state qubit paradigms. As the effective volume of the electron wavefunction can vary by several orders of magnitude between specific systems, the electron spins and the nuclear spins can play roles as both an uncontrollable environment or as

controllable qubits. At one end of the spectrum, many groups have exhibited control over a confined electron qubit in GaAs quantum dots. Here, the surrounding substrate of magnetic nuclei typically act as a noisy environment, decohering the coherent electron spin state [110, 107, 72]. In systems where the electron spin is localized in a molecular orbital or color center, the electron spin interacts most strongly with a few nearest nuclei. Here, both the electron and the nuclear spins can be used as qubits for information processing. Recent demonstrations include controlled electron-nuclear entanglement [96, 97], enhanced nuclear spin detection [95, 26], and single electron-nuclear gates [65, 103]. At the opposite end of the spectrum, the electron spin can be considered an environment for a local cluster of nuclear spins. Optical pumping techniques can be used to effectively cool the temperature of the spin states, but the electron spin environment decoheres the nuclear spins during a computation [29]. Most recently, universal control of a nuclear spin via only electron spin control has been demonstrated, [39]. A summary of these works appears in Table 5.1.

Electron-Nuclear spins	Characteristic Systems	Improvements with AHF control	References
qubit-environment	Quantum Dots. Carbon Nanotubes.	Control spin diffusion. Extend electron T_2	[110, 107, 72]
qubit-memory	NV Centers. Fullerenes.	Extend coherence times to nuclear T_2.	[39, 65, 103]
qubit-qubit	Ionic single crystals.	Faster Gates. Universal Control	[96]
actuator-qubit	Molecular single crystals.	Faster Gates. Universal Control. Nuclear-nuclear gates via electron spin.	[95]
environment-qubit		Improved nuclear polarization transfer.	[29]

Table 5.1: Electron and Nuclear spin roles in coherent solid-state systems. Depending on the localization of the electronwave function and relative decoherence rates, an electron spin can act as a qubit or as an environment to nuclear spins. Coherence, in either case, can be extended by controlling the electron spin. If the hyperfine interaction is anisotropic, nuclear spin dynamics can be controlled via the electron spin. Such nuclear spin control may be used to reduce losses to the nuclear environment or to enhance polarization transfer nearby nuclear spins. It can also be used to robustly control small clusters of nuclear spins acting as small quantum information processors.

Ultimately the details of the microscopic electron wavefunction and the magnetic properties of the atomic lattice sites determine these systems' dynamics, thus the fate of any system as an information processor is determined by how the available control fields can steer the natural dynamics to a desired outcome. The presence of

an anisotropic hyperfine interaction provides a means by which the control of nuclear spins can be improved. Here we show how to exploit a local, isolated electron spin to coherently control nuclear spins. Moreover, we suggest that this approach provides a fast and reliable means of controlling nuclear spins and enables the electron spins of such solid-state systems to be used for state preparation and readout [95] of nuclear spin states, and *additionally* as a spin actuator for mediating nuclear-nuclear spin gates.

5.2 System Model

Many of the successes of liquid state NMR are due to the model of the spin system being an accurate and complete description of the coherent dynamics of the spin degrees of freedom. Likewise, we will choose solid-state electron-nuclear systems where a single localized electron interacts with a few nuclear spins at nearby lattice sites. In doing this, we neglect many uncontrollable degrees of freedom, such as phonon modes, electron orbital angular momentum, the lattice potential, and we can therefore write down a Hamiltonian for the spin degrees of freedom. Any coupling of these external degrees of freedom into the spins of the system will be treated as a source of decoherence.

Our Hamiltonian of a single local electron spin with angular momentum, $S = \frac{1}{2}$ and N nuclear spins, each with angular momentum $I_k = \frac{1}{2}$, in the presence of a magnetic field $\vec{B}$ is [130]:

$$\mathscr{H}_{\text{en}} = \beta_e \mathbf{g}_{\mu\nu} \hat{S}_\mu B_\nu - \sum_{k=1}^{N} \gamma_n^k (1 - \boldsymbol{\delta}_{\mu\nu}^k) \hat{I}_\mu^k B_\nu + 2\pi \sum_{k=1}^{N} \mathbf{A}_{\mu\nu}^k \hat{S}_\mu \hat{I}_\nu^k + \pi \sum_{k,l=1}^{N} \mathbf{D}_{\mu\nu}^{kl} \hat{I}_\mu^k \hat{I}_\nu^l \quad (5.1)$$

Here β_e is the Bohr magneton, γ_n^k is the gyromagnetic ratio of the k^{th} nuclear spin, and B_ν is the external magnetic field. $\hat{S}$ and $\hat{I}^k$ are the spin-$\frac{1}{2}$ operators. The second-rank tensors $\mathbf{g}$, $\mathbf{A}^k$, $\boldsymbol{\delta}^k$, and $\mathbf{D}^{kl}$ represent the electron g-factor, the hyperfine interaction, the chemical shift, and the nuclear dipole-dipole interaction respectively.

With the intention of controlling the electron spins via electron spin resonance

(ESR) techniques, we choose a magnetic field where the electron spin is quantized along the direction of $\vec{B} = B_0\hat{z}$. For a $g = 2$ electron, the magnetic moment of the electron spin is at least 660 times that of the nuclear spin. Thus, the nuclear spins will align (or anti-align) with the local fields present due to the hyperfine interaction, nuclear Zeeman interaction and the nuclear dipole-dipole interaction. In the regime where the nuclear Zeeman and hyperfine fields are comparable in magnitude [1] $\mathscr{H}_{\text{en}}$ can be approximated by[2]:

$$\mathscr{H}_{\text{en}} \approx \omega_S \hat{S}_z - \sum_{k=1}^{N} \omega_I^k \hat{I}_z^k + 2\pi \sum_{k=1}^{N} \left(A_{zx}^k \hat{S}_z \hat{I}_x^k + A_{zy}^k \hat{S}_z \hat{I}_y^k + A_{zz}^k \hat{S}_z \hat{I}_z^k \right) \tag{5.2}$$

Here, $\omega_s = \beta_e B_0 \|\mathbf{g}\|$ is the electron Larmor frequency and $\omega_I^k = \gamma_n \|(1-\boldsymbol{\delta})\| B_0$ is the nuclear Larmor frequency. The nuclear dipole-dipole interaction is neglected as it is typically 100 times weaker than the hyperfine terms.

To find the eigenfunctions of this system, we can apply a similarity transformation to diagonalize $\mathscr{H}_{\text{en}}$. Because the nuclear dipole-dipole interaction is not relevant in this approximation, the only spin-spin interactions involve the electron spin and a single nuclear spin. Thus, the transformation has a particularly simple form[84, 130]:

$$T \;=\; \hat{S}^{\alpha} \otimes_k R(\theta_{\uparrow}^k, \phi_{\uparrow}^k) \bigoplus \hat{S}^{\beta} \otimes_k R(\theta_{\downarrow}^k, \phi_{\downarrow}^k) \tag{5.3}$$

where $R(\theta^k, \phi^k) = e^{-i\theta^k I_y^k} e^{-i\phi^k I_z^k}$, $\hat{S}^{\alpha} = |\uparrow\rangle\langle\uparrow| = E_+$, $\hat{S}^{\beta} = |\downarrow\rangle\langle\downarrow| = E_-$. The Hilbert space divides into an upper and lower manifold for the electron spin. In each manifold, the hyperfine field has a particular orientation with respect to the main magnetic field, giving a geometric description (Fig. 5-1). The rotation about $\hat{z}$ moves the A_{zy} and A_{zx} components to the zx-plane for each nuclear spin; the rotation about $\hat{y}$ rotates the zx vector along z thus diagonalizing the Hamiltonian. The nuclear spin eigenstates

[1] The relative order of terms for Eq. (5.2) to hold is: $\beta_e \|g_{\mu z}\| B_0 \gg \|\gamma_n (1-\boldsymbol{\delta}) B_0\| \sim \|A_{z\nu}\| \gg \|D^{j,k}\|$

[2] $\hat{I}_\mu = \frac{1}{2}\sigma_\mu$ are the spin operators in relation to the Pauli matrices.

are thus a mixture of the nuclear Zeeman eigenstates:

$$|\alpha_0^k\rangle = \cos\theta_\uparrow^k|\uparrow\rangle + e^{i\varphi_\uparrow^k}\sin\theta_\uparrow|\downarrow\rangle \tag{5.4}$$

$$|\alpha_1^k\rangle = \sin\theta_\uparrow^k|\uparrow\rangle - e^{i\varphi_\uparrow^k}\cos\theta_\uparrow|\downarrow\rangle \tag{5.5}$$

$$|\beta_0^k\rangle = \cos\theta_\downarrow^k|\uparrow\rangle + e^{i\varphi_\downarrow^k}\sin\theta_\downarrow|\downarrow\rangle \tag{5.6}$$

$$|\beta_1^k\rangle = \sin\theta_\downarrow^k|\uparrow\rangle - e^{i\varphi_\downarrow^k}\cos\theta_\downarrow|\downarrow\rangle \tag{5.7}$$

$$\tag{5.8}$$

It should be noted that $\langle\alpha_{0,1}^k|\beta_{0,1}\rangle \neq 0$ provided $\theta_\uparrow^k \neq 2\pi l + \theta_\downarrow^k$. The eigenfunctions of this $\mathbb{C}^{2^{N+1}} \times \mathbb{C}^{2^{N+1}}$ Hilbert space can store N bits of quantum information in either the spin-up or spin-down electron manifolds:

$$|j_1\, j_2\, \ldots j_N\rangle = |\uparrow\rangle \otimes |\alpha_{j_1}^1\rangle \otimes |\alpha_{j_2}^2\rangle \otimes \cdots \otimes |\alpha_{j_N}^N\rangle \tag{5.9}$$

$$\text{or} \tag{5.10}$$

$$= |\downarrow\rangle \otimes |\beta_{j_1}^1\rangle \otimes |\beta_{j_2}^2\rangle \otimes \cdots \otimes |\beta_{j_N}^N\rangle \tag{5.11}$$

where $j_k \in \{0, 1\}$. Note that by storing information in either the $|\uparrow\rangle$ or $|\downarrow\rangle$ electron spin manifolds there is no spin superposition of the electron wavefunction and that the electron spin remains separable from the nuclear spins. This precludes the electron spin from storing any quantum information.

5.3 Generating Universal Control

Having identified a physical system in which we can store quantum, we now identify the requisite control fields for universality. Drawing from the spectroscopy of electron and nuclear systems, one possible way of controlling the spin system is to use oscillatory magnetic fields resonant with a sufficient number of transitions to ensure universality. This will include both electron spin transitions and nuclear spin transitions, much like the ENDOR (electron-nuclear double resonance) spectroscopic technique [32, 101]. Another possible method is to draw from the ESEEM [122](electron spin

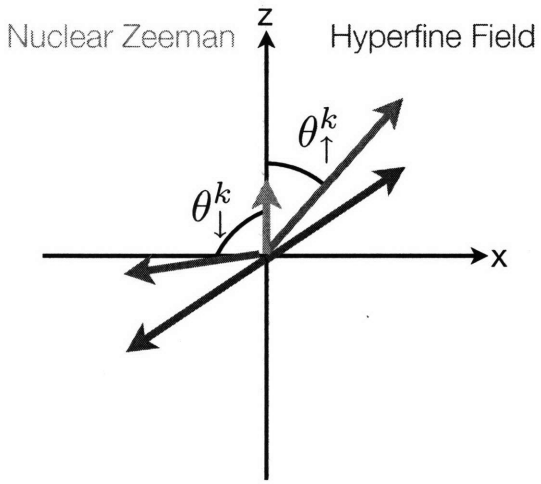

Figure 5-1: Magnetic fields present at a single nuclear spin. The vector sum the DC magnetic field (lighter arrow along z) and the hyperfine field (darker arrows) define the nuclear spin quantization axis. The angle between the electron quantization axis (z) and the nuclear quantization axis depends on the state of the electron: $\theta_\uparrow$ or $\theta_\downarrow$. In the absence of hyperfine anisotropy, the nuclear quantization axes are anti-parallel. Note that we work only in the $x-z$ plane, despite the fact that we have specified both A_{zx} and A_{zy} terms. The $x-y$ vector can be rotated to purely the x axis with a new $A'_{zx} = \sqrt{A^2_{zx} + A^2_{zy}}$.

echo envelope modulation). Here, pulses only on the electron spin excite coherence between a number of levels. This coherence is then modulated by the different nuclear spins through the hyperfine interaction. Coherence can be transferred from the electron to the nuclear spin also [62, 112]. The origin of the echo modulations of ESEEM are due precisely to the orthogonality of the two quantization axes of the nuclear spin arising from the anisotropy of the hyperfine interaction. This same condition allows us to completely control the 1e-Nn system without the need for explicit nuclear spin transitions.

If we seek to address only electron spin transitions, our controls are time-dependent microwave fields oscillating near the electron spin resonance frequency and parametrized by three values: B_1^e, the amplitude of an oscillating magnetic field ($\perp B_0\hat{z}$), Ω the frequency of oscillation, and ϕ the phase of the oscillation:

$$\begin{aligned} &\mathscr{H}_{\mathrm{C}}(B_1^e, \Omega, \phi) = \\ &\beta_e \|\mathbf{g}\| B_1^e(t) \Big(\cos\left(\Omega t + \phi(t)\right)\ \hat{S}_x\ + \sin\left(\Omega t + \phi(t)\right)\ \hat{S}_y \Big) \end{aligned} \tag{5.12}$$

For simplicity, we can set $\phi(t) = \phi_0 = \frac{\pi}{2}$ and remove phase control completely. The control Hamiltonian will excite transitions between levels $|j\rangle$ and $|k\rangle$ provided the matrix element $\langle k|\hat{S}_x|j\rangle \neq 0$. If we assume the condition $\langle \alpha_{0,1}^k | \beta_{0,1} \rangle \neq 0$, this operator will induce transitions between any level in the electron spin $\downarrow$ manifold and all levels in the electron spin $\uparrow$ manifold, barring degenerate eigenvalues E_j of $\mathscr{H}_{\mathrm{en}}$ or degenerate transition frequencies ($\hbar\omega_{jk} = E_j - E_k$)[3]. As shown in [141, 4], this level connectivity can be represented as a graph, and that the complete connectivity of the graph generated by the matrix elements of $\mathscr{H}_{\mathrm{C}}$ guarantee universality. For the 1e-N nuclear spin system, distinct g-factors and hyperfine couplings for each nuclear spin guarantee the non-degeneracy of the eigenstates. The hyperfine couplings and the nuclear Zeeman frequencies must also be chosen such that $\omega_{jk}/\omega_{j'k'} \neq 1$. Lastly, the anisotropy of *each* hyperfine interaction assures the complete connectivity of the graph given the form of $\mathscr{H}_{\mathrm{en}}$ and $\mathscr{H}_{\mathrm{C}}$. The entire system can be completely controlled by modulating B_1^e for a fixed Ω and without phase control. Figure 5-2

[3]The matrix representation of $\mathscr{H}_{\mathrm{en}}$ in this case is *strongly regular*

shows several diagrammatic examples. For universal control over a set of nuclear spins with resolved anisotropic hyperfine coupling to one electron spin it is sufficient to apply an amplitude modulated waveform to any electron spin transition.

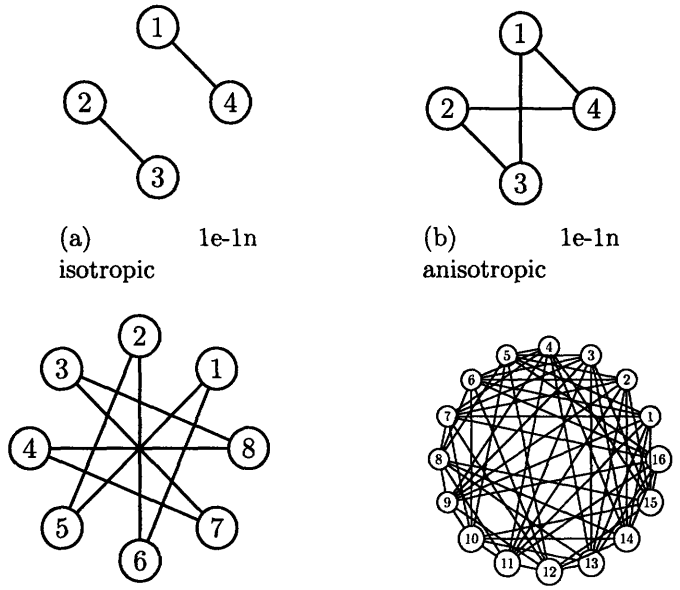

Figure 5-2: Diagrammatic proof of universality. The connectivity of energy levels of 1e-Nn systems represented as 2^{N+1} node graphs. An edge is drawn between two nodes if the control Hamiltonian operator has a non-zero matrix element for the eigenstates represented by the nodes ($\langle k|\hat{S}_x|j\rangle \neq 0$). When the hyperfine interaction between *any one* nuclear spin and the electron is purely isotropic universality is not achieved as in (a) and (c). In the limit of infinitesimal anisotropy, the levels may be connected but the matrix elements are exceedingly small, indicating long times for generating universal control. As additional nuclear spins are added, the connectivity becomes exponentially more complex.

Physically, we can see the modulation of $\mathscr{H}_0$ via $\mathscr{H}_C$ as generating rotations about non-commuting axes. The local magnetic field vector between the electron spin and any one nuclear spins is separated by a finite angle, $\theta^k_{\uparrow,\downarrow}$ depending on the spin state of the electron. $\mathscr{H}_C$ modulates these non-commuting vectors and can thus generate any rotation in SU(4) of a pair. If we consider collective motions of the N nuclear spins relative to the two electron spin states, this generates the complete algebra in SU(2^{N+1}). Given the complexity of the full dynamics of these 2^N vectors, we can use

optimal control methods (Chapter 2) developed for and applied to liquid and solid state NMR [71, 43, 115, 8] to engineer arbitrary unitaries.

5.4 Implementation

Further understanding of the requirements for control can be seen by analyzing an example system. We demonstrate the utility of this control scheme by exploring Ramsey fringes [119] and Hahn echoes [57] in a 1e-1n system. Our 1e-1n system is a single crystal of x-ray irradiated malonic acid — an extremely well-studied sample in the field of pulsed ESR. Using previously reported [92, 91, 69] hyperfine constants of malonic acid we can orient the crystal to maximize the anisotropy of the hyperfine interaction.

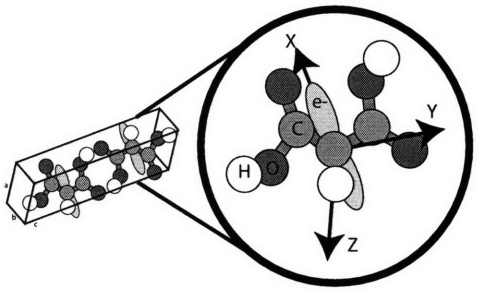

Figure 5-3: Malonic Acid Crystal. Molecules of malonic acid align via hydrogen bonding to form a single triclinic crystal. There are either two or four molecules per unit cell depending on temperature. White spheres represent hydrogen atoms, gray spheres are carbon atoms, and red spheres are oxygen atoms. The electron defect is located on the middle (carbonyl) carbon.

In the hyperfine principal axis system (PAS) the couplings of $\mathbf{A}^{\mathrm{PAS}}$ are $\approx [-60, -30, -90]$. The PAS of the hyperfine tensor, the molecular axes (x,y,z) and the crystal axes (a,b,c) are nearly coincident in this molecule. By mounting the crystal along the the $\hat{c}$ axis, a natural direction for crystal growth, we ensure the -90MHz component is always perpendicular to $B_0\hat{z}$. We can then rotate the crystal about the $\hat{c}$ axis, changing the relative angle between the $\hat{a} - \hat{c}$ plane and the magnetic field. We measure the splitting of the two hyperfine peaks versus rotation angle using x-band continuous-wave (CW) ESR measurements (Figure 5-4). When the $\hat{a} - \hat{c}$ plane is 45° to the $\hat{z}$

laboratory direction, the A_{zx} term is maximized. This orientation is then transferred to our pulsed ESR spectrometer.

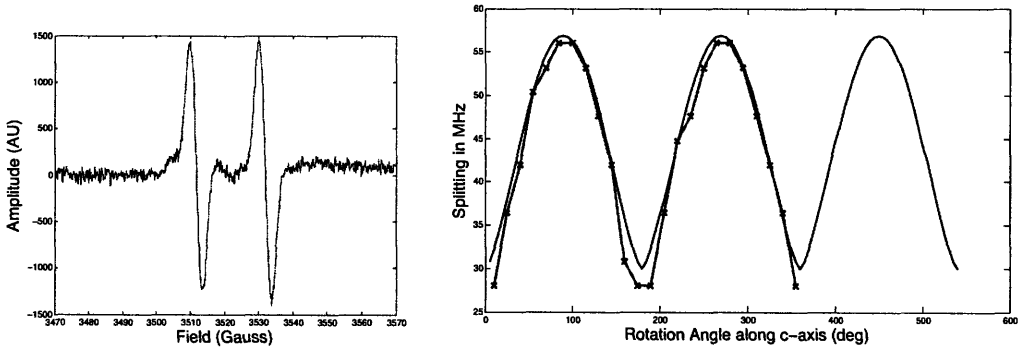

(a) CW ESR spectrum

(b) Fitting of splitting to the model

Figure 5-4: CW ESR alignment of crystal. The CW ESR spectrum (a) shows two dispersive peaks, one for each possible nuclear spin configuration. By changing the orientation of the crystal with respect to the magnetic field, the energy difference in the splittings changes. We can map the measured splittings with our model Hamiltonian to maximize A_{zx}

In adopting a real system to our model, we note that the electron wave function of our paramagnetic defect can couple to the many surrounding hydrogen (I=1/2) nuclei as the dipole-dipole part of the hyperfine interaction between the S=1/2 electron and the hydrogen nuclei in the matrix maintains over a long-range [130]. Furthermore, we assume that each individual paramagnetic center does not couple to any other paramagnetic center. In reality, these many centers can lead to line broadening via instantaneous diffusion mechanisms. These undesired couplings can be treated as a source of decoherence. Thus, the simplified Hamiltonian of our closed 1e-1n system is: $\mathscr{H}_0/2\pi = \nu_s\hat{S}_z - \nu_n\hat{I}_z + A_{zx}\hat{S}_z\hat{I}_x + A_{zz}\hat{S}_z\hat{I}_z$ where $\nu_s = 11.885$ GHz, $\nu_n = 18.1$ MHz, $A_{zx} \approx 14.2$ MHz, and $A_{zz} \approx -42.7$ MHz. The control Hamiltonian Eq. (5.12) parameters are $\max\big(\beta_e\|\mathbf{g}\|B_1^e(t)\big)/2\pi = 7$ MHz and $\Omega/2\pi = 11.909$ GHz. A description of the experimental setup appears in Chapter 7.

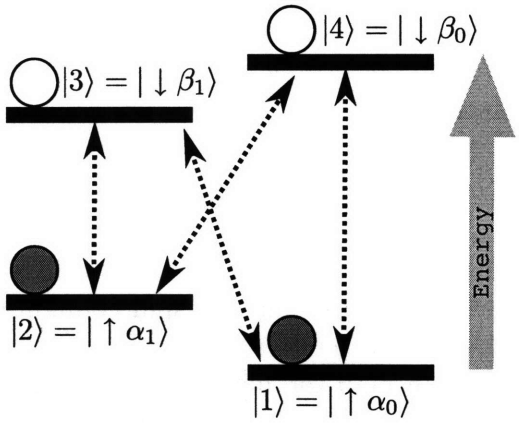

Figure 5-5: Energy level diagram of a one electron (S=1/2) and one nuclear (I=1/2) spin system for Eq. (5.2). The electron spin state is in an eigenstate of purely the Zeeman interaction, while the nuclear spin state is *not* an eigenfunction of the Zeeman interaction alone due to the anisotropic hyperfine interaction. Because $\langle\alpha_0|\beta_1\rangle \neq 0$ and $\langle\alpha_0|\beta_0\rangle \neq 0$ the electron spin operator ($\hat{S}_x$) has finite probabilities between all levels (dashed arrows). This allows for universal control of the entire spin system. The filled and unfilled circles represent the relative spin state populations of the ensemble at thermal equilibrium. In our experimental setup the energy differences are $\omega_{12}/2\pi = 7.8$ MHz, $\omega_{34}/2\pi = 40$ MHz, $\omega_{14}/2\pi = 12.005$ GHz, $\omega_{23}/2\pi = 11.954$ GHz

5.4.1 ESEEM and Effective ESEEM

For an ESEEM experiment, one does a spin echo experiment on the electron spin:

$$\frac{\pi}{2}\Big)_x^S - \tau - \pi\Big)_x^S - \tau \tag{5.13}$$

In the absence of any hyperfine coupling, we would expect to see an echo at a time 2τ after the first pulse, such that $\langle S_y(2\tau)\rangle = -1$. If we have a Hamiltonian like Eq. (5.2), then the echo is modulated as [130]:

$$\langle S_y(2\tau)\rangle = -1 + \frac{k}{4}\Big(2 - 2\cos(|\omega_{12}|\tau) - 2\cos(|\omega_{34}|\tau) + 2\cos(\omega_+\tau) + 2\cos(\omega_-\tau)\Big) \tag{5.14}$$

where $\omega_\pm = \omega_{12} \pm \omega_{34}$ and $k = (2\pi\omega_I A_{zx}/\omega_{12}\omega_{34})^2$ is the modulation depth. This results assumes that $\|\mathscr{H}_C\| \gg \|\mathscr{H}_{\text{en}}\|$, such that the electron pulses excite the entire spectrum of available transitions. In the case when one has a weak microwave excitation field $\|\mathscr{H}_C\| < \|\mathscr{H}_{\text{en}}\|$, only the transitions near the resonance frequency Ω are excited. Various methods, such as soft ESEEM [129] have been developed for overcoming this problem by applying radiation at two different carrier frequencies simultaneously.

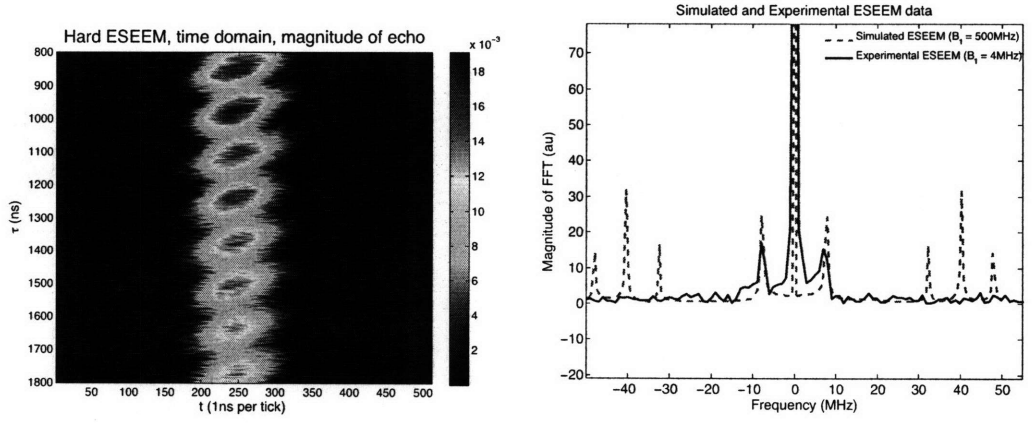

(a) 2D $\tau - t$ plot

(b) FFT of τ (projected)

Figure 5-6: ESEEM data using hard pulses. Note the absence of peaks above 8 MHz. The linewidths of the simulated data reflect a 6G magnetic field inhomogeneity. The experimental and simulated data have not been normalized.

Due to the insufficient RF power for covering the breadth of the malonic acid spectrum, we can use our knowledge of the natural Hamiltonian at our preferred orientation to generate the propagator: $U_{\pi/2} = e^{-i\pi S_x/2}$ using GRAPE. We then apply the sequence:

$$U_{\pi/2} - \tau - U_{\pi/2} - \tau \tag{5.15}$$

and expect to see echo modulations like those in Eq. (5.14) but reduced by a factor of two because of the second flip angle.

Figure 5-7 shows the two-dimensional data for this "effective ESEEM" experiment. If we take the Fourier transform over the indirect (τ) domain and sum up over the acquistion signal, we get a projection onto the indirect Fourier domain with spectral components near 8,40,48 and 32 MHz. This indicates that we have components of the electron magnetization modulating at the two nuclear frequencies.

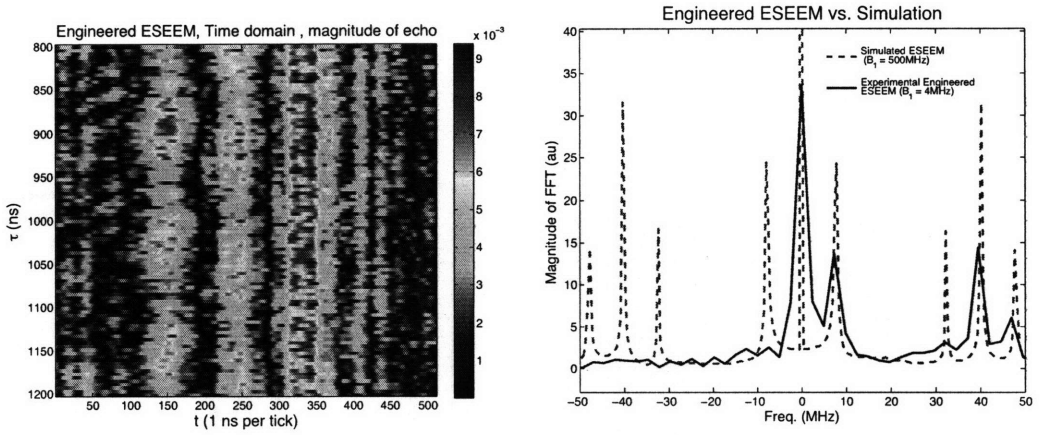

(a) 2D $\tau - t$ plot

(b) FFT of τ (projected)

Figure 5-7: ESEEM data using engineering pulses. Note the presence of all four peaks in the experimental spectrum. The 8 MHz and 40 MHz peaks should be nearly twice the amplitude of the sum and difference peaks. The simulated data and experimental data are not normalized. Peaks occur on the positive frequency domain only due to phase cycling of the pulses.

5.4.2 Ramsey-fringe Experiments

We can now use our methods to isolate one of the frequencies of the ESEEM experiment. The equilibrium state of the ensemble system, $\rho_{\text{thermal}} = -\hat{S}_z$, has no net nuclear spin polarization, so we first transfer the available electron spin polarization to the nuclear spins. This is achieved by selectively inverting the levels $|2\rangle$ and $|4\rangle$ or $|1\rangle$ and $|3\rangle$ (see Figure 5-5). We created coherence between nuclear eigenstates with an engineered nuclear $\pi/2$ pulse selective for only one of the electron manifolds[4], $U_{12}(\pi/2)$. The Ramsey fringe experiment measures the phase evolution under $\mathscr{H}_{en}$. We halt evolution by again applying $U_{12}(\pi/2)$ and then transferring the polarization back to the electron spin. By monitoring the relative amplitude of the electron spin echo at different times, τ, we indirectly observe the nuclear spin dynamics. If we introduce a refocusing pulse for both nuclear spin states, $U_r = U_{12}(\pi) + U_{34}(\pi)$, after a time $\tau/2$, the coherent phase oscillations are refocused.

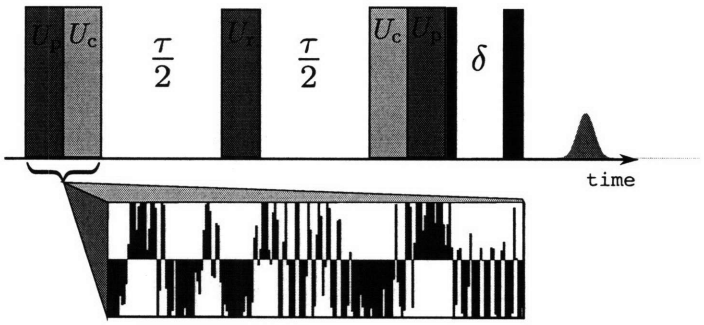

Figure 5-8: Schematic pulse sequence for measuring 'Ramsey fringes and Hahn echoes. U_{p} creates a non-equilibirum population difference between levels 1&2 and U_{c} creates a coherence between nuclear spin in the S=-1/2 manifold. During τ, this coherence evolves under $\mathscr{H}_{en}$, acquiring an observable phase. The coherence is transformed back to a population difference between nuclear spin levels and then to electron spin levels. A pair of short, unmodulated pulses are used to detect an electron spin echo whose height is proportional to the resultant electron spin population. With a refocusing pulse (U_{r}) the acquired phase is unraveled, leaving no modulation of the echo signal. The waveform used to implement $U_{\text{p}}U_{\text{c}}$ is shown inset. Note that all pulses are applied resonant with the 1-4 transition and induces transitions between 1-4, 2-4, 1-3, and 2-3 due to selection rules.

[4] $U_{jk}(\theta) = e^{(-i\frac{\theta}{2}\sigma_x^{jk})}$. The operator $\sigma_x^{jk} = |j\rangle\langle k| + |k\rangle\langle j|$

Figure 5-9 shows the coherent oscillations between nuclear coherence on levels $|1\rangle$ & $|2\rangle$. We implement the net unitaries, $U_{\rm pc} = U_{12}(\frac{\pi}{2})U_{24}(\pi)$ and $U_{\rm pc}^{-1}$ as a single modulation sequence with total time (T) of 800ns and simulated fidelities (F) 0.99 and 0.98 respectively. The nuclear π pulse, U_r, was implemented in a time period (F=0.98, T=520ns) much shorter than would have been possible by addressing the nuclear spin transitions directly. Again, it is key to realize that the nuclear pulse is achieved through modulation of the hyperfine interaction and is applied at the electron spin resonance frequency. Simulations of the modulation sequences using our model 1e-1n Hamiltonian show agreement of the observed oscillation.

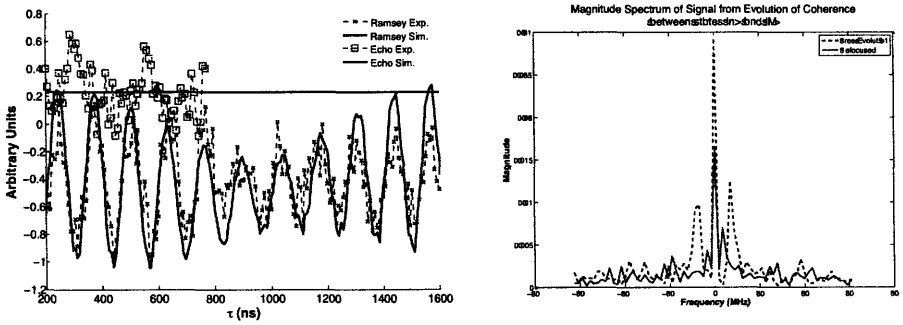

Figure 5-9: Coherent oscillations of the nuclear spin in malonic acid. Measurements of the electron spin echo as a function of τ (a) between coherence transfer indirectly reveal the nuclear precession rate. Simulations of the experiment show agreement between with the observed signal (signal-to-noise ratio $\approx$ 4.9). The Ramsey fringe experiment ($\times$) reveals a clear precession of the coherence between the $|1\rangle$ and $|2\rangle$ states at roughly 8 MHz . For the echo data ($\Box$), small pulse errors and incomplete phase cycling result in a small systematic oscillation at half the precession frequency; ideally the echo should be independent of τ. The FFT (b) without a nuclear π reveals the rate of procession as roughly 8 MHz . The absence of spectral peaks at $\pm$8MHz indicates successful refocusing in the presence of a "nuclear π pulse".

5.5 Nuclear-Nuclear Gates

A key point to storing quantum information in electron nuclear spin systems is the speed-up in quantum gate times due to the strength of the hyperfine interaction compared to the nuclear-nuclear dipole interaction. Since no information resides on

the electron spin, this *electron spin actuator* provides a handle with which to control the nuclear spins. Any two qubit nuclear gate U_{n_1,n_2} must be implemented on the entire electron-nuclear system as $U_{\text{en}} = \mathbf{1} \otimes U_{n_1,n_2}$. The electron spin may be put into a superposition, or even entangled with the nuclear spins, during the gate, but at the end of the gate remains separable from the nuclear subsystem.

To motivate the potential of this scheme, we can take the malonic acid system above and replace the carbon nucleus closest to the paramagnetic electron with an isotopically labeled ^{13}C spin. The PAS of the hyperfine tensor between the carbon and the electron is nearly the same as the proton-electron with values $\mathbf{A}_{\text{PAS}}^{k=2} = [213, 42, 13]$. Using the orientation the maximizes the coupling from above, we find a modulation sequence for a CNOT, condition on the proton spin: $U_{\text{1e-2n}} = \mathbf{1} \otimes \text{C}_H\text{NOT}_C$. This modulation (Figure 5-10) uses both phase and amplitude modulation of the microwave field. It also assumes twice the maximum amplitude and twice the bandwidth of the pulses used in the Ramsey Fringe experiments. These conditions are well within the bounds of current ESR technology. Were such a gate needed in the absence of an electron spin, the necessary time would be at least ten times that of our modulation sequence ($2\mu s$) based on the C-H dipolar coupling strength[5].

5.6 Conclusions

The universality of a system comprised of one electron spin ($S = 1/2$) with resolved anisotropic hyperfine couplings to N nuclear spins ($I_k = 1/2$) has been investigated. This system can be completely controlled by only irradiating transitions involving an electron spin flip. Due to the spin state of the electron there are two nuclear quantization axes with orthogonal components; any quantum gate between the nuclear spins can be composed of repeated rotations of the orthogonal components induced by electron spin flips. In practice, optimal control techniques must be employed to find an implementable modulation of the control fields. We have used these modulation

[5]The dipolar coupling strength for the -CH pair is +10 to -20 kHz depending on orientation to the magnetic field.

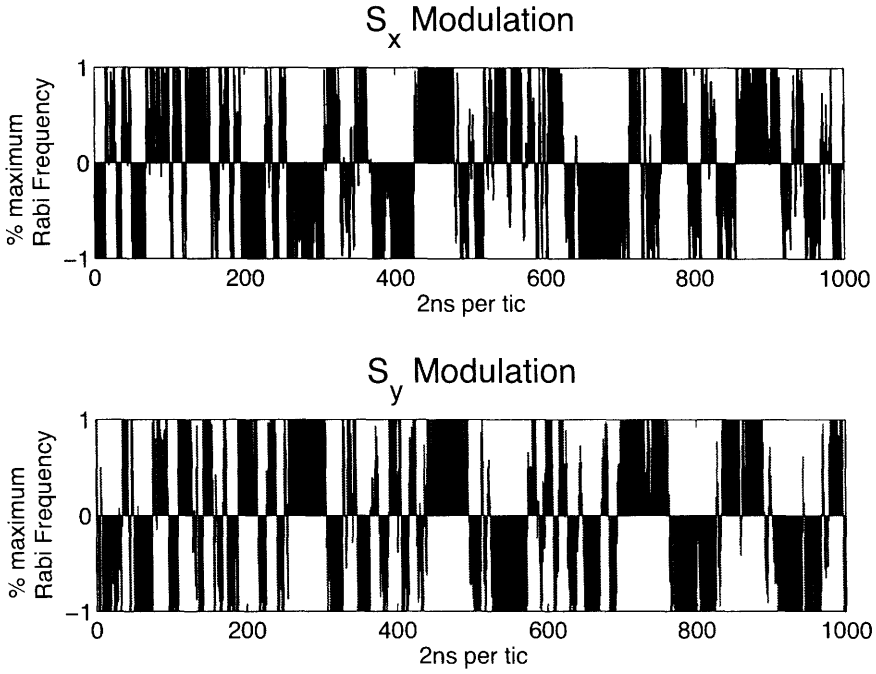

Figure 5-10: Nuclear-Nuclear CNOT Modulation for ^{13}C-labeled irradiated malonic acid. At the same crystal orientation used above, we find a sequence modulating both the amplitude and the phase of the control Hamiltonian with 1000 2ns intervals and a maximum Rabi frequency of 15MHz. The time for performing the gate using nuclear-nuclear dipole couplings (tens of kHz) in the absence of an electron spin would be much longer.

sequences to explicitly demonstrate universality in a malonic acid (N=1) ensemble spin system.

Such systems with resolved anisotropic hyperfine interactions form a small quantum information processors which can be the basis of a larger quantum computer; however, an efficient means of coupling these small processors together is a necessary step towards building a quantum computer.

Chapter 6

Decoherence protection of electron-nuclear systems

In a closed quantum system, consisting of one electron (S=1/2) and one nuclear spin (I=1/2) coupled together, relaxation and decoherence of either spin species can in turn affect the coherence properties of the other.

For solid-state spin systems, a bath of nuclear spin flip-flops generates a stochastically fluctuating magnetic field, leading to decoherence of electron spin states [138, 34]. As the nuclear spins present in these systems lies in the mesoscopic to macroscopic scales, most theories rely on mean-field approximations, cluster expansions [124], or other methods for approximating the magnetic field arising from an unnumerable collection of nuclear spins.

In the microscopic limit, the dynamics of a closed system can be solved completely, with clearly interpretable results for a small number of spins. The simplest of these consists of one electron (S=1/2) and one nuclear spin (I=1/2) coupled together. Relaxation and decoherence of either spin species can in turn affect the coherence properties of the other by way of the spin-spin coupling. Empirically, nuclear spin relaxation times are measured to be much longer than those of electron spins; this can be attributed to the stronger extent of localization of the nuclear spin wavefunction compared to the total electron wavefunction and the strength of the Bohr and nuclear magnetons. In a coupled system however, the relaxation times are

not necessarily uncorrelated. Here, I present a simple model for showing the nuclear T_2^n time is limited by the electron T_1^e.

6.1 Markovian Dynamics of the T_1 process

.

The characteristic signature of a T_1 process is the return of a system to equilibrium of a state out of equilibrium. For a spin-1/2 quantized along the $\hat{z}$-axis in the laboratory frame, fluctuating fields resonant with the energy difference between the two spin states[1] and perpendicular to $\hat{z}$ are the main mechanism for T_1 [134]. A dephasing, or T_2 process, occurs when these fluctuations parallel to the axis of quantization. Following the calculation from Redfield theory, the operational form of the T_1 process involves an emission (σ_-) and an absorption process (σ_+) while that of a T_2 process have a (σ_z) contribution. These operators appear with a time-dependence in the Redfield matrix $\mathscr{R}$ and evolve under the equation of motion:

$$\frac{d\rho_{ij}}{dt} = \mathscr{H}_{ik}\rho_{kj} - \rho_{ik}\mathscr{H}_{kj} + \mathscr{R}_{ikjl}(\rho_{kl}) \tag{6.1}$$

(The subscripts represent row and column indices; repeated letters indicate a summation.)

In the limit where the correlation time, τ_c, of the environment changing its state (the effects of which appear in $\mathscr{R}$), approaches 0, the environment behaves as a memoryless system. In this Markovian limit, the dynamics can be accurately described by a Lindblad master equation:

$$\frac{d\rho}{dt} = \frac{i}{\hbar}[\mathscr{H}, \rho] + \sum_k \{L_k\rho, L_k^\dagger\} + \{L_k^\dagger\rho, L_k\} \tag{6.2}$$

where L_k are the jump operators describing the effective action of the environment

[1]For single crystal solid-state systems, the mechanism for T_1^e is mostly the indirect, or Raman process. This involves two phonons with an energy difference of $E = \hbar(\nu_1 - \nu_2)$ and a virtual energy level. These processes give rise to a rapid divergence of T_1^e at at low temperatures, as $T_1^e \sim 1/T^9$ [130]

on the system in the short-time limit.

To solve this equation, ρ can be expressed as a linear combination of operators B_j that span the Hilbert space and are orthogonal under Hilbert-Schmidt inner product ($\mathrm{tr}(B_k^\dagger B_j) = \delta_{jk}$). This will yield N^2 coupled differential equations for a Hilbert space of size N.

The dynamics can be expressed compactly by choosing the N^2 matrices B_j to be the canonical rank 1 matrices E_{ij}, where the entry of the i^{th} row and j^{th} column is 1 and all other entries are 0. The density operator, ρ can then be columnized by stacking the N columns in order to generate an $N^2 \times 1$ vector $|\rho\rangle$. The $N \times N$ dimensional operators can be converted into their supermatrix $N^2 \times N^2$ versions using the following transformations.

$$\hat{\hat{\mathscr{H}}} = \mathscr{H}^* \otimes \mathbf{1} - \mathbf{1} \otimes \mathscr{H} \tag{6.3}$$

$$\hat{\hat{\Gamma}} = \sum_k L_k^* \otimes L_k + -\frac{1}{2}\mathbf{1} \otimes L_k^\dagger L_k - \frac{1}{2} L_k^T L_k^* \otimes \mathbf{1} \tag{6.4}$$

$\hat{\hat{\Gamma}}$ is known as the relaxation superoperator and represents the dissipative dynamics of the system. The Lindbladian $\mathscr{L} = i\hat{\hat{\mathscr{H}}}_0 + \hat{\hat{\Gamma}}$ is the generator of the dynamics and the dynamical superoperator $\mathcal{S}$ is obtained by integrating the dynamics (Chapter 3).

$$|\dot{\rho}(t)\rangle = \mathscr{L}|\rho(t)\rangle \tag{6.5}$$

6.1.1 Example: T_1^e dependence of T_2^n

Using the framework set forth in the preceeding section, we are poised to solve the problem of a coupled electron and nuclear spin system with the electron undergoing solely T_1^e relaxation. Take the closed system Hamiltonian to be $\mathscr{H}_0^{1e1n} = \omega_S \hat{S}_z + \omega_I \hat{I}_z + A\hat{S}_z\hat{I}_z$ and the jump operators to be $L_1 = \sqrt{g_+}\sigma_+$ and $L_2 = \sqrt{g_-}\sigma_-$. The 16 entries in $|\rho\rangle$ are ordered: $\{\rho_{11}, \rho_{21}, \ldots, \rho_{12}, \rho_{22}, \ldots, \rho_{44}\}$.

Conveniently, this matrix equation can be permuted to a block diagonal structure resulting in four sets of coupled differential equations:

$$\dot{\rho}_{11} = -g_-\rho_{11} + g_+\rho_{33} \tag{6.6}$$

$$\dot{\rho}_{33} = g_-\rho_{11} - g_+\rho_{33} \tag{6.7}$$

$$\dot{\rho}_{22} = -g_-\rho_{22} + g_+\rho_{44} \tag{6.8}$$

$$\dot{\rho}_{44} = g_-\rho_{22} - g_+\rho_{44} \tag{6.9}$$

$$\dot{\rho}_{21} = -\big(2i(A+\omega_i) + g_-\big)\rho_{21} + g_+\rho_{43} \tag{6.10}$$

$$\dot{\rho}_{43} = g_-\rho_{21} - \big(2i(-A+\omega_i) + g_+\big)\rho_{43} \tag{6.11}$$

$$\dot{\rho}_{12} = -\big(-2i(A+\omega_i) + g_-\big)\rho_{12} + g_+\rho_{34} \tag{6.12}$$

$$\dot{\rho}_{34} = g_+\rho_{12} - \big(2i(A-\omega_i) + g_+\big)\rho_{34} \tag{6.13}$$

The eight other matrix elements are uncoupled. Each pair of differential equations can be solved using eigenvalue and eigenvector methods associated with solving for the equation of motion of coupled oscillators. The diagonal terms (ρ_{11} & ρ_{22}, ρ_{33} & ρ_{44}) yield a simple solution by linear combination. By choosing $a_+ = \rho_{11,22} + \rho_{33,44}$ and $a_- = \rho_{11,33} - \frac{g_+}{g_-}\rho_{22,44}$ we reduce the equations of motion to:

$$\dot{a}_+ = 0 \tag{6.14}$$

$$\dot{a}_- = -(g_- + g_+)a_- \tag{6.15}$$

Thus the characteristic decay time for any of the diagonal terms of our coupled spin system undergoing T_1^e modes of decay is $T_1 = (g_- + g_+)^{-1}$.

For the "off-diagonal" terms, corresponding to nuclear spin coherence, the eigenvalues of the coupled equations are more complex and can be found by solving for the characteristic polynomial of the matrix:

$$\begin{bmatrix} -\Big(2i(\omega_i + A) + g_-\Big) & g_+ \\ g_- & -\Big(2i(\omega_i + A) + g_-\Big) \end{bmatrix}$$

yield the eigenvalues:

$$\lambda_{\pm} = -2i\omega_i - \frac{1}{2}(g_+ + g_-) \pm \frac{1}{2}\sqrt{(g_- + g_-)^2 + 8iA(g_- - g_+) - 16A^2}$$

While this general solution may not give much insight to the dynamics, we can make a few generalizations for limiting behavior. First, we see that if roots $\lambda_{\pm}$ are complex, meaning we will have coherent oscillations of the nuclear coherence as well as decay. The nuclear coherence decay rate, T_2^n will thus be bounded by the largest of the two roots. In the case when $A = 0$, then spin systems are uncoupled; as such the characteristic decay rate are $\lambda_{\pm} = \{-2i\omega_i, -2i\omega_i - (g_+ + g_-)\}$. Any state with nuclear coherence and the electron state in equilibrium will oscillate and not decay, whereas any non-equilibrium electron state with nuclear coherence will return to equilibrium at a rate of $1/T_1^e$. For $(g_+ + g_-) \gg A$ we get similar behavior although the physics is completely different. This motional narrowing regime can be understood as the nuclear coherence being modulated so quickly that dephasing becomes frozen. Lastly, in the slow motion regime ($(g_+ + g_-) \ll A$) $T_2^n \to 2T_1^e$.

If the interaction between the electron spin and the nuclear spin is made anisotropic as in Eq. (5.2) the 16×16 Liouvillian no longer has a compact block diagonal structure. Instead, the 16 differential equations becomes coupled and involve diagonalizing one 8×8 matrix and two 4×4 matrices. A closed form solution using the preceeding techniques will not prove effective.

Suppose that we do not want to know the general dynamics for any particular state of an electron-nuclear system undergoing T_1^e modes of decay, but instead pose the question: *Which states will not decay?* Such states will be eigenstates with pure imaginary eigenvalues, as seen from the $A \to 0$ case above. Thus by identifying the eigenstates of $\mathscr{L}$ with purely imaginary eigenvalues, we will find a set of states $\{|\eta\rangle\}$ that do not decay. If the dimension of this set is four or greater, then there may be a possibility of storing one qubit of information in the state, provided proper commutation relations for these states exist.

To understand the structure of the Lindbladian we first identify a few facts about

$\mathscr{L}$. In general $\mathscr{L}$ is a defective matrix, in that it is not uniquely diagonalizable. This can be seen from the fact that $\mathscr{L} - \mathscr{L}^\dagger \neq 0$ and resides in the non-Hermiticity of the relaxation superoperator $\hat{\hat{\Gamma}}$. Otherwise stated, $\mathscr{L}$ is not Hermitian. Quantum processes must conserve the complete positivity of the state ρ; as such $\mathscr{L}$ is a completely positive matrix and thus has a decomposition as $\mathscr{L} = GG^T$. This implies that $\mathscr{L}$ has a set of right eigenvectors following the equation:

$$\mathscr{L}|v_j\rangle = \lambda_j|v_j\rangle \tag{6.16}$$

and has a set of left eigenvectors following the equation:

$$\langle w_j|\mathscr{L} = \lambda_j\langle w_j| \tag{6.17}$$

The set of eigenvalues, $\{\lambda_j\}$ is the same from both $\{|w_j\rangle\}$ and $\{|v_j\rangle\}$. Thus $\{|w_j\rangle\}$ is the dual of $\{|v_j\rangle\}$.

For a time-indepedent Lindbladian, $\frac{\partial \mathscr{L}}{\partial t} = 0$, the solution for the state vector at any future time is given by:

$$|\rho(t)\rangle = \sum_k \langle w_k|\rho(0)\rangle e^{\lambda_k t}|v_k\rangle \tag{6.18}$$

This description of open system quantum evolution is reminiscent of a quantum channel described as a Kraus form. The state is mapped from an initial to a final form with a complex phase and attenuation. Let the left and right eigenvectors with purely imaginary or zero eigenvalue be $\{|\eta_j^L\rangle\}$ and $\{|\eta_j^R\rangle\}$ respectively. As a single qubit can be parametrized by three real values plus one normalization constraint, if the $\{|\eta_j^R\rangle\}$ follow the same commutation relations and product relations as the Pauli operators, then one qubit of information can be stored in the $\{|\eta_j^R\rangle\}$.

6.2 Encoding nuclear spins to electron T_1

As stated in the previous section, for the Ising Hamiltonian with $A \neq 0$ and $g_\pm$ comparable any other energy scale in the Hamiltonian, all states with nuclear coherence will decay. Numerically, we see this is the case for an anisotropic Hamiltonian with realistic energy scales. Using the insight of the collective σ_z encoding from Chapter 3, we can try to use an additional nuclear spin and the subsystem of two coupled nuclear states $|J=0, J_z=0\rangle$ and $|J=1, J_z=0\rangle$ to remove the effect of the nuclear spin dephasing due to the ZZ coupling. We take as our model Hamiltonian for this 1e-2n system to be:

$$\mathscr{H}_0^{1e1n} = \omega_S \hat{S}_z + \omega_{I1}\hat{I}_z^1 + 2\pi A_1 \hat{S}_z \hat{I}_z + \omega_{I2}\hat{I}_z^2 + 2\pi A_2 \hat{S}_z \hat{I}_z^2 \tag{6.19}$$

Numerical results show that when $A_1 = A_2$ and $\omega_{I1} = \omega_{I2}$ we have $|\eta_L\rangle = \{\mathbf{1} + \sigma_z^1 + \sigma_z^2 + \sigma_z^1\sigma_z^2, \mathbf{1} + \sigma_z^1 + \sigma_z^2 + \sigma_z^1\sigma_z^2, \mathbf{1} + \sigma_z^1 + \sigma_z^2 + \sigma_z^1\sigma_z^2, \mathbf{1} + \sigma_z^1 + \sigma_z^2 + \sigma_z^1\sigma_z^2, \sigma_x^1\sigma_x^2 + \sigma_y^2\sigma_y^2 \pm (\sigma_x^1\sigma_y^2 - \sigma_y^1\sigma_x^2)\}$. For any values $A_1 \neq A_2$ or $\omega_{I1} \neq \omega_{I2}$ only 4 pure imaginary eigenvalues of $\mathscr{L}$ exist, with the removal of the σ_x and σ_y terms from the preceding set. This is a direct analog of the collective Z DFS from Chapter 3. If the coupling constant or Zeeman frequencies are equal the internal Hamiltonian drives information stored in the protected states outside of the subspace.

For an anisotropic interaction of the form:

$$\mathscr{H}_0^{1e2n} = \omega_S \hat{S}_z + \omega_{I1}\hat{I}_z^1 + 2\pi A_1 \hat{S}_z \hat{I}_z + B_1 \hat{S}_z \hat{I}_x^1 + \omega_{I2}\hat{I}_z^2 + 2\pi A_2 \hat{S}_z \hat{I}_z^2 + B_2 \hat{S}_z \hat{I}_x^2 \tag{6.20}$$

numerical results show that no such DFS exists even when the couplings are equal. As the quantization axis of the nuclear spins depends on the state of the electron spin, electron spin flips in the isotropic Hamiltonian are seen as fluctuating fields along the $\hat{z}$-axis. In the anisotropic case the axis for the nuclear spins when the electron spin is up differs from when it is down, thus an electron spin flip looks like a rotation about the y-axis for the nuclear spins and evolution under $\mathscr{H}_0^{1e2n}$ after the spin flip looks like a z-axis rotation. Random rotations about two orthogonal

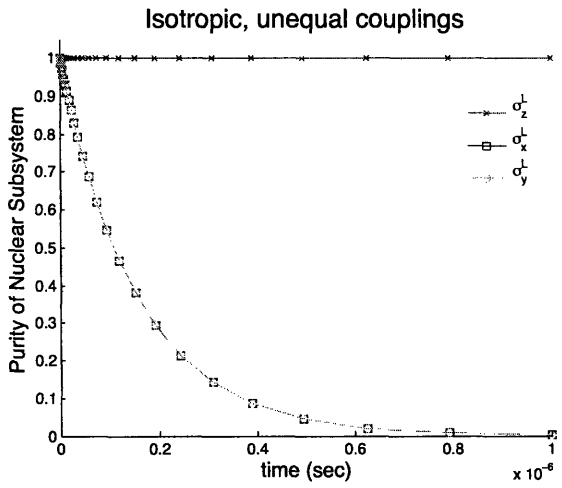

Figure 6-1: Purity of 1e-2n DFS Qubit. For unequal couplings, we see the same behavior as we showed for the NMR example. σ_x^L and σ_y^L undergo a single exponential dephase, while the σ_z^L state remains unchanged. For equal couplings (not shown), none of the logical states decay.

axes thus lead to dephasing, as our logical qubit is only immune to random rotations about a single axis. In the isotropic case the electron T_1^e process can be modeled as a dephasing channel for the nuclear spins. For the anisotropic case, the channel then looks depolarizing.

For collective rotations about a random axis, it has been shown [146, 45, 145] that the smallest noiseless subsystem supporting one qubit of information exists for three spin-1/2 particles within doubly degenerate subsystems of $J = 1/2$. Our numerical calculations of the eigenspaces of $\mathscr{L}$, after a Gram-Schmidt decomposition, show that when the couplings are equal ($A_j = A$, $B_j = B$, $\omega_{Ij} = \omega_I$), a total of five states have zero eigenvalues with eigenvectors $|\eta_j^L\rangle$ and $|\eta_j^R\rangle$. This numerical result cannot be compactly represented as sums of two-spin exchange operators, as the noiseless basis states.

Intuition suggests that the noiseless operators should remain invariant under the action $\mathscr{L}$ and also under the map generated by $\mathscr{L}$: $\mathbf{S} = e^{\mathscr{L}t}\ \forall t$. Again, we use numerical calculations to investigate the dynamics. For any state $|\sigma_z^e \otimes \sigma_\mu^L\rangle$ the outcome of the map $\mathbf{S}$ is 1. These states are fixed points of the map, as suspected. If the electron

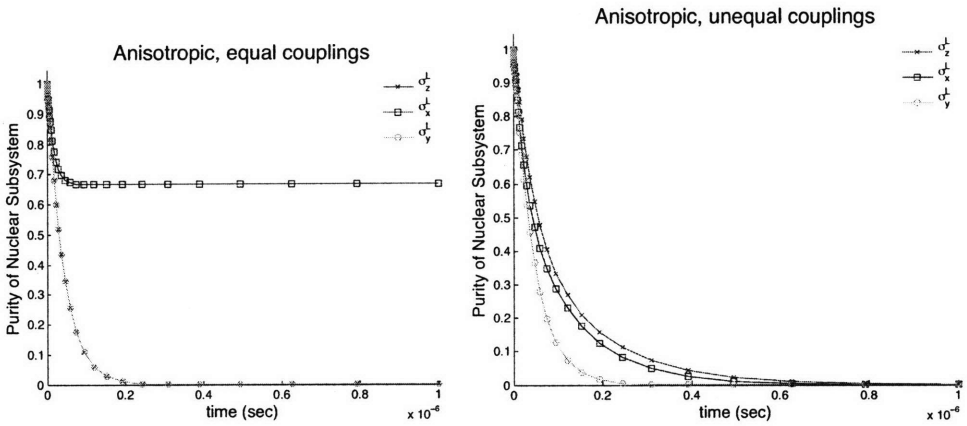

(a) Anisotropic, $A_1 = A_2$, $B_1 = B_2$, $\omega_{I1} = \omega_{I2}$ (b) Anisotropic, $A_1 \neq A_2$, $B_1 \neq B_2$, $\omega_{I1} = \omega_{I2}$

Figure 6-2: Purity of 1e-2n DFS Qubit. For equal couplings (a), the σ_z and σ_y following single exponential decays to zero. The state σ_x^L saturates a 2/3 because the fixed point of this map is $|\eta^L\rangle = \mathbf{1} - \frac{\vec{\sigma}_1 \cdot \vec{\sigma}_2}{3}$. For unequal couplings, all of the logical states decay to zero, as is characteristic of a depolarizing channel.

spin state has an identity component, then $\mathbf{S}|\mathbf{1}^e \otimes \sigma_\mu^L\rangle = \alpha|\mathbf{1}^e \otimes \sigma_\mu^L\rangle + \beta|\sigma_z^e \otimes \sigma_\mu^L\rangle$.

The non-unitality of the process manifests itself as the left eigenvectors are not in one-to-one correspondence with the right eigenvectors. One would suspect depolarizing/repolarizing of the state as $tr\{\rho(t=0)^2\} \neq tr\{\rho(t \to \infty)^2\}$. However, if we trace out the electron spin, we see that the information within the nuclear subsystem is preserved. Thus the initial state of the electron spin does not have to be the thermal state, but should be diagonal. This means that a single qubit of information within the three nuclear spins can be preserved.

The usual catalogue of logical encodings can thus be employed to nuclear spin subsystems coupled to a single electron spin to extend the memory of nuclear spin registers beyond the T_1^e of the electron spin. However, if the hyperfine couplings and Larmor frequencies of the nuclear spins composing the logical qubit are incompatible with the encoding, the natural Hamiltonian will drive the state outside the protected space.

Lastly, we have conveniently dropped the nuclear dipole-dipole interactions from $\mathscr{H}_0$ as argued earlier that these couplings are small compared to the hyperfine terms.

While we need not use the dipolar action for control, during long times of a relaxation process the slight change in eigenstates and symmetry breaking will slowly leak the information from the protected subsystem into the environment. Without further explanation, we suggest the possibility of approximate DFSes [5] or modeling the dipolar evolution as a finite correlation time noise process [139].

6.3 Generating Robust Control

Identification of a nuclear spin memory has many implications for small scale quantum information processors including quantum repeaters [17], spin-based storage [95]. In these applications quantum information must be transferred from a more volatile qubit to the memory with a high fidelity and should be done unitarily. As an odd quirk of nature, the precise Hamiltonians supporting logical qubits are not universally accessible. In order to encode into and out of the protected subspace you must break the symmetry, if only briefly, that gives you an encoding. In a system where the coupling between two spins could be tuned dynamically, either by changing the electromagnetic fields or moving particles apart, this task would be rather straightforward. For systems like those in magnetic resonance, the couplings are well-defined and cannot be rapidly changed. In essence there seems to be a trade-off between having robustness or control.

By dynamically modulating the Hamiltonian with external fields, we can attempt to symmetrize the Hamiltonian *on average*. This technique has its origins in magnetic resonance where multiple-pulse sequences have been used to remove interactions on average; the quantum information literature uses the moniker of "bang-bang" control, as the amplitudes used for modulating the system must typically be strong compared to the noise correlation time.

While decoupling the electron spin from the nuclear spin would indeed remove the effects of T_1^e relaxation on the nuclear spins, several arguments can be made in favor of resymmetrizing. First, to decouple with bang-bang style pulses the system must be able to support a large bandwidth response. For ESR systems, this includes

both a high-power amplifier with the ability to excite all interactions in the system simultaneously and a low Q resonator for dealing with nanosecond scale responses. Such low Q's are typically avoided in ESR as the inductive detection scales as $\sqrt{Q}$. For some optically detected systems [77, 66], hard pulse techniques may be possible.

One method of decoupling involves performing an average over a group, $\mathcal{G}$, such that the effective Hamiltonian of the system becomes some desired Hamiltonian [19]. If we want all of the nuclear spins to appear identical, this require averages of the cyclic group, C_N, where N is the total number of nuclear spins. Symmetrizing Hamiltonian thus corresponds to implementing the symmetries of the group.

As an example, take the smallest system capable of T_1^e robustness for a generic anisotropic Hamiltonian, C_3. C_3 has 3 rotational symmetries and three planes of reflective symmetries as seen in Figure 6-3. Implementing the rotational symmetries corresponds to an exchange of spins A and B, followed by an exchange of B and C. This net exchange must be done twice, so that spins A, B and C each stay in the three positions for an equal amount of time. The unitary operators for implementing such an exchange are:

$$U_{AB} = e^{-i\frac{\pi}{4}\vec{\sigma}_A\cdot\vec{\sigma}_B} \tag{6.21}$$

$$U_{BC} = e^{-i\frac{\pi}{4}\vec{\sigma}_B\cdot\vec{\sigma}_C} \tag{6.22}$$

$$U_{CA} = e^{-i\frac{\pi}{4}\vec{\sigma}_C\cdot\vec{\sigma}_A} \tag{6.23}$$

Alternatively, we can implement a series of six reflections to average over C_3. Such a six step cycle only requires a single exchange/swap for each step. Given that the symmetrizing must be done such that the total cycle time is much quicker than T_1^e ($\tau/T_1^e \ll 1$), one would expect the three-step cycle to outperform the six-step cycle. This would indeed by true if the unitary dynamics could be generated instantaneously Fig. 6-4. However, when the unitary dynamics must be generated using the natural Hamiltonian and by a modulation of the control Hamiltonian, the details of this process can affect which scheme is best. Not all unitary gates are created equal. For example, any gate $U_{\alpha\beta}$ above must be implemented on the combined 1e-3n system

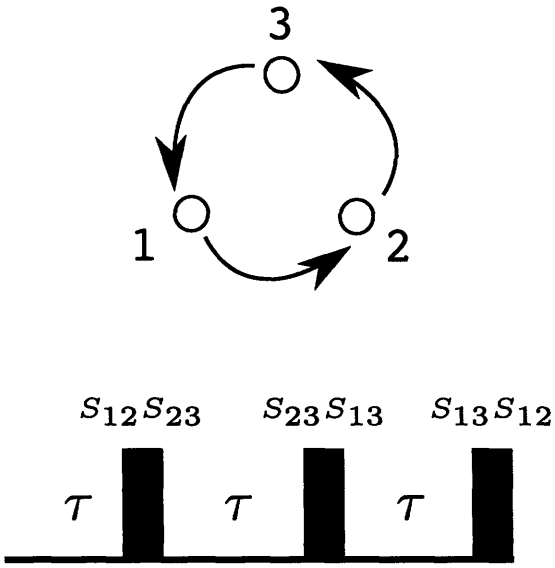

Figure 6-3: Dynamic Symmetrization (cyclic).

as $U_{net} = \mathbf{1}^e \otimes U^{3n}_{\alpha\beta}$. This has a tensor product decomposition: $\mathsf{U}(2) \otimes \mathsf{U}(2) \otimes \mathsf{U}(4)$. However, if we attempt to generate a single step of the rotation cycle we require an operator of the form $\mathsf{U}(2) \otimes \mathsf{U}(8)$. As the form of the anisotropic Hamiltonian and a simply control Hamiltonian can be written solely as tensor products of $\mathsf{U}(2)$, generating unitary gates span higher dimensional unitary groups requires longer time evolution.'

6.4 Conclusions

In this section we have elucidated a solution to electron T_1^e processes limiting coupled nuclear spin coherence times. For electron-nuclear systems where the hyperfine coupling takes on an isotropic form ($a_{\text{iso}}\vec{S} \cdot \vec{I}$), the electron spin flips induce uniaxial dephasing; however, in the anisotropic hyperfine case, the dephasing occurs along two orthogonal axes, leading to depolarization. A memory of nuclear spin qubits can still be achieved by going to logical encodings of qubits. While we have studied a few key logical encodings, the noise models we have presented do not take into account

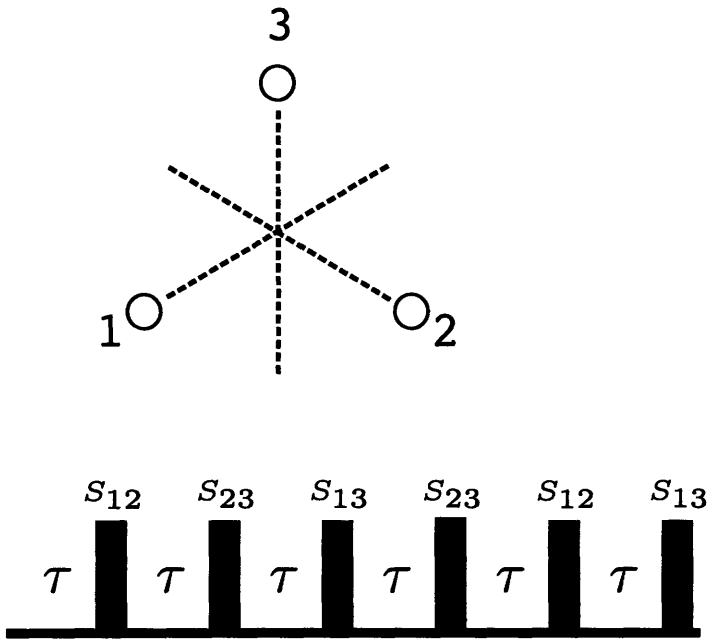

Figure 6-4: Dynamic Symmetrization (reflection).

any nuclear spin-lattice or spin-spin relaxation mechanisms. Further investigation under a complete noise model will give added insight into the dynamics and utility of these systems. Also, we have only studied the case of Markovian noise processes. Finite correlation times will dictate which symmetrization schemes work best and most robustly in realistic scenarios.

Chapter 7

Instrumentation

Pulsed electron spin resonance is a widely used technique in spectroscopy of paramagnetic substances [130], but has rarely been applied to observe coherent dynamics over large Hilbert spaces. As such dynamics are the ultimate goal of QIP, we have developed pulsed ESR instrumentation and techniques specific to engineering coherent control in electron/nuclear spin systems. In this section we describe the requirements, design, and operation of the microwave electronics and cryogenic probe.

7.1 X-Band Pulsed ESR Spectrometer

As described in Chapter 5, we wish to operate our quantum system of electron and nuclear spin state at a magnetic field where the anisotropic hyperfine interaction and nuclear Zeeman interaction have comparable strengths. For malonic acid $0.4T$ is a convenient field strength; with an electronic g-factor of $\sim$2, this corresponds to X-band microwave frequencies (8-12 GHz). Pulsed spectrometers operating in this range have existed since the mid-50s, as research groups modified CW ESR spectrometers to observe spin echoes. Technological improvements in microwave electronics gave rise to more sophisticated spectrometers in the mid-60s [100, 18, 63] and more recent advances throughout the 1990s introduced microelectronics to the pulsed ESR system [42, 41, 131, 12]. Furthermore, commercial pulsed ESR spectrometers can be purchased operating from the L-band (800 MHz) to the W-band (95 GHz), however,

these systems do not readily allow for arbitrary fast modulation of the microwave control fields — a requirement for robust control of the hyperfine interaction. Gaussian and Sinc shaped pulses have been used for EPR-based imaging techniques[35] and in limited spectroscopic applications[125], but arbitrary waveform generation on an X-band carrier frequency, though not technically challenging, has not been widely used by the pulse ESR community.

Our custom spectrometer benefits from advances in microwave technology in the X-band, driven primarily by communications and radar applications. This has allowed for miniaturization of passive (circulators, attenuators, directional couplers, etc) and active (amplifiers, phase shifters, mixers) components. Connectivity of the components can be achieved without waveguides using low-loss coaxial cables, allowing for a small form-factor spectrometer. We include PCI based acquisition and timing, where a digitizer and pulse programmer reside in the personal computer controlling the spectrometer. A library of quantum gates are easily transferred to the arbitrary waveform generator (AWG) using custom software.

Figure 7-1 shows a block diagram for the spectrometer. An Agilent E8254A (AA) microwave synthesizer provides the base microwave frequency, ν_B, up to 20 GHz, with kHz resolution. This signal is mixed with an intermediate frequency (IF) signal, $\nu_{IF} = 159\text{MHz}$, from a PTS-160 synthesizer (BB) matching the resonance frequency of our system $\nu_0 = \nu_B + \nu_{IF}$. A single-sideband upconverter supresses the first lower harmonic $\nu_B - \nu_{IF}$ and outputs ν_B. The carrier frequency is then amplified using a low noise 10 dB pre-amplifier (i) to drive a double-balanced mixer (j) with a 4GHz IF bandwidth. A 250 MHz signal from an AWG (CC) provides amplitude modulation of the carrier signal. Another amplification stage (g) compensates for the insertion loss of an ECL (emitter coupled logic) driven 6-bit digital phase shifter (h). A series of fast buffer amplifiers converts a 0-5V TTL signal to the -5V to 0V ECL levels. A variable attenuator (k, see Figure 7-2 for calibration curve) allows for adjusting the input signal to a 12W solid-state power amplifier with maximum output of 42 dBm, 50 dB gain and a 1 GHz bandwidth centered at 11.2 GHz (l). The sensitivity in coupling the spectrometer to the microwave resonator necessitates variable attenuation control

for the fixed gain amplifier.

The output of the power amplifier arrives at port 1 of a three port circulator (m)with $\approx$ 23 dB isolation between ports. Port 2 couples to a loop gap microwave resonator (described in the following section). Port 3 connects back to another circulator (m) for further isolation. A PIN diode power limiter (o) and a TTL microwave switch (n) provide two additional layers of isolation between the probe and the receive train when pulsing at high power. The switch can be triggered closed during acquisition with roughly a 300ns deadtime.

Acquisition begins after the switch with nearly 100dB of gain in multiple stages. First, a receiver frontend (p) mixes down the signal near ν_0 with the base frequency (ν_B), obtained from a directional coupler (z) off the main microwave synthesizer. This component amplifies the signal by 30 dB and has a noise figure of 2.5dB. A high-gain low-noise preamplifier (t) provides 25dB of IF gain; further amplification (u) brings the $\approx$ 159 MHz signal up another 25dB. A 90° hybrid splits (v) the IF signal into in-phase and quadrature components that are mixed down to DC with two IF double-balanced mixers (x) with the PTS source providing a local oscillator for phase sensitive detection. Two low-pass filters (y) remove the harmonics from the mixers. Each of the quadrature channels are then digitized with a PCI based 100MHz, 14-bit digital acquisition card (National Instruments NI-5122)

A PulseBlasterESR (SpinCore) PCI-based pulse programmer operating at 300 MHz allows for 3.3ns resolution for any instruction word. This device provides 4 BNC channels capable of driving TTL lines and 24 additional channels buffered to drive additional TTL lines. The pulse programmer controls the following time-critical parts of the spectrometer: switch gating, amplifier blanking, digital phase shifting, AWG triggering, and digitizer triggering. To specify the amplitude modulation of the microwave carrier, shaped waveforms are loaded onto the AWG using a GPIB interface (Measurement Computing PCI-GPIB-300K).

A key calibration in the optimal operation of the spectrometer is the linear scaling of the power amplifier output. As we mix a 250 MHz modulation from our AWG with the main microwave carrier (ν_B), the voltage levels of modulation will affect the mixer

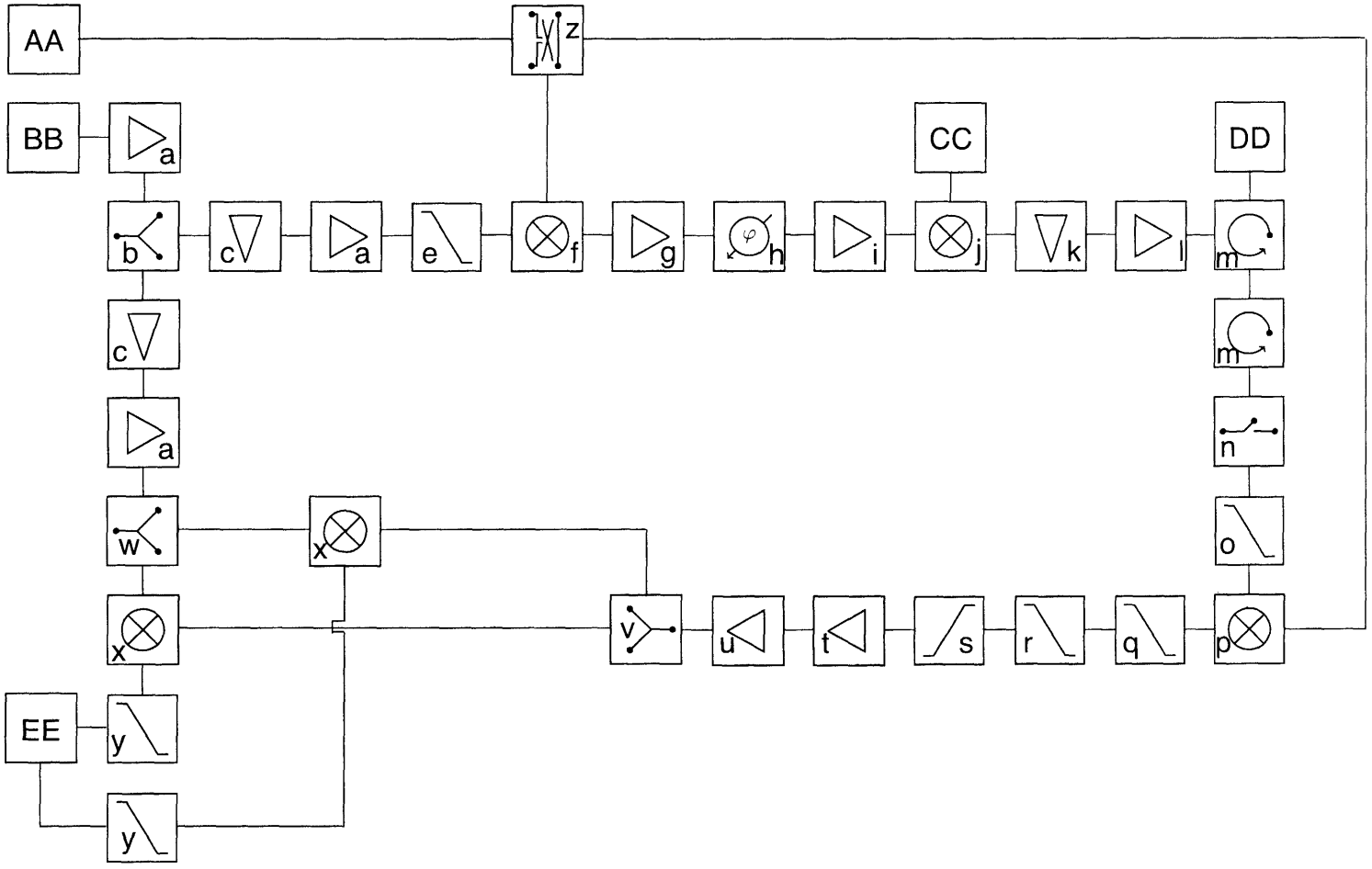

gure 7-1: Block Diagram of Microwave and RF Electronics for Pulsed ESR Spectrometer. Details of the componer sponding to lowercase labels can be found in Table 7.1. The capital letters are reserved for separate, complex comp crowave synthesizer (AA), the RF synthesizer (BB), the AWG (CC),the probe (DD) (See 7.2), and dual channel d E).

Component	Manufacturer	Part No.	Diagram
RF Amplifier	Mini-Circuits	ZFL-1HAD	a
Power divider	Mini-Circuits	ZMSC-2-1	b
Attenuator	Mini-Circuits	SAT-10	c
Low Pass Filter	Mini-Circuits	SLP-300	e
SSB Upconverter	MITEQ	SM0812LC2MDC	f
Microwave Amplifier	Mini-Circuits	ZX60-14012L-S	g
Digital Phase Shifter	MITEQ	PS-0618-360-5-5.6	h
Microwave Amplifier	MITEQ	AFS-2-10701370	i
Double-Balanced Mixer	MITEQ	DM0812LW2	j
Attenuator	ATM	AF966-10	k
Power Amplifier	Microwave Power	L1112-41-TL39	l
Circulator	Ditom	D3C1112	m
Microwave Switch	ATM	S1517D	n
Limiter (PIN-PIN Diode)	Eclipse Microwave	EPL8012A3	o
Receiver Front-end	MITEQ	AR0812LC2C	p
Low Pass Filter	Mini-Circuits	VLP-64	q
Low Pass Filter	Mini-Circuits	SLP-200	r
High Pass Filter	Mini-Circuits	SLP-50	s
IF Amplifier	HD Communications Corp.	HD18440	t
IF Amplifier	Mini-Circuits	ZFL-500LN	u
90° Hybrid	Pulsar	QE-07412	v
Power divider	Mini-Circuits	ZX10-2-12	w
Mixer	Mini-Circuits	ZFM-3	x
Low Pass Filter	Mini-Circuits	SLP-50	y
10 dB Directional Coupler	ATM	C116-10	z

Table 7.1: Microwave and RF components.

(j) output amplitude fed into the power amplifier (l). For shaped pulsing, this voltage varies discretely from 0% to 100% with 8-bit precision; we need the amplifier output to correspond linearly to any input signal as the engineered quantum gates depend on such linearity. The variable attenuator (k) is set such that we do not saturate the amplifier and a flat modulation signal at 100% corresponds to the maximum power output (42dBm). We calibrate the linearity by adding 120 dB of attenuation after the power amplifier and feeding the amplifier output directly into the receiver front end (p). (The large degree of attenuation excludes saturation effects from the receiver front end.) The usual heterodyne detection, less one IF amp (u) allows us to observe a DC signal proportional to the amplifier output. We specify flat (boxcar) shaped pulses with amplitudes ranging from 10% to 100% of the maximum output voltage of the AWG. We then take the mean digitized DC level after a series of 256 scans and plot this level for different settings of the variable attenuator (k) in Figure 7-2. Using this data, we set the maximum AWG output voltage to 300mV (pp). We have also used a 6th order polynomial fit to some of the non-linear traces (4 and 5). By inverting the polynomial, we can then adjust the input voltage nonlinearly to ensure linear output (not shown). This allows for shorter $\frac{\pi}{2}$ times and modulations sequences.

7.2 Low-Temperature Pulsed ENDOR Probe Design

The novel spectrometer presented in Section 7.1 enables the use of optimal control techniques and pulse shaping in ESR for an electron-nuclear spin system. Next, we focus on coupling the magnetic fields arising from electron spin magnetization to the spectrometer by means of a resonant structure. At microwaves frequencies, TE or TM mode cavities in rectangular or cylindrical geometries [113] can provide high Q resonant structures; loop-gap resonators (Section 7.2.1), dielectric resonators, and stripline resonators and their variations can have Q's of 1 to 10, 000 but the dimen-

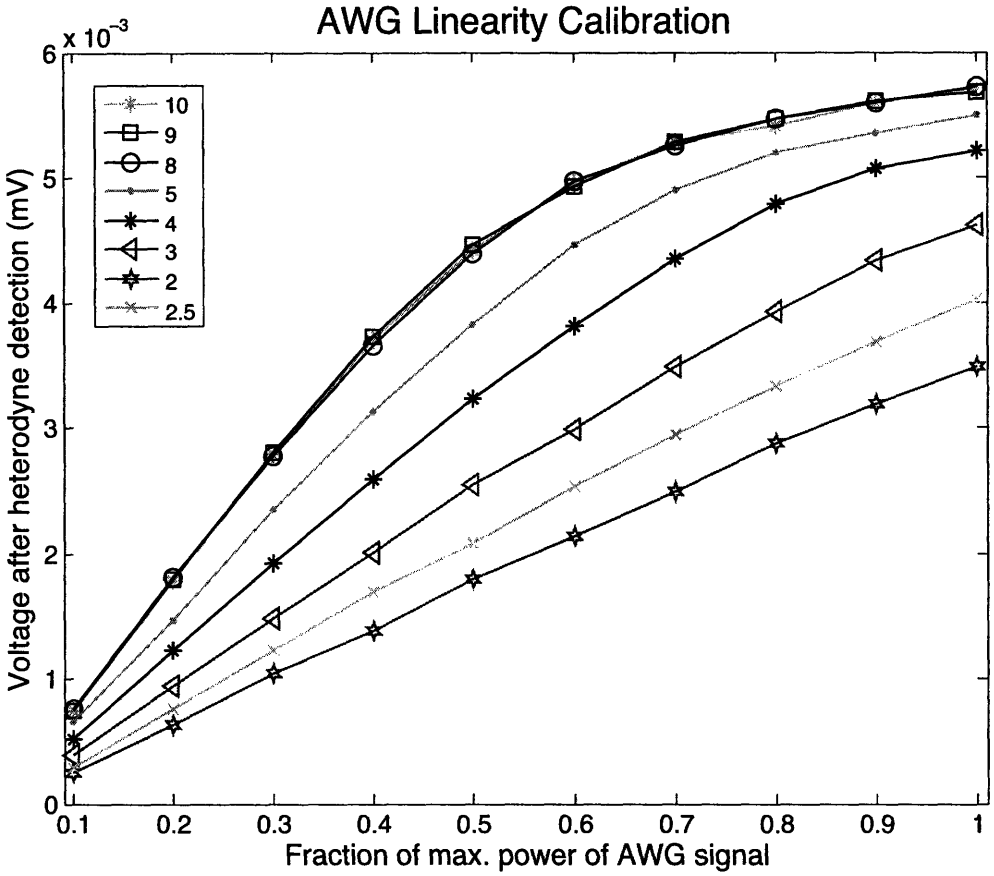

Figure 7-2: Microwave Power Amplifer Linearization. Each curve shows the heterodyne detected output for a specified AWG input signal. At small attenuation (10-8) the amplifier begins saturation at 40% of the maximum AWG signal. Linear operation begins at a setting of 3.

sions of the resonators are typically on the order of the wavelength of the radiation. Many previous probe designs [41, 27] for pulsed ESR and ENDOR (electron-nuclear double resonance) provided us insight into microwave materials, coupling mechanism, geometries, etc.

The probe for our ESR or ENDOR spectrometer not only holds the resonator, but most also provide a stable mounting of the sample within the resonant cavity. For room temperature (300K) studies this is usually a trivial matter; for low-temperature/cryogenic studies several additional factors must be taken into account. First, there must be a means of conducting heat from the cryogenic bath to the sample. This can be done by submersing the sample into the cryogen or by using a cold-finger device (Figure 7-6) with appreciable thermal conductivity at the temperatures of interest. Care must be taken to isolate the low temperature components from ambient temperature and minimize conductive, convective, and radiative heat losses. Radiative losses ($\dot{q} \approx T^4$) are minimized using a radiation shield thermally sunk to liquid nitrogen temperatures. We evacuate (10^{-5} torr) the sample space to reduce convective losses.

7.2.1 Loop gap resonators

The loop gap resonator [93, 94, 47, 46] is a resonant structure with dimensions on the order of the microwave wavelength. The basic idea comes from modeling a slotted tube as a lumped element device. A cylindrical conductive tube of length z and with radius r gives rise to a natural inductance L when current flows along the surface of the conductor. If slots of thickness t are made down the length of the tube, the current cannot flow along the slots and a charge buildup at the gaps will give rise to a capacitance C. This device will resonate at a frequency of roughly $1/\sqrt{LC}$. An oscillating current flowing azimuthially around the loop gives rise to a magnetic field along the long axis of the tube. The electromagnetic fields can be further confined by placing the loop-gap in a larger diameter conductor of radius R. Slight empirical corrections give the formula for determining the resonance based on the geometric factors, as reported by Hyde [46]. Figure 7-3 shows a schematic of the loop gap

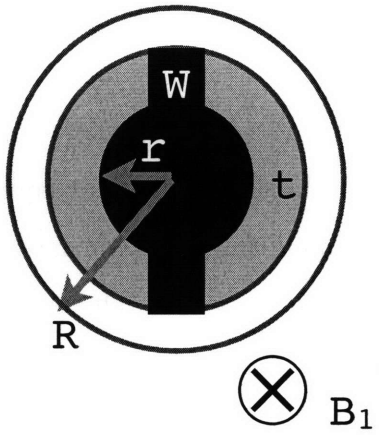

Figure 7-3: Loop Gap Resonator. r defines the inner radius and R is the radius to the shield. W is the gap width and t is the thickness of the conducting cylinder. Z defines the overall length of the resonator and only contributes to the resonance due to stray fields when Z is comparable to r. n defines the number of loops. The inductance of such a structure is $L = \mu_0 \pi r^2 / Z$; the capacitance is $C = \epsilon W Z / tn$.

resonator.

The quality factor of the resonator depends on the conductivity of the materials used, the dielectric constant, ϵ, of the materials between the conductors, and the uniformity of the gaps. Coupling to the resonator can be achieved inductively by placing a loop of the inner coaxial conductor near the end of the loop gap resonator or capacitively by coupling the inner conductor of a coax (or antenna) to the gap.

Our loop gap resonators were constructed from oxygen-free high conductivity copper tubes with an outer diameter of 4mm, inner diameter of 3mm, and lengths ranging from 4mm-12mm. Two gaps ranging from 0.25mm - 0.50mm were made along long axis. The slotted copper tubes are then inserted into fused silica (quartz) tubes (ID=4mm, OD=6.4mm) and affixed to the inner surface using a cyanoacrylate adhesive with care taken to keep the gaps smooth and free of adhesive. An outer shield (OD=10mm) is placed around the loop gap resonator. These devices will resonate between 10.500 GHz and 12.100 GHz. Measurements using a microwave network analyzer show a Q of about 250.

7.2.2 Generation 1 Probe

In the design of our probe, we have tried to satisfy constraints on the sample temperature, easy of access, compatibility with existing equipment and modularity. Our first task was to arrange for sample and resonator mounting with an existing Janus DT cryostat. Figure 7-4 shows the probe tail. The outer vacuum shield (A) attaches to the helium dewar via a viton o-ring seal. An aluminum vacuum box (E) accommodating the resonator and any electronics is welded to (A). The bottom plate (see Figure 7-5) mates with the vacuum box and seals with an o-ring (D). The OFHC copper cold plate (C) mounts to the helium space of the dewar via an indium seal and can be cooled to 4K. The radiation shield (B) sits flush against to the nitrogen space of the dewar and remains at 77K to reduce radiative losses. The assembled tail is positioned between the two pole pieces of an electromagnet such that the sample coincides with the most homogenous part of the magnetic field.

The bottom plate design (Figure 7-5) provides convenient, modular access to change samples or resonators. Inductive coupling to the loop gap resonator is achieved by bending the inner conductor of a 0.141" coaxial cable (A) into a teardrop shaped loop and soldering the inner conductor to the coaxial shied. Given the assymmetry of the coupling loop with respect to the loop gap resonator, impedance matching of the transmission line (coaxial cable) to the resonator depends both on the relative orientation of the coupling loop and the distance from the surface. A major concern is the robustness and reproducibility of moving the coupling loop toward and away from the loop gap resonator.

Berillium copper bellows provide a means for retaining vacuum and permitting linear motion of the coupling loop without using a proper vacuum feedthrough. Unfortunately, the restoring force of the bellows causes lateral and bending motions; this is problematic for maintaining the alignment of the coupling loop. We compensate for this by silver soldering both end of the bellows to 6mm thick brass endcaps (C&D); the coaxial cable was soldered to one of the brass pieces to complete a vacuum seal. Both brass pieces fit snugly into the barrel of brass holder (F) in order to prevent

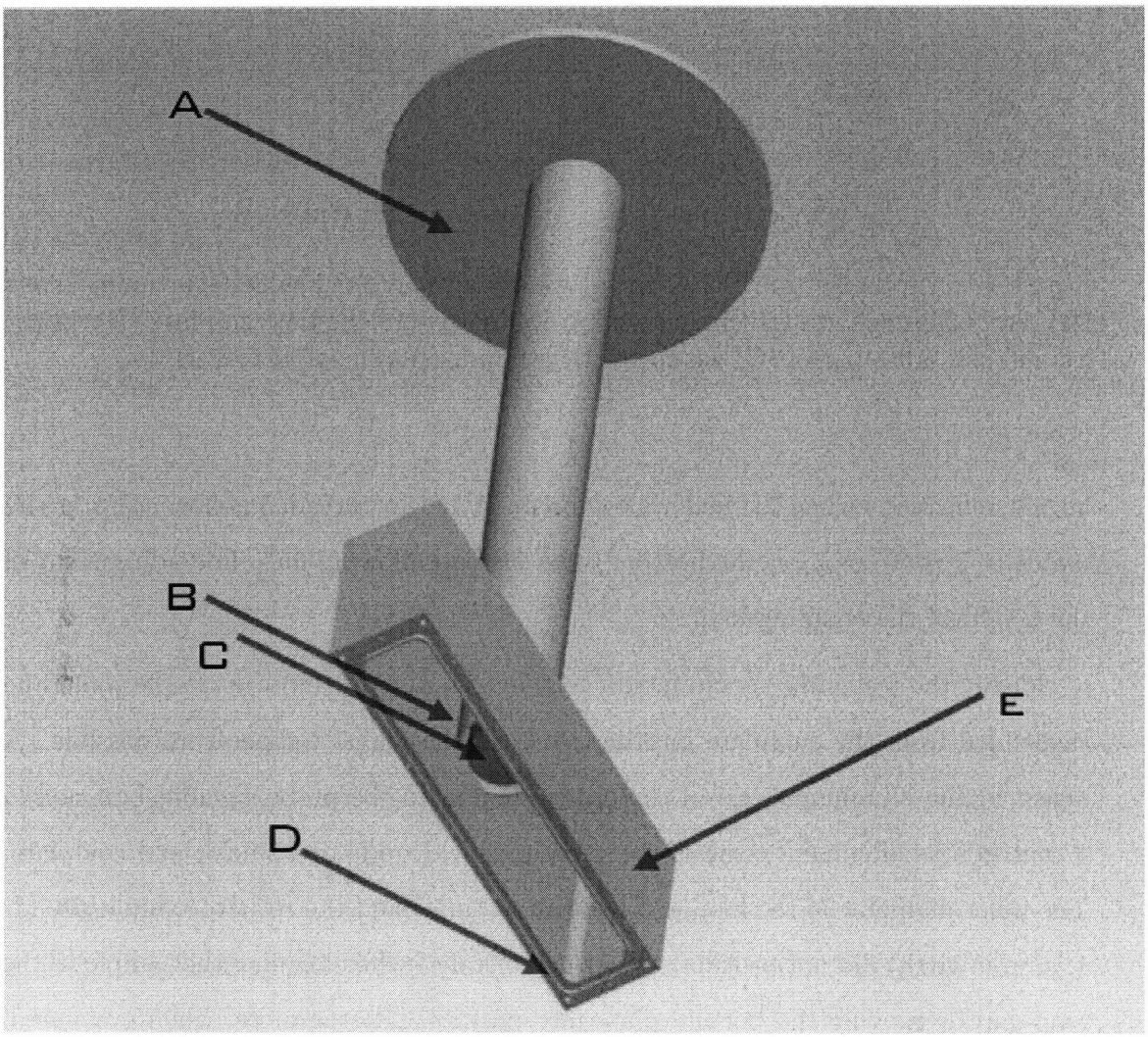

Figure 7-4: Cryostat-Probe Interface. Outer vacuum shield (A). Radiation Shield (B). Copper cold plate (C). O-ring groove (D). Vacuum Box (E).

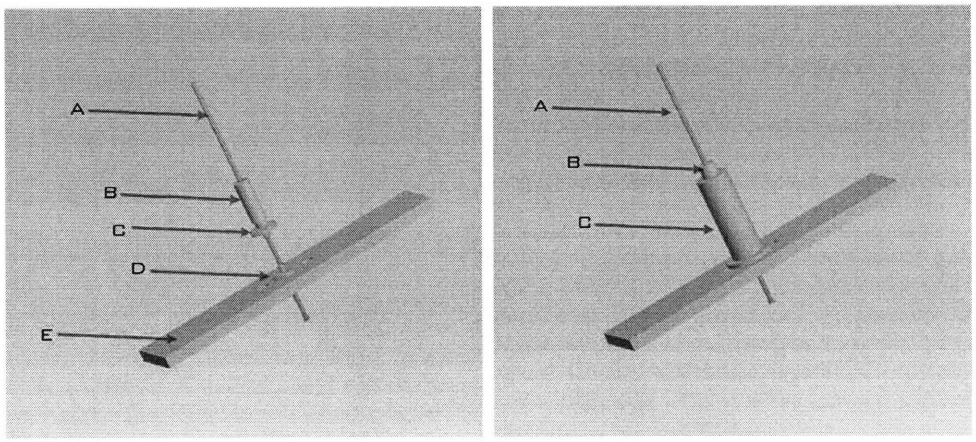

(a) Without Barrel (b) With Barrel

Figure 7-5: Probe Bottom Plate. In (a) we show the coaxial cable (A), tuning screw (B), and brass bellows attachments (C & D) relative to the bottom plate (E). In (b) we add the brass barrel (C) which restricts lateral movement of C & D.

lateral deflections when the bellows compress. A 1/4-40 threaded hollow adjuster (B) mates to a protrusion on the bottom brass endcap allowing for a fine adjustment of the height of the coupling loop.

Ideally the resonator should mount to the bottom plate and the sample should be suspended from the coldplate in order to reach the lowest temperature possible. A defect in the aluminum weld of the outer vacuum to the probe vacuum box caused a central axis alignment issue of the vacuum shield, radiation shield, and coldplate. The inner diameter of the loop-gap resonator (3mm) and the relative sample size (1-1.5mm in girth) did not provide a generous tolerance when aligning the sample to the loop gap by moving the bottom plate into position. Furthermore, when evacuated, forces on the outer vacuum shield changed the relative position of the OVC to the cold finger causing further distortions. To ensure proper sample-resonator alignment, we have designed a rexolite holder (Figure 7-6) containing the loop gap resonator, shield and sample in one complete package. Angular references on the top surface allow for changing the sample's rotational alignment with respect to the main magnetic field — an essential piece to tuning the anisotropic hyperfine interaction. With this design, the sample and loop gap resonator can be aligned [relative to the coupling loop]

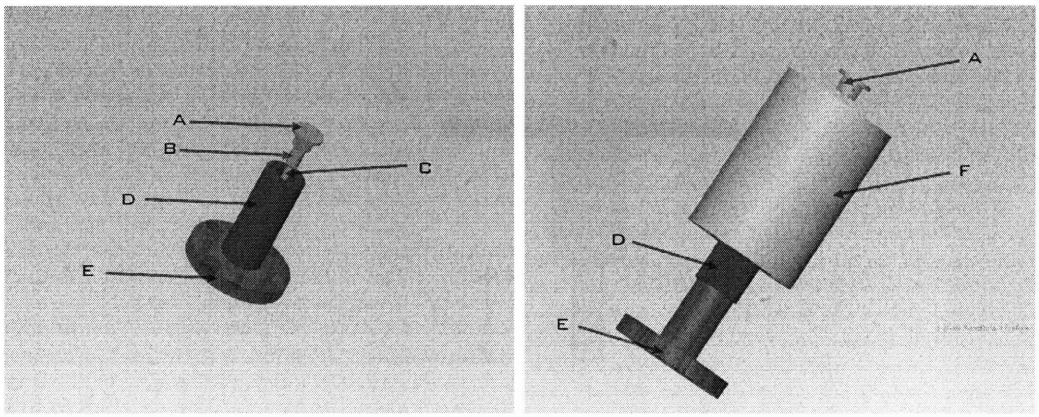

(a) Bottom rexolite holder (b) Rexolite Holder (Exploded View)

Figure 7-6: Rexolite Sample Holder. The lower half of the rexolite holder (a) is comprised of a two-piece copper quartz rod holder (A & B), quartz rod (C), outer shield (D), and rexolite piece (E). The loop gap resonator (not shown) mounts along the center axis. The upper half (b) consists of another rexolite holder (F) with 15° markings where (A) mounts for sample orientation.

outside of the probe box and mounted directly to the copper cold finger. Thermal contraction of the device at 4K and the increased thermal mass of the rexolite holder prevent us from cooling the sample to liquid helium temperatures. At liquid nitrogen temperatures (77K) the relaxation properties and polarization of the samples of interest are appreciable; thermal contractions of the loop gap resonator, while finite and observable in its frequency response, do not impede the observance of electron spin resonance.

Once the sample, resonator and bottom plate have been completely mounted, we evacuate the sample space and cool the entire system to 77K. Mechanical movements due to ambient pressure and thermal contractions of the resonator necessitate further impedance matching of the coupling loop to the loaded resonator. To measure the relative impedance, we attach the probe and a microwave synthesizer to a three port circulator and measure the reflected power on the third port with a diode detector. When the probe is matched to the transmission line (50Ω), the observed voltage from the diode detecter approaches zero (see Figure 7-7). In Figure 7-8 we show this voltage as a function of microwave frequency for different adjustments to the coupling

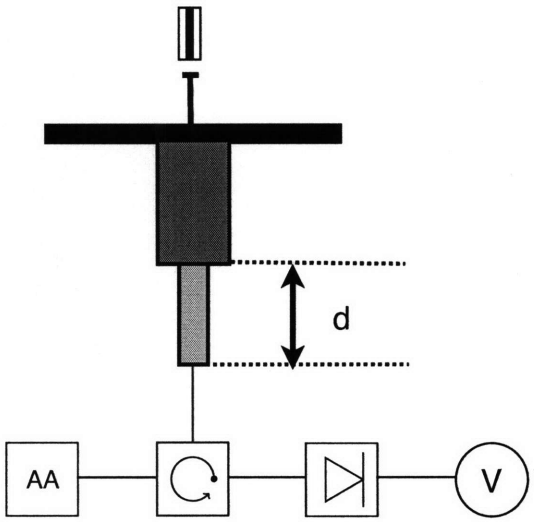

Figure 7-7: Resonator Measurement Setup. A swept microwave signal (AA) and the probe are attached to a three port circulator. A diode detector measures the output voltage as d0 is varied.

loop height. Optimal coupling usually occurs when the edge of the coupling loop is within 2-3mm of the resonator end.

7.3 Future Directions of Instrumentation

Our probe and spectrometer have allowed us to demonstrate universal control in a one electron, one nuclear spin (1e-1n) quantum information processor. However, initial investigations into a 1e-2n system suggest that faster hardware and phase sensitive modulation, although mathematically not necessary, may be useful. In addition, a desire to study samples (like Si:P) with strongly temperature dependent relaxation times [1] motivates changes to the sample mounting. In short, the design, assembly and usage of this ESR spectrometer has brought to light many of the shortcomings of this first generation instrument. In this section, we will outline some future directions for extending the current design to study larger Hilbert spaces or different spin systems.

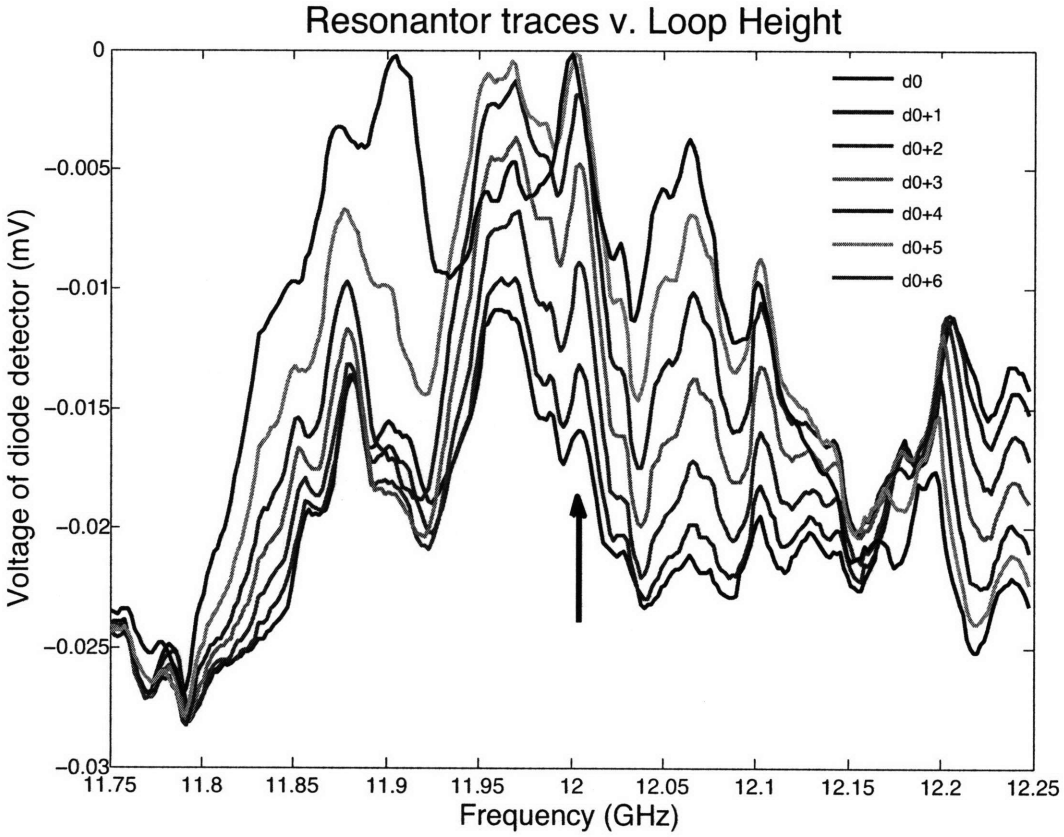

Figure 7-8: Impedance Matching of Loop Gap Resonator. Each traces shows the impedance mismatch of the probe to a 50Ω tranmission line as measured with a diode detector. $d0$ represents an equilibrium position of the coupling loop; the integers represent turns of a 1/4-40 screwthread. This resonance of this loop gap is around 12.004 GHz as indicated by the arrow.

7.3.1 Spectrometer component advances

In accordance with our numerical investigations for control of large Hilbert spaces, a future design benefits from faster, phase sensitive modulation and increased microwave power. The modulation rate of a microwave carrier signal is fundamentally limited by the frequency of that carrier signal, roughly 10-12GHz for our system. With a 1-2 Gs/s AWG, we can generate pulses shaped with 0.5-1ns time steps well within our X-band carrier. In addition, in phase **and** quadrature modulation of the carrier signal provides an additional control parameter. When engineering quantum gates numerically, the algorithms converge to satisfactory solutions quickly with this additional parameter. Moreover, strong/fast perturbations to the system yield shorter quantum gates. A 1kW X-Band traveling-wave-tube (TWT) microwave amplifiers or 120W solid-state microwave amplifiers would provide the higher nutation frequencies we desire . As the oscillating magnetic field in the resonator scales as the square-root of the power, a 100-fold increase in power would only give a 10-fold increase in our control amplitude. Next, one needs to upgrade the pulse programmer, which controls the timing of all aforementioned parts. Commercially available sub-nanosecond timing and at least 12 independent control lines would provide ample timing resources. Lastly, a larger bandwidth heterodyne detection module will allow for observation of more strongly coupled hyperfine systems. Modifications of the detection module include increasing the IF frequency above the current value of 159MHz and any removal of bandwidth limited components. A digitizer with sampling of 1Gs/s will also allow for finer observations of echo modulations.

7.3.2 Probe advances

As the sample and control fields are coupled via a finite-bandwidth resonator this too must increased. In Chapter 3, we outlined how distortions of shaped pulses due to tuned-circuit ringing degrade the fidelity of an engineered quantum gate. With a resonator Q of 250 and a resonance frequency of 12 GHz, we can expect a bandwidth of 48 MHz. Even our current modulations rates are outside the limitations of this

resonator. Degrading the Q (and increasing the bandwidth) can be achieved by insertion of a lossy dielectric material, changing the material of the resonator to one with a lower electrical conductivity, or by changing the geometry. This last option may be promising, as the current resonator design does not have a broad tuning range. Samples with differing dielectric constants can load the resonator and lower the resonance frequency, as can thermal changes, like temperature dependent electrical conductivity or contractions changing the gap sizes of a loop-gap resonator. Ideally, we would like to pick a single resonance frequency and tune the resonator, as opposed to the current method where the loop gap resonance defines the operating frequency. Bridged-loop gap resonators [111, 61] and stacked dielectric resonators [64] are both options.

While providing increased modulation bandwidth, decreasing the Q reduces the detection sensitivity. The sensitivity of the detected field, assuming thermal resistive noise, scales as $\sqrt{Q/V_c}$ [2], we can compensate for increased resonator bandwidth with decreased resonator volume (V_c). Another way to increase the sensitivity is to increase the polarization of the sample by going to lower temperatures (see Figure 7-9). The cold plate of the old design can be removed and the sample placed directly in liquid helium. Rotating the sample with respect to the magnetic field can occur directly with a series of support stages and a mounting rod. Further support structures will be necessary to adjust the alignment of the sample within the resonator.

In short, improvements to the spectrometer involve increased bandwidth and a variety of trade-offs. A necessary decrease in the Q of the resonator can be compensated for by going to lower samples temperatures, small volumes, and higher power amplifiers.

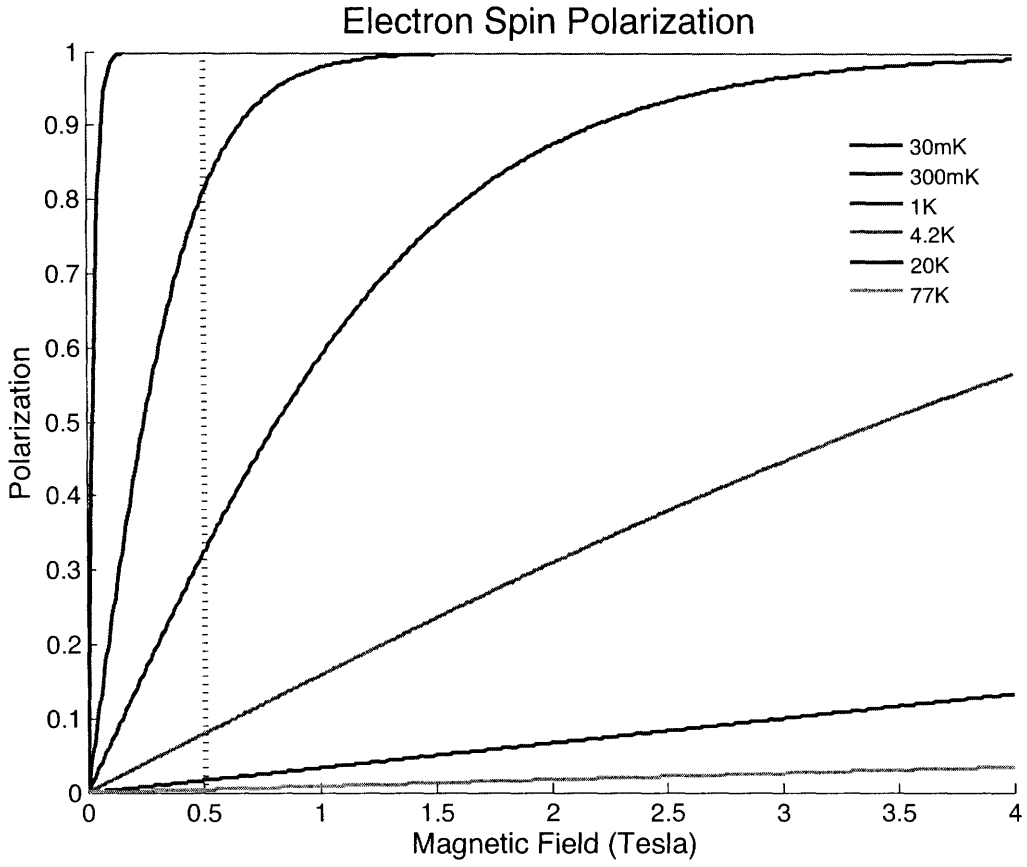

Figure 7-9: Polarization of electron spin (S=1/2). For several key temperatures, we plot the electron spin polarization as a function of magnetic field: $P = \tanh(\frac{\beta\hbar Bg}{kT})$. For magnetic fields compatible with the anisotropic hyperfine interaction, roughly 33% polarization can occur near liquid ^{4}He temperatures.

Chapter 8

Conclusion

In the preceding six chapters, I have developed several tools for coherently controlling quantum information in a variety of physical settings and have shown demonstrations of their feasibility. Methods developed using liquid state NMR include improving the system model of classical control fields, controlling logical qubits in the presence of leakage, decreasing the signal loss in state preparation for logical encodings, and understanding real-world implementations of optimal control methods. In addition, I show how these techniques, developed in a test-bed system, are applicable to other technologies, including solid-state spin systems.

To control nuclear spins by an electron spin actuator represents a new paradigm for coherent quantum control: accessing a subsystem without directly addressing the qubits within the subsystem. The faster gate times seen for the 1e-1n and 1e-2n systems can be expected with additional nuclear spin qubits provided the hyperfine interactions are as strong. This added resource does not come without cost, as environmental coupling to the electron spin manifests itself as depolarizing noise on the nuclear subsystem. Here, the insights gathered from implementing logical encodings in the liquid state can be applied to find a noiseless/decoherence-free subsystem of nuclear spins in the solid-state. As the Hamiltonian required for complete controllability of the system and the Hamiltonian necessary for an NS without leakage are mutually exclusive, the same types of modulation techniques used in Chapter 4 to limit the leakage can be used to generate the correct symmetries on average.

8.1 Outlook

The universality of the anisotropic hyperfine interaction is relevant to most solid-state quantum information proposals. In these systems both the electron and nuclear spins can serve as qubits and as environments. Where the interactions can be resolved, those parts of the system can be controlled. The idea of one species corrupting the coherence of another is true on a large scale, but locally the systems are universal. When possible the largest completely controllable quantum system should be used; decoupling usable spins in the presence of available control is a waste of a valuable resource.

As the size of any controllable quantum system grows, the operational fidelity of quantum gates in general decays. While nature's abhorrence of a quantum computer is an unanswered question, progress towards a large scale quantum computational device — capable of eclipsing the power of classical computers — proceeds at a slow, steady rate. In light of the long timescale expected until the dawn of quantum computation, one can ask the question: *What sort of small-scale coherent solid-state devices could be made by drawing from QIP ideas?* One possible idea is a quantum repeater or memory for storing the state of a photon or short-lived qubit for an extended period of time and then moving it onward. This could extend the coherence time of the original state. Another possibility is a few qubit processor implementing the phase estimation algorithm. As the speed-ups of most quantum algorithms rely on the phase of the quantum state and finding a periodicity, the ability to monitor the phase of a quantum state can have applications in interferometry, quantum metrology, and quantum simulations.

8.2 Extensions of Logical Qubits in Liquid State NMR

Improved models of control fields, subsystem pseudo-pure states, and encoded logic presented in this thesis can be extended into more complex encodings with the hope

of achieving higher fidelity control over multiple layers of logically encoded qubits. With six qubits, fully concatenated error protection schemes could be implemented. For example, by adding another logical qubit like that used in Chapter 4, the system ground state will be $|0\rangle_{1L}|0\rangle_{2L}|0\rangle_{3L}$. These three logical qubits can then be used for yet another encoding with the basis state $|0\rangle_l = |0\rangle_{1L}|0\rangle_{2L}|0\rangle_{3L}$ and $|1\rangle_l = |1\rangle_{1L}|1\rangle_{2L}|1\rangle_{3L}$. This new logical qubit would be robust to pairwise collective $\hat{z}$ noise to infinite depth and a σ_x^L noise to first order. $(|0\rangle_l + |1\rangle_l)/\sqrt{2}$ is a GHZ state of collective z DFS qubits. Alternatively, one can encode against σ_x errors first and then logically collective phase errors by switching the order — a DFS qubit made from two physical GHZ states. While the encodings can be analyzed theoretically given a particular noise model, studying the coherence properties of these two states experimentally will provide insight into the mechanisms of decoherence. These properties will depend greatly on the molecule used as the quantum information processor. Indeed, recent work using NMR on liquid crystals [60] shows an improvement in fidelity by using a logical encoding. Lastly, subsystem pseudo-pure states enable a more efficient study of any logical qubit states by simplifying the state preparation; the accompanying measures of fidelity over the logical degrees of freedom will enable a measure of leakage in implementation.

Further improvements can also be made in the methods used to engineer unitary transformations. First, the bandwidth limitations of the device used to couple the control fields to the spin system (e.g. the coil of the RF circuit) should be included in the system model used to find control sequences. This can be done by either simulating the control field explicitly with a convolution kernel or putting a penalty on fast modulations. For open quantum systems, the algorithms used to engineer quantum gates do not take into account relaxation processes. The implementation used in Chapter 4 maximally leaves the subspace of a single qubit when rotations of σ_x^L are required. By adding a relaxation superoperator to the SMP or GRAPE algorithm, as well as penalties for time spend outside of the subspace, it may be possible to find a path through Liouville space that minimizes decoherence due to leakage during a σ_x^L operation. Finally, as the systems scale in size, using simulations

of large quantum systems to find control sequences becomes inefficient. It may be possible to use the quantum information processor itself as a "simulator", whereby measurements of the quantum state can be used to assess the fidelity of the quantum operation. The modulation sequence can then be iteratively altered to improve the gate fidelity. Similar ideas have been implemented in atomic ensemble systems [105].

8.3 Extensions of Anisotropic Hyperfine Control

Control of nuclear spin qubits local to an electron spin via the anisotropic hyperfine interaction provide a new tool engineering small scale quantum registers. The 1e-1n implementation (Chapter 5) shows that AHF control is possible by measuring quantum phase evolution of the nuclear spins on the electron spin. The next step would be to assess the goodness of the quantum gate implementation using a quantitative measure, like gate fidelity. This would also require pseudo-pure sequence for the ensemble system, not like that of liquid state NMR. In fact, we have found the modulation sequences for implementing the necessary rotations of a pseudo-pure state reported in [96]. It is likely that some gates will not perform as intended due to bandwidth limitations of the resonator; improvements to the optimal control algorithms can account for this bandwidth and should give increased fidelities. The possible difference in nuclear spin relaxation times of the two manifolds (T_2^α vs. T_2^β) is yet another property of the AHF system that needs to be investigated. Gate engineering can be used to simplify the measurement of the relaxation superoperator. Lastly, The 1e-2n malonic acid system (Chapter 5) is an ideal candidate for immediate demonstration of a nuclear-nuclear gate.

To extend these AHF systems to be used as a quantum memory, I have shown that at least three nuclear spins are necessary for the nuclear T_2 to extend past the electron T_1. One possible sample for showing this is a phosphorous donor embedded in a lattice of silicon. NMR measurements of the nuclear T_2 in bulk ^{29}Si show coherence times of several seconds to minutes. These times will degrade near a donor electron, but should be long given no other nearby defects. The geometry of the four silicon-29

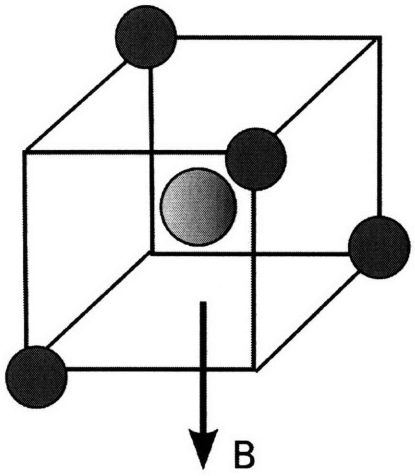

Figure 8-1: Isotropic DFS with Si:P. The nearest four silicon atoms to a phosphorus defect provide the correct geometry for a 1e-4n logical qubit. The dark (blue) spheres are ^{29}Si atoms. The light (yellow) sphere is a ^{31}P atom.

atoms in the E-shell of the defect silicon lattice [150] (see Figure 8-1) readily provides the symmetry necessary for a 1e-4n isotropic DFS[1]. Universality can be recovered by reorienting the crystal with respect to the magnetic field and applying a sequence to induce a time-averaged symmetry to the Hamiltonian. The isotropic hyperfine coupling of the phosphorus will divide the system into four separate manifolds instead of just the two of the electron spin states. Engineering of such a system may be beyond the forefront of silicon technology, but should provide a very clean quantum memory. If these local quantum memories can be connected in an efficient, coherent manner, we can build the basis of a larger, robust quantum processor.

Finally, in order to scale these quantum memories controlled via the anisotropic hyperfine interaction beyond one logical qubit the local processors must be connected. The electron spin provides a "handle" for linking these two systems in a variety of ways: optically when such an excitation exists, electrically if the system is a metal/semiconductor, or through modulating of the dipole-dipole interaction between two electrons. Strong measurements of the electron spins can then entangle two

[1]The isotropic DFS is spanned by the two basis vectors $|0\rangle_L = |s,s\rangle$ and $|1\rangle_L = \frac{1}{\sqrt{3}}\big(|t_+,t_-\rangle + |t_-,t_+\rangle - |t_0,t_0\rangle\big)$. $|s\rangle$ is the singlet state and $|t_{0,+,-}\rangle$ are the J=1 triplet states with J_z angular momentum 0,+1, and -1 respectively

or more nuclear subsystems into a robust multiple logical qubit quantum memory.

Appendix A

Cumulant Methods

We calculate the ensemble average of a time-ordered exponential in terms of the cumulant expansion. First, expand the time-ordered average exponential $S = \langle \mathcal{T} \exp(-i \int_0^t dt' \mathscr{H}(t')) \rangle$ via the Dyson series:

$$\begin{aligned} S &= \mathbf{1} - i \int_0^t dt' \langle \mathscr{H}(t') \rangle + \tfrac{(-i)^2}{2!} \mathcal{T} \int_0^t dt_1 \int_0^t dt_2 \langle \mathscr{H}(t_1) \mathscr{H}(t_2) \rangle + \cdots \\ &\quad + \tfrac{(-i)^n}{n!} \mathcal{T} \int_0^t dt_1 \cdots \int_0^t dt_n \langle \mathscr{H}(t_1) \cdots \mathscr{H}(t_n) \rangle + \cdots \end{aligned} \tag{A.1}$$

The term $\langle \mathscr{H}(t_1) \cdots \mathscr{H}(t_n) \rangle$ is called the n-th moment of the distribution. We want now to express this same propagator in terms of the cumulant function $K(t)$, defined by:

$$S = e^{K(t)} \tag{A.2}$$

The cumulant function itself can most generally be expressed as a power series in time:

$$K(t) = \sum_{n=1}^{\infty} \frac{(-it)^n}{n!} K_n = -itK_1 + \frac{(-it)^2}{2!} K_2 + \cdots \tag{A.3}$$

Expanding now the exponential (A.2) using the expression in equation (A.3) we have:

$$\begin{aligned} S &= \mathbf{1} + K(t) + \tfrac{1}{2!} (K(t))^2 + \cdots \\ &= \mathbf{1} - itK_1 + \tfrac{(-it)^2}{2!} (K_2 + K_1^2) + \cdots \end{aligned} \tag{A.4}$$

where in the second line we have separated terms of the same order in time. By

equating terms of the same order in Eq. (A.4) and (A.1) we obtain the cumulants K_n in terms of the moments of order at most n. For example:

$$\begin{aligned} K_1 &= \frac{1}{t}\int_0^t dt' \left\langle \mathscr{H}(t') \right\rangle \\ K_2 &= \frac{1}{t^2}\,\mathcal{T}\int_0^t dt_1 \int_0^t dt_2 \left\langle \mathscr{H}(t_1)\mathscr{H}(t_2) \right\rangle - K_1^2 \end{aligned} \tag{A.5}$$

The propagator can therefore be expressed in terms of the cumulant averages:

$$\begin{aligned} \left\langle \mathscr{H}(t') \right\rangle_c &= \left\langle \mathscr{H}(t') \right\rangle \\ \left\langle \mathscr{H}(t_1)\mathscr{H}(t_2) \right\rangle_c &= \mathcal{T}\left\langle \mathscr{H}(t_1)\mathscr{H}(t_2) \right\rangle - \left\langle \mathscr{H}(t_1) \right\rangle \left\langle \mathscr{H}(t_2) \right\rangle \end{aligned} \tag{A.6}$$

The propagator can therefore be written as:

$$S = \exp\left(-i \int_0^t dt' \left\langle \mathscr{H}(t') \right\rangle_c - \int_0^t dt_1 \int_0^t dt_2 \left\langle \mathscr{H}(t_1)\mathscr{H}(t_2) \right\rangle_c + \cdots \right) \tag{A.7}$$

Note that if $\mathscr{H}$ is a deterministic function of time, the ensemble averages can be dropped and $\left\langle \mathscr{H}(t) \right\rangle_c = \int_0^t dt'\, \mathscr{H}(t')$ becomes the time-average Hamiltonian, which is the first term in the Magnus expansion. The second term in the cumulant expansion, on the other hand, becomes

$$\begin{aligned} & \mathcal{T}\int_0^t dt_1 \int_0^{t_1} dt_2\, \mathscr{H}(t_1)\mathscr{H}(t_2) - \left(\int_0^t dt'\, \mathscr{H}(t') \right)^2 \\ = \;& 2\int_0^t dt_1 \int_0^{t_1} dt_2\, \mathscr{H}(t_1)\mathscr{H}(t_2) - \int_0^t dt_1 \int_0^t dt_2\, \mathscr{H}(t_1)\mathscr{H}(t_2) \\ = \;& \int_0^t dt_1 \int_0^{t_1} dt_2\, \mathscr{H}(t_1)\mathscr{H}(t_2) - \int_0^t dt_1 \int_{t_1}^t dt_2\, \mathscr{H}(t_1)\mathscr{H}(t_2) \\ = \;& \int_0^t dt_1 \int_0^{t_1} dt_2 \left[\mathscr{H}(t_1),\, \mathscr{H}(t_2) \right], \end{aligned} \tag{A.8}$$

where $[\cdot,\cdot]$ denotes the commutator and we have used the fact that the time-ordering operator $\mathcal{T}$ symmetrizes its argument with respect to permutation of the time points. This is the second term in the Magnus expansion for the "average" (effective) Hamil-

tonian, and proceeding in this fashion one can in principle derive average Hamiltonian theory from the Dyson and cumulant expansions.

Appendix B

Signal loss in state preparation

Since we are interested in the information that we can manipulate and observe, a good measure of the sensitivity gain or loss is the SNR of the qubits storing the information. We consider the magnetization of the Q qubits:

$$SNR = \langle |\vec{M}| \rangle \propto S(\rho) = \sqrt{Tr\{\sum_{i=1}^{Q} \sigma_z^i \rho\}^2 + Tr\{\sum_{i=1}^{Q} \sigma_x^i \rho\}^2 + Tr\{\sum_{i=1}^{Q} \sigma_y^i \rho\}^2} \tag{B.1}$$

.

At room temperature and in a high magnetic field, the NMR spin system is a highly mixed state described by the thermal density matrix ρ_{th}:

$$\rho_{th} \approxeq \frac{\mathbf{1}}{2^N} - \epsilon\rho_{eq} = \frac{\mathbf{1}}{2^N} - \frac{\epsilon}{2^N} \sum_{i=1}^{N} \sigma_z^i \tag{B.2}$$

where the term $\epsilon\rho_{eq}$ is a small, traceless deviation from the identity, which gives rise to the observable signal. The ability to use this system as a quantum information test-bed relies on effectively purifying the mixed equilibrium state. QIP can be performed on *pseudo-pure* states [49, 73, 30], states for which the dynamics of the observable operators are equivalent to the observables of a pure state. Unfortunately, the creation of pseudo-pure states comes at the expense of exponential consumption in experimental resources: time in the case of temporal averaging [73], signal in the case of spatial averaging [30], or usable Hilbert space in the case logical labeling [49].

Since the eigenvalues of a pseudo-pure state are different than those of the mixed state (with the exception of SU(2)), a non-unitary completely positive map, $\mathbf{T}$, must be implemented:

$$\rho_P = \mathbf{T}(\rho_{th}) = \tfrac{\mathbf{1}}{2^N} - \epsilon\alpha(\rho_{pp} - \tfrac{\mathbf{1}}{2^N}) \tag{B.3}$$

where ρ_{pp} is a density matrix describing a pure state. The scaling factor α determines the signal loss and is bounded by the spectral norm ratio (since $\|\rho_{eq}\| \geq \|\mathbf{T}(\rho_{eq})\|$):

$$\alpha \leq \frac{\|\rho_{eq}\|}{\|\rho_{pp} - \mathbf{1}/2^N\|} \tag{B.4}$$

with $\|\rho_{eq}\| = \frac{N}{2^N}$. The SNR loss in the case of a full pseudo-pure state is thus $\frac{N}{2^N-1}$.

In the case of encoded qubits, the information is spread throughout the Hilbert space in a way that is not guaranteed to give an observable signal as defined in Eq. B.1. Since logical qubits represent actual information, the easiest way the access this information is to decoded the logical qubits into physical qubits which will give rise to an observable signal.

We assume to encode l logical qubits among N physical qubits, with a syndrome subsystem $\mathcal{S}$ of dimensions 2^s, then the unitary encoding operation will take the state over l physical qubits and $N-l$ ancilla to the encoded state $|\psi\rangle_L|0\rangle_S$:

$$U_{enc}|\psi\rangle_l|\phi\rangle_s|00...\rangle_{N-l-s} = |\psi\rangle_L|\phi\rangle_S \tag{B.5}$$

where here we assume that the s syndrome states are order as the first ancillas. For a subsystem pseudo-pure state like that of Eq. 4.5, the state post decoding ($U_{enc}^\dagger$) is:

$$\begin{aligned}\rho_{spps} = &\left(a|\psi\rangle\langle\psi| - \tfrac{1-a}{2^N-2^{s+l}}\mathbf{1}_l\right)\tfrac{\mathbf{1}_s}{2^s}|00\ldots\rangle\langle 00\ldots|_{N-l-s} \\ &+\tfrac{1-a}{2^N-2^{s+l}}\mathbf{1},\end{aligned} \tag{B.6}$$

If we reduce the sum of the SNR from Q to l then the information carrying signal is given by: $S(\rho) = a\epsilon\alpha S(|\psi\rangle\langle\psi|_l) \propto a\alpha l$, where $\alpha \leq \frac{\|\rho_{eq}\|}{\|\rho_{pp}-\mathbf{1}/2^N\|}$. To obtain the spectral norm of the subsystem pseudo-pure state traceless part, we calculate its eigenvalues:

$$\{\frac{a}{2^s} - 2^{-N},\ -2^{-N},\ \frac{1-a}{2^N - 2^{s+l}} - 2^{-N}\} \tag{B.7}$$

The upper bound for the signal is obtained for $a = 2^{s+1-N}$ and we have: $SNR \propto N2^{s+1-N}$.

For tensor qubits of logical qubits, as in Eq. 4.7, the decoding has the form:

$$\begin{aligned} U_{enc}^{\dagger}\rho_{spps}U_{enc} &= \bigotimes_{i=1}^{l}[(a|\psi\rangle\langle\psi|_1 - \tfrac{1-a}{2^n-2}\mathbf{1}_1) \\ &\otimes \tfrac{\mathbf{1}_s}{2^s} \otimes |00\ldots\rangle\langle 00\ldots| + \tfrac{1-a}{2^n-2}\mathbf{1}_n]_i \end{aligned} \tag{B.8}$$

where we have made the assumption that $a_i = a$. The signal is again proportional to $a\alpha l$ and varying a we can find the optimal state. The eigenvalues for the traceless part of the subsystem pseudo-pure state are:

$$\begin{aligned} &\prod_{i=1}^{l}(\{\tfrac{a}{2^s}, 0, \tfrac{1-a}{2^n-2^{s+1}}\}_i) - 2^{-N} \\ &= \{(\tfrac{a}{2^s})^{l-p}\left(\tfrac{1-a}{2^n-2^{s+1}}\right)^p \|_{p=0}^{l} - 2^{-N}, -2^{-N}\} \end{aligned} \tag{B.9}$$

The maximum SNR depends on the relative dimension of the logical subspace and the syndrome and on the number of encoded qubits. In particular:

When $l < \frac{-1}{\log_2(1-2^{s-n})}$ the $SNR \propto N2^{s+1/l-n}$ (The norm reaches the minimum value 2^{-N} for $a \leq 2^{s+1/l-n}$).

When $l > \frac{-1}{\log_2(1-2^{s-n})}$, instead, we obtain $SNR \propto \frac{N2^s(2^n-2^s)^l}{2^N-(2^n-2^s)^l}$: The minimum value for the norm $(2^n - 2^s)^{-1} - 2^N$ is obtained for $\frac{a}{2^s} = \frac{1-a}{2^n-2^{s+1}}$, i.e. for $a = \frac{2^s}{2^n-2^s}$).

Notice that for $n \leq s$ there is no useful solution. In both cases, the SNR obtained with a tensor product structure is higher than for the first construction presented.

Appendix C

Publications

- Hodges JS, Yang JC, Ramanathan C, Cory DG. "Universal Control of Nuclear Spins Via Anisotropic Hyperfine Interactions." arXiv:0707.2956 [quant-ph].

- Henry MK, Ramanathan C, Hodges JS, Ryan CA, Ditty MJ, Laflamme R, Cory DG. "Fidelity enhancement by logical qubit encoding." arXiv:0705.4119v1 [quant-ph].

- Cappellaro P, Hodges JS, Havel TF, Cory DG. "Control of qubits encoded in decoherence-free subspaces." *Laser Physics* **17**, 545 (2007).

- Hodges JS, Cappellaro, PC, Havel TF, Martinez R, Cory DG. "Experimental implementation of a logical Bell state encoding ." *Physical Review A* **75**, 042320 (2007).

- Cappellaro P, Hodges JS, Havel TF, Cory DG. "Subsystem pseudopure states." *Physical Review A* **75**, 042321 (2007).

- Hodges JS, Cappellaro P, Havel TF, Cory DG. "Quantum Control of Nuclear Spins." *Decision and Control, 2006 45th IEEE Conference on*, 2488 (2006).

- Cappellaro P, Hodges JS, Havel TF, Cory DG. "Principles of Control for Decoherence Free Subsystems." *Journal of Chemical Physics* **125**, 044514 (2006).

◇ Fortunato EM, Viola L, Hodges J, Teklemariam G, Cory DG "Implementation of universal control on a decoherence-free qubit." *New Journal of Physics* **4**, 5 (2002).

Bibliography

[1] E. Abe, K. M. Itoh, J. Isoya, and S. Yamasaki. Electron-spin phase relaxation of phosphorus donors in nuclear-spin-enriched silicon. *Physical Review B*, 70(3):033204, 2004.

[2] A. Abragam. *Principles of Nuclear Magnetism.* Oxford Univ. Press, 1961.

[3] R. Alicki and M. Fannes. *Quantum Dynamical Systems.* Oxford University Press, 2001.

[4] C. Altafini. Controllability of quantum mechanical systems by root space decomposition of [fraktur su](N). *Journal of Mathematical Physics*, 43(5):2051–2062, 2002.

[5] D. Bacon. *Decoherence, Control, and Symmetry in Quantum Computers.* PhD thesis, University of California: Berkeley, 2001.

[6] D. Bacon, J. Kempe, D. A. Lidar, and K. B. Whaley. Universal Fault-Tolerant Quantum Computation on Decoherence-Free Subspaces. *Phyiscal Review Letters*, 85(8):1758–1761, 2000.

[7] T. M. Barbara, J. F. Martin, and J. G. Wurl. Phase transients in NMR probe circuits. *Journal of Magnetic Resonance*, 93(3):497–508, 1991.

[8] J. Baugh, O. Moussa, C. A. Ryan, A. Nayak, and R. Laflamme. Experimental implementation of heat-bath algorithmic cooling using solid-state nuclear magnetic resonance. *Nature*, 438(7067):470–473, 2005.

[9] A. Beige, D. Braun, B. Tregenna, and P. L. Knight. Quantum Computing Using Dissipation to Remain in a Decoherence-Free Subspace. *Phyiscal Review Letters*, 85(8):1762–1765, 2000.

[10] C. H. Bennett and G. Brassard. Quantum Cryptography: Public Key Distribution and Coin Tossing. In *Proceedings of IEEE International Conference on Computers Systems and Signal Processing*, pages 175–179, 1984.

[11] G. P. Berman, G. W. Brown, M. E. Hawley, and V. I. Tsifrinovich. Solid-State Quantum Computer Based on Scanning Tunneling Microscopy. *Phyiscal Review Letters*, 87(9):097902, 2001.

[12] P. P. Borbat, R. H. Crepeau, and J. H. Freed. Multifrequency Two-Dimensional Fourier Transform ESR: An X/Ku-Band Spectrometer. *Journal of Magnetic Resonance*, 127(2):155–167, 1997.

[13] N. Boulant, J. Emerson, T. F. Havel, D. G. Cory, and S. Furuta. Incoherent Noise in Quantum Information Processing. *Journal of Chemical Physics*, 121:2955–2961, 2004.

[14] M. D. Bowdrey, J. A. Jones, E. Knill, and R. Laflamme. Compiling gate networks on an Ising quantum computer. *Physical Review A*, 72(3):032315, 2005.

[15] S. L. Braunstein, C. M. Caves, R. Jozsa, N. Linden, S. Popescu, and R. Schack. Separability of Very Noisy Mixed States and Implications for NMR Quantum Computing. *Phyiscal Review Letters*, 83(5):1054–1057, 1999.

[16] H. Breuer and F. Petruccione. *The Theory of Open Quantum Systems*. Oxford Univ. Press, 2002.

[17] H.-J. Briegel, W. Dür, J. I. Cirac, and P. Zoller. Quantum Repeaters: The Role of Imperfect Local Operations in Quantum Communication. *Physical Review Letters*, 81(26):5932–5935, 1998.

[18] I. M. Brown and D. J. Sloop. A Pulsed Electron Paramagnetic Resonance Spectrometer. *Review of Scientific Instruments*, 41(12):1774–1777, 1970.

[19] M. S. Byrd and D. A. Lidar. Comprehensive Encoding and Decoupling Solution to Problems of Decoherence and Design in Solid-State Quantum Computing. *Phyiscal Review Letters*, 89(4):047901, 2002.

[20] A. R. Calderbank and P. W. Shor. Good quantum error-correcting codes exist. *Physical Review A*, 54(2):1098–1105, 1996.

[21] P. Cappellaro, J. S. Hodges, T. F. Havel, and D. G. Cory. Principles of control for decoherence-free subsystems. *Journal of Chemical Physics*, 125(4):044514, 2006.

[22] P. Cappellaro, J. S. Hodges, T. F. Havel, and D. G. Cory. Subsystem pseudopure states. *Physical Review A*, 75(4):042321, 2007.

[23] H. Y. Carr and E. M. Purcell. Effects of Diffusion on Free Precession in Nuclear Magnetic Resonance Experiments. *Physical Reivew*, 94(3):630–638, 1954.

[24] T. R. Carver and C. P. Slichter. Polarization of Nuclear Spins in Metals. *Phyiscal Review*, 92(1):212–213, 1953.

[25] Y. C. Cheng and R. J. Silbey. Stochastic Liouville equation approach for the effect of noise in quantum computations. *Physical Review A*, 69(5):052325, 2004.

[26] L. Childress, M. V. G. Dutt, J. M. Taylor, A. S. Zibrov, F. Jelezko, J. Wrachtrup, P. R. Hemmer, and M. D. Lukin. Coherent dynamics of coupled electron and nuclear spin qubits in diamond. *Science*, 314(5797):281–285, 2006.

[27] T. Christides, W. Froncisz, T. Oles, and J. S. Hyde. Probehead with interchangeable loop-gap resonators and rf coils for multifrequency EPR/ENDOR. *Review of Scientific Instruments*, 65(1):63–67, 1994.

[28] I. L. Chuang, N. A. Gershenfeld, M. G. Kubinec, and D. Leung. Bulk Quantum Computation with Nuclear Magnetic Resonance: Theory and Experiment. *Procings of the Royal Society of London A*, 454:447–467, 1998.

[29] D. Cory, R. Laflamme, E. Knill, L. Viola, T. Havel, N. Boulant, G. Boutis, E. Fortunato, S. Lloyd, R. Martinez, C. Negrevergne, M. Pravia, Y. Sharf, G. Teklemariam, Y. Weinstein, and W. Zureck. NMR based quantum information processing: Achievements and prospects. *Fortschritte der Physik*, 48:875, 2000.

[30] D. G. Cory, A. F. Fahmy, and T. F. Havel. Ensemble quantum computing by NMR spectroscopy. *Proceedings of the National Academy of Sciences of the United States of America*, 94:1634, 1997.

[31] B. Cowan. *Nuclear Magnetic Resonance and Relaxation.* Cambridge University Press, 1997.

[32] E. R. Davies. A new pulse endor technique. *Physics Letters A*, 47(1):1–2, 1974.

[33] S. De Filippo. Quantum computation using decoherence-free states of the physical operator algebra. *Physical Review A*, 62(5):052307, 2000.

[34] R. de Sousa and S. Das Sarma. Electron spin coherence in semiconductors: Considerations for a spin-based solid-state quantum computer architecture. *Physical Review B*, 67(3):033301, 2003.

[35] N. Devasahayam, R. Murugesan, K. Matsumoto, J. B. Mitchell, J. A. Cook, S. Subramanian, and M. C. Krishna. Tailored sinc pulses for uniform excitation and artifact-free radio frequency time-domain EPR imaging. *Journal of Magnetic Resonance*, 168(1):110–117, 2004.

[36] D. P. DiVincenzo. Two-bit gates are universal for quantum computation. *Physical Review A*, 51(2):1015–1022, 1995.

[37] D. P. DiVincenzo, D. Bacon, J. Kempe, G. Burkard, and K. B. Whaley. Universal quantum computation with the exchange interaction. *Nature*, 408(6810):339–342, 2000.

[38] L.-M. Duan and G.-C. Guo. Preserving Coherence in Quantum Computation by Pairing Quantum Bits. *Phyiscal Review Letters*, 79(10):1953–1956, 1997.

[39] M. V. G. Dutt, L. Childress, L. Jiang, E. Togan, J. Maze, F. Jelezko, A. S. Zibrov, P. R. Hemmer, and M. D. Lukin. Quantum Register Based on Individual Electronic and Nuclear Spin Qubits in Diamond. *Science*, 316(5829):1312–1316, 2007.

[40] A. Einstein, B. Podolsky, and N. Rosen. Can Quantum-Mechanical Description of Physical Reality Be Considered Complete? *Phyiscal Review*, 47(10):777–780, 1935.

[41] J. Forrer, S. Pfenninger, J. Eisenegger, and A. Schweiger. A pulsed ENDOR probehead with the bridged loop-gap resonator: Construction and performance. *Review of Scientific Instruments*, 61(11):3360–3367, 1990.

[42] J. Forrer, S. Pfenninger, B. Wagner, and T. Weiland. Progress in instrumentation for pulsed ESR and ENDOR spectroscopy. *Pure and Appl. Chem.*, 64(6):865–872, 1992.

[43] E. M. Fortunato, M. A. Pravia, N. Boulant, G. Teklemariam, T. F. Havel, and D. G. Cory. Design of strongly modulating pulses to implement precise effective Hamiltonians for quantum information processing. *The Journal of Chemical Physics*, 116(17):7599–7606, 2002.

[44] E. M. Fortunato, L. Viola, J. Hodges, G. Teklemariam, and D. G. Cory. Implementation of universal control on a decoherence-free qubit. *New Journal of Physics*, 4:5, 2002.

[45] E. M. Fortunato, L. Viola, M. A. Pravia, E. Knill, R. Laflamme, T. F. Havel, and D. G. Cory. Exploring noiseless subsystems via nuclear magnetic resonance. *Physical Review A*, 67(6):062303, 2003.

[46] W. Froncisz and J. S. Hyde. The loop-gap resonator: a new microwave lumped circuit ESR sample structure. *Journal of Magnetic Resonance*, 47(3):515–521, 1982.

[47] R. Gallay and J. J. van der Klink. Resonator and coupling structure for spin-echo ESR. *Journal of Physics E*, 19(3):226–230, 1986.

[48] D. Gamliel and H. Levanon. *Stochastic Processes in Magnetic Resonance*. World Scientific, 1995.

[49] N. A. Gershenfeld and I. L. Chuang. Bulk Spin-Resonance Quantum Computation. *Science*, 275(5298):350–356, 1997.

[50] V. Giovannetti, S. Lloyd, and L. Maccone. Quantum-Enhanced Measurements: Beating the Standard Quantum Limit. *Science*, 306(5700):1330–1336, 2004.

[51] D. Giulini, E. Joos, C. Kiefer, J. Kupsch, I. Stamatescu, and H. D. Zeh. *Decoherence and the Appearance of a Classical World in Quantum Theory*. Springer-Verlag, Berlin, FRG, 1996.

[52] D. Gottesman. Class of quantum error-correcting codes saturating the quantum Hamming bound. *Physical Review A*, 54(3):1862–1868, 1996.

[53] L. K. Grover. A fast quantum mechanical algorithm for database search. In *STOC '96: Proceedings of the twenty-eighth annual ACM symposium on Theory of computing*, pages 212–219, New York, NY, USA, 1996. ACM Press.

[54] U. Haeberlen. *High Resolution NMR in Solids: Selective Averaging.* Academic Press, 1976.

[55] U. Haeberlen and J. S. Waugh. Coherent Averaging Effects in Magnetic Resonance. *Phyiscal Review*, 175(2):453–467, 1968.

[56] U. Haeberlen and J. S. Waugh. Coherent Averaging Effects in Magnetic Resonance. *Phyiscal Review*, 175(2):453–467, 1968.

[57] E. L. Hahn. Spin Echoes. *Phyiscal Review*, 80(4):580–594, 1950.

[58] T. F. Havel, Y. Sharf, L. Viola, and D. G. Cory. Hadamard products of product operators and the design of gradient-diffusion experiments for simulating decoherence by NMR spectroscopy. *Physics Letters A*, 280(5-6):282–288, 2001.

[59] W. H. Hayt Jr and J. E. Kemmerly. *Engineering Circuit Analysis.* McGraw Hill, third edition, 1978.

[60] M. Henry, C. Ramanathan, J. S. Hodges, C. A. Ryan, M. J. Ditty, R. Laflamme, and D. G. Cory. Fidelity enhancement by logical qubit encoding. *arXiv:0705.4119*, 2007.

[61] H. Hirata and M. Ono. Resonance frequency estimation of a bridged loop-gap resonator used for magnetic resonance measurements. *Review of Scientific Instruments*, 67(1):73–78, 1996.

[62] E. C. Hoffmann, M. Hubrich, and A. Schweiger. Primary Nuclear Spin Echoes in EPR Induced by Microwave Pulses. *Journal of Magnetic Resonance, Series A*, 117(1):16–27, 1995.

[63] M. Huisjen and J. S. Hyde. A pulsed EPR spectrometer. *Review of Scientific Instruments*, 45(5):669–675, 1974.

[64] M. Jaworski, A. Sienkiewicz, and C. P. Scholes. Double-Stacked Dielectric Resonator for Sensitive EPR Measurements. *Journal of Magnetic Resonance*, 124(1):87–96, 1997.

[65] F. Jelezko, T. Gaebel, I. Popa, M. Domhan, A. Gruber, and J. Wrachtrup. Observation of Coherent Oscillation of a Single Nuclear Spin and Realization of a Two-Qubit Conditional Quantum Gate. *Phyiscal Review Letters*, 93(13):130501, 2004.

[66] F. Jelezko and J. Wrachtrup. Single defect centres in diamond: A review. *Physica Status Solidi A*, 203(13):3207–3225, 2006.

[67] J. A. Jones and E. Knill. Efficient Refocusing of One-Spin and Two-Spin Interactions for NMR Quantum Computation. *Journal of Magnetic Resonance*, 141(2):322–325, 1999.

[68] B. E. Kane. A silicon-based nuclear spin quantum computer. *Nature*, 393(6681):133–137, 1998.

[69] J. Kang, S. Tokdemir, J. Shao, and W. H. Nelson. Electronic g-factor measurement from ENDOR-induced EPR patterns: malonic acid and guanine hydrochloride dihydrate. *Journal of Magnetic Resonance*, 165(1):128–136, 2003.

[70] J. Kempe, D. Bacon, D. A. Lidar, and K. B. Whaley. Theory of decoherence-free fault-tolerant universal quantum computation. *Physical Review A*, 63(4):042307, 2001.

[71] N. Khaneja, T. Reiss, C. Kehlet, T. Schulte-Herbrüggen, and S. J. Glaser. Optimal control of coupled spin dynamics: design of NMR pulse sequences by gradient ascent algorithms. *Journal of Magnetic Resonance*, 172:296–305, 2005.

[72] J. M. Kikkawa and D. D. Awschalom. All-Optical Magnetic Resonance in Semiconductors. *Science*, 287(5452):473–476, 2000.

[73] E. Knill, I. Chuang, and R. Laflamme. Effective pure states for bulk quantum computation. *Physical Review A*, 57(5):3348–3363, 1998.

[74] E. Knill, R. Laflamme, R. Martinez, and C.-H. Tseng. An algorithmic benchmark for quantum information processing. *Nature*, 404:368–370, 2000.

[75] E. Knill, R. Laflamme, and L. Viola. Theory of Quantum Error Correction for General Noise. *Phyiscal Review Letters*, 84(11):2525–2528, 2000.

[76] E. Knill, R. Laflamme, and W. H. Zurek. Resilient Quantum Computation. *Science*, 279(5349):342–345, 1998.

[77] J. Kohler, J. A. J. M. Disselhorst, M. C. J. M. Donckers, E. J. J. Groenen, J. Schmidt, and W. E. Moerner. Magnetic resonance of a single molecular spin. *Nature*, 363(6426):242–244, 1993.

[78] K. Kraus. General state changes in quantum theory. *Annals of Physics*, 64:311–335, 1971.

[79] D. W. Kribs and R. W. Spekkens. Quantum error-correcting subsystems are unitarily recoverable subsystems. *Physical Review A*, 74(4):042329, 2006.

[80] R. Kubo. Fluctuation, Relaxation and Resonance in Magnetic Systems. In D. ter Haar, editor, *Fluctuation, Relaxation and Resonance in Magnetic Systems*, page 23. Oliver and Boyd, Edinburgh, 1962.

[81] E. K. L Viola and R. Laflamme. Constructing qubits in physical systems. *Journal of Physics A*, 34(35):7067–7079, 2001.

[82] T. D. Ladd, J. R. Goldman, F. Yamaguchi, Y. Yamamoto, E. Abe, and K. M. Itoh. All-Silicon Quantum Computer. *Physical Review Letters*, 89(1):017901, 2002.

[83] K. K. Y. Lee. Investigations on resource-limited quantum control through NMR pulses. Master's thesis, Massachusetts Institute of Technology, 2006.

[84] S. Lee, B. R. Patyal, and J. H. Freed. A two-dimensional Fourier transform electron-spin resonance (ESR) study of nuclear modulation and spin relaxation in irradiated malonic acid. *Journal of Chemical Physics*, 98(5):3665–3689, 1993.

[85] M. H. Levitt. Composite pulses. *Progress in Nuclear Magnetic Resonance Spectroscopy*, 18(2):61–122, 1986.

[86] D. A. Lidar, D. Bacon, J. Kempe, and K. B. Whaley. Decoherence-free subspaces for multiple-qubit errors. I. Characterization. *Physical Review A*, 63(2):022306, 2001.

[87] D. A. Lidar, D. Bacon, J. Kempe, and K. B. Whaley. Decoherence-free subspaces for multiple-qubit errors. II. Universal, fault-tolerant quantum computation. *Physical Review A*, 63(2):022307, 2001.

[88] D. A. Lidar, I. L. Chuang, and K. B. Whaley. Decoherence-Free Subspaces for Quantum Computation. *Phyiscal Review Letters*, 81(12):2594–2597, 1998.

[89] D. A. Lidar and L.-A. Wu. Reducing Constraints on Quantum Computer Design by Encoded Selective Recoupling. *Phyiscal Review Letters*, 88(1):017905, 2001.

[90] D. Loss and D. P. DiVincenzo. Quantum computation with quantum dots. *Physical Review A*, 57(1):120–126, 1998.

[91] R. C. McCalley and A. L. Kwiram. ENDOR Studies at 4.2 K of the radicals in Malonic-acid single-crystals. *Journal of Chemical Physics*, 97(12):2888–2903, 1993.

[92] H. M. McConnell, C. Heller, T. Cole, and R. W. Fessenden. Radiation Damage in Organic Crystals. I. CH(COOH)2 in Malonic Acid. *Journal of the American Chemical Society*, 82(4):766–775, 1960.

[93] M. Mehdizadeh and T. K. Ishii. Electromagnetic field analysis and calculation of the resonance characteristics of the loop-gap resonator. *Microwave Theory and Techniques, IEEE Transactions on*, 37(7):1113–1118, 1989.

[94] M. Mehdizadeh, T. K. Ishii, J. S. Hyde, and F. Wojciech. Loop-Gap Resonator: A Lumped Mode Microwave Resonant Structure. *Microwave Theory and Techniques, IEEE Transactions on*, 83(12):1059–1064, 1983.

[95] M. Mehring and J. Mende. Spin-bus concept of spin quantum computing. *Physical Review A*, 73(5):052303, 2006.

[96] M. Mehring, J. Mende, and W. Scherer. Entanglement between an Electron and a Nuclear Spin (1/2). *Phyiscal Review Letters*, 90(15):153001, 2003.

[97] M. Mehring, W. Scherer, and A. Weidinger. Pseudoentanglement of Spin States in the Multilevel N@C[sub 60] System. *Phyiscal Review Letters*, 93(20):206603, 2004.

[98] M. Mehring and J. S. Waugh. Phase Transients in Pulsed NMR Spectrometers. *Review of Scientific Instruments*, 43(4):649–653, 1972.

[99] S. Meiboom and D. Gill. Modified Spin-Echo Method for Measuring Nuclear Relaxation Times. *Review of Scientific Instruments*, 29:688–691, 1958.

[100] W. B. Mims. Electron Echo Methods in Spin Resonance Spectrometry. *Review of Scientific Instruments*, 36(10):1472–1479, 1965.

[101] W. B. Mims. Pulsed Endor Experiments. *Proceedings of the Royal Society of London. Series A, Mathematical and Physical Sciences (1934-1990)*, 283(1395):452–457, 1965.

[102] M. Mohseni, J. S. Lundeen, K. J. Resch, and A. M. Steinberg. Experimental Application of Decoherence-Free Subspaces in an Optical Quantum-Computing Algorithm. *Physical Review Letters*, 91(18):187903, 2003.

[103] J. J. L. Morton, A. M. Tyryshkin, A. Ardavan, S. C. Benjamin, K. Porfyrakis, S. A. Lyon, and G. A. D. Briggs. Bang-bang control of fullerene qubits using ultrafast phase gates. *Nature Physics*, 2(1):40–43, 2006.

[104] M. A. Nielsen. A simple formula for the average gate fidelity of a quantum dynamical operation. *Physics Letters A*, 303(4):249–252, 2002.

[105] I. Novikova, A. V. Gorshkov, D. F. Phillips, A. S. S. rensen, M. D. Lukin, and R. L. Walsworth. Optimal Control of Light Pulse Storage and Retrieval. *Physical Review Letters*, 98(24):243602, 2007.

[106] J. E. Ollerenshaw, D. A. Lidar, and L. E. Kay. Magnetic Resonance Realization of Decoherence-Free Quantum Computation. *Physical Review Letters*, 91(21):217904, 2003.

[107] K. Ono and S. Tarucha. Nuclear-Spin-Induced Oscillatory Current in Spin-Blockaded Quantum Dots. *Physical Review Letters*, 92(25):256803, 2004.

[108] A. W. Overhauser. Polarization of Nuclei in Metals. *Phyiscal Review*, 92(2):411–415, 1953.

[109] A. Peres. *Quantum Theory: Concepts and Methods.* Kluwer Academic Publishers, 1995.

[110] J. R. Petta, A. C. Johnson, J. M. Taylor, E. A. Laird, A. Yacoby, M. D. Lukin, C. M. Marcus, M. P. Hanson, and A. C. Gossard. Coherent Manipulation of Coupled Electron Spins in Semiconductor Quantum Dots. *Science*, 309(5744):2180–2184, 2005.

[111] S. Pfenninger, J. Forrer, A. Schweiger, and T. Weiland. Bridged loop–gap resonator: A resonant structure for pulsed ESR transparent to high-frequency radiation. *Review of Scientific Instruments*, 59(5):752–760, 1988.

[112] A. Ponti and A. Schweiger. Nuclear coherence-transfer echoes in pulsed EPR. *Journal of Chemical Physics*, 102(13):5207–5219, 1995.

[113] C. P. Poole. *Electron Spin Resonance.* Dover Publications, Inc., 1996.

[114] M. Pravia, E. Fortunato, Y. Weinstein, M. D. Price, G. Teklemariam, R. J. Nelson, Y. Sharf, S. Somaroo, C. H. Tseng, T. F. Havel, and D. G. Cory. Observations of quantum dynamics by solution-state NMR spectroscopy. *Concepts in Magnetic Resonance*, 11(4):225–238, 1999.

[115] M. A. Pravia, N. Boulant, J. Emerson, A. Farid, E. M. Fortunato, T. F. Havel, R. Martinez, and D. G. Cory. Robust control of quantum information. *The Journal of Chemical Physics*, 119(19):9993–10001, 2003.

[116] W. H. Press, W. T. Vetterling, S. A. Teukolsky, and B. P. Flannery. *Numerical Recipes in C: The Art of Scientific Computing.* Cambridge University Press, second edition edition, 1992.

[117] M. D. Price, S. S. Somaroo, A. E. Dunlop, T. F. Havel, and D. G. Cory. Generalized methods for the development of quantum logic gates for an NMR quantum information processor. *Physical Review A*, 60(4):2777–2780, 1999.

[118] V. Ramakrishna, M. V. Salapaka, M. Dahleh, H. Rabitz, and A. Peirce. Controllability of molecular systems. *Physical Review A*, 51(2):960–966, 1995.

[119] N. F. Ramsey. A Molecular Beam Resonance Method with Separated Oscillating Fields. *Physical Reivew*, 78(6):695–699, 1950.

[120] R. Raussendorf and H. J. Briegel. A One-Way Quantum Computer. *Physical Review Letters*, 86(22):5188–5191, 2001.

[121] W.-K. Rhim, D. D. Elleman, L. B. Schreiber, and R. W. Vaughan. Analysis of multiple pulse NMR in solids. II. *The Journal of Chemical Physics*, 60(11):4595–4604, 1974.

[122] L. G. Rowan, E. L. Hahn, and W. B. Mims. Electron-Spin-Echo Envelope Modulation. *Phyiscal Review*, 137(1A):A61–A71, 1965.

[123] D. Rugar, R. Budakian, H. J. Mamin, and B. W. Chui. Single spin detection by magnetic resonance force microscopy. *Nature*, 430(6997):329–332, 2004.

[124] S. K. Saikin, W. Yao, and L. J. Sham. Single-electron spin decoherence by nuclear spin bath: Linked-cluster expansion approach. *Physical Review B*, 75(12):125314, 2007.

[125] K. M. Salikhov, D. J. Schneider, S. Saxena, and J. H. Freed. A theoretical approach to the analysis of arbitrary pulses in magnetic resonance. *Chemical Physics Letters*, 262(1-2):17–26, 1996.

[126] R. Schack and C. M. Caves. Classical model for bulk-ensemble NMR quantum computation. *Physical Review A*, 60(6):4354–4362, 1999.

[127] S. G. Schirmer, H. Fu, and A. I. Solomon. Complete controllability of quantum systems. *Physical Review A*, 63(6):063410, 2001.

[128] B. Schumacher. Sending entanglement through noisy quantum channels. *Physical Review A*, 54(4):2614–2628, 1996.

[129] A. Schweiger, C. Gemperle, and R. R. Ernst. Soft pulse electron-spin-echo-envelope modulation spectroscopy (soft ESEEM). *Journal of Magnetic Resonance*, 86(1):70–81, 1990.

[130] A. Schweiger and G. Jeschke. *Principles of pulse electron paramagnetic resonance.* Oxford University Press, New York, New York, 2001.

[131] J. J. Shane, I. Gromov, S. Vega, and D. Goldfarb. A versatile pulsed X-band ENDOR spectrometer. *Review of Scientific Instruments*, 69(9):3357–3364, 1998.

[132] P. W. Shor. Algorithms for quantum computation: discrete logarithms and factoring. In *Proceedings 35th Annual Symposium on Foundations of Computer Science*, pages 124–134, 1994.

[133] P. W. Shor. Scheme for reducing decoherence in quantum computer memory. *Physical Review A*, 52(4):R2493–R2496, 1995.

[134] C. P. Slichter. *Principles of Magnetic Resonance.* Springer-Verlag, 1990.

[135] I. Solomon. Relaxation Processes in a System of Two Spins. *Physical Review*, 99(2):559–565, 1955.

[136] A. Steane. Multiple-Particle Interference and Quantum Error Correction. *Proceedings of the Royal Society A*, 452(1954):2551–2577, 1996.

[137] D. Suter and K. Lim. Scalable architecture for spin-based quantum computers with a single type of gate. *Physical Review A*, 65(5):052309, 2002.

[138] J. Taylor and M. Lukin. Dephasing of Quantum Bits by a Quasi-Static Mesoscopic Environment. *Quantum Information Processing*, 5(6):503–536, 2006.

[139] G. Teklemariam, E. M. Fortunato, C. C. López, J. Emerson, J. P. Paz, T. F. Havel, and D. G. Cory. Method for modeling decoherence on a quantum-information processor. *Physical Review A*, 67(6):062316, 2003.

[140] C. H. Tseng, S. Somaroo, Y. Sharf, E. Knill, R. Laflamme, T. F. Havel, and D. G. Cory. Quantum simulation of a three-body-interaction Hamiltonian on an NMR quantum computer. *Physical Review A*, 61(1):012302, 1999.

[141] G. Turinici and H. Rabitz. Quantum wavefunction controllability. *Chemical Physics*, 267(1-3):1–9, 2001.

[142] C. Uchiyama and M. Aihara. Synchronized pulse control of decoherence. *Physical Review A*, 68(5):052302, 2003.

[143] A. J. Vega. Controlling the effects of pulse transients and RF inhomogeneity in phase-modulated multiple-pulse sequences for homonuclear decoupling in solid-state proton NMR. *Journal of Magnetic Resonance*, 170(1):22–41, 2004.

[144] L. Viola. Quantum control via encoded dynamical decoupling. *Physical Review A*, 66(1):012307, 2002.

[145] L. Viola, E. M. Fortunato, M. A. Pravia, E. Knill, R. Laflamme, and D. G. Cory. Experimental Realization of Noiseless Subsystems for Quantum Information Processing. *Science*, 293(5537):2059–2063, 2001.

[146] L. Viola and E. Knill. Verification procedures for quantum noiseless subsystems. *Physical Review A*, 68(3):032311, 2003.

[147] L. Viola, S. Lloyd, and E. Knill. Universal Control of Decoupled Quantum Systems. *Physical Review Letters*, 83(23):4888–4891, 1999.

[148] W. S. Warren;, N. Gershenfeld, and I. Chuang;. The Usefulness of NMR Quantum Computing. *Science*, 277(5332):1688–1690, 1997.

[149] Y. S. Weinstein, T. F. Havel, J. Emerson, N. Boulant, M. Saraceno, S. Lloyd, and D. G. Cory. Quantum process tomography of the quantum Fourier transform. *Journal of Chemical Physics*, 121(13):6117–6133, 2004.

[150] W. M. Witzel, X. Hu, and S. D. Sarma. Decoherence induced by anisotropic hyperfine interaction in Si spin qubits. *Physical Review B*, 76(3):035212, 2007.

[151] P. Zanardi and M. Rasetti. Noiseless Quantum Codes. *Physical Review Letters*, 79(17):3306–3309, 1997.

[152] W. H. Zurek. Decoherence and the Transition from Quantum to Classical. *Physics Today*, pages 36–44, 1991.